

**EFFECT OF HEAT TREATMENT ON NANOCRYSTALLINE
FORMATION IN $\text{Fe}_{40}\text{Ni}_{40}(\text{Si}+\text{B})_{19}\text{Mo}_{1-2}$ AMORPHOUS RIBBONS**



**A THESIS SUBMITTED IN PARTIAL FULFILLMENT
OF THE REQUIREMENTS FOR
THE DEGREE OF MASTER OF SCIENCE
(PHYSICAL CHEMISTRY)
FACULTY OF GRADUATE STUDIES
MAHIDOL UNIVERSITY
2003**

**ISBN 974-04-3077-5
COPYRIGHT OF MAHIDOL UNIVERSITY**

Thesis
Entitled

**EFFECT OF HEAT TREATMENT ON NANOCRYSTALLINE
FORMATION IN $\text{Fe}_{40}\text{Ni}_{40}(\text{Si}+\text{B})_{19}\text{Mo}_{1-2}$ AMORPHOUS RIBBONS**

Somjet Saiseng

Mr.Somjet Saiseng
Candidate

Pongtip Winotai

Assoc.Prof. Pongtip Winotai,
Ph.D.(Physics)
Major-Advisor

I-Ming Tang

Prof. I-Ming Tang,
Ph.D.(Physics)
Co-Advisor

Sauvarop Limcharoen

Prof. Sauvarop Limcharoen,
Dr.rer.nat (Chemistry)
Co-Advisor

Rassmidara Hoonsawat

Assoc.Prof. Rassmidara Hoonsawat,
Ph.D.
Dean
Faculty of Graduate Studies

Sauvarop Limcharoen

Prof. Sauvarop Limcharoen,
Dr.rer.nat (Chemistry)
Chair
Master of Science Programme
in Physical Chemistry
Faculty of Science

Thesis
Entitled

**EFFECT OF HEAT TREATMENT ON NANOCRYSTALLINE
FORMATION IN $\text{Fe}_{40}\text{Ni}_{40}(\text{Si}+\text{B})_{19}\text{Mo}_{1-2}$ AMORPHOUS RIBBONS**

was submitted to the Faculty of Graduate Studies, Mahidol University
For the degree of Master of Science
Major in Physical Chemistry

on
4 April, 2003



.....

Mr.Somjet Saiseng
Candidate



.....

Assoc.Prof.Pongtip Winotai,
Ph.D.(Physics)
Chair



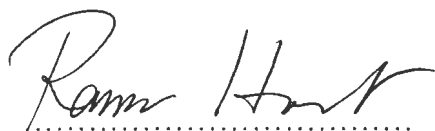
.....

Prof. I-Ming Tang,
Ph.D.(Physics)
Member



.....

Assis.Prof.Tanakorn Osotchan,
Ph.D. (Physics)
Member



.....

Assoc.Prof.Rassmidara Hoonsawat,
Ph.D.
Dean
Faculty of Graduate Studies
Mahidol University



.....

Prof.Amaret Bhumiratana,
Ph.D.
Dean
Faculty of Science
Mahidol University

ACKNOWLEDGMENT

I wish to express my sincere gratitude and appreciation to my advisor Assoc. Prof. Dr. Pongtip Winotai for his introduction and kindness through out this study. I would like to thank Prof. Dr. I-Ming Tang who support ribbons to study. My sincere thanks are expressed to Prof. Dr. Sauvarop Bualek-Limchareon and Assis. Prof. Dr. Tanakorn Osochan for their helpful suggestion and for their useful suggestion and completion this thesis.

I wish to thank Assoc.Prof.Pichet Limsuwan, Department of Physics, Faculty of science. King Mongkut's University of Technology Thonburi, for AFM measurements.

I would like to thank Miss Silipan Nilpairuch, Metallurgy and Material Research Institute, Chulalongkorn University, for VSM measurement.

I am grateful to Postgraduate Education and Research Program in Chemistry, PERCH and Teaching Assistant scholarship for financial.

My appreciation is also extended to all the lectures of the physical chemistry and chemical physics, Mahidol University for valuable knowledge.

Finally, I wish to thank my family, my friends and everybody for their encouragement and support which help me to complete this thesis.

Somjet Saiseng

EFFECT OF HEAT TREATMENT ON NANOCRYSTALLINE FORMATION IN $\text{Fe}_{40}\text{Ni}_{40}(\text{Si}+\text{B})_{19}\text{Mo}_{1-2}$ AMORPHOUS RIBBONS

SOMJET SAISENG 4236042 SCPC/M

M.Sc.(PHYSICAL CHEMISTRY)

THESIS ADVISORS: PONGTIP WINOTAI, Ph.D.(PHYSICS), I-MING TANG, Ph.D.(PHYSICS), SAOVAROP LIMCHAREON, Dr.rer.nat(CHEMISTRY)

ABSTRACT

The effect of heat treatment at various temperatures of $\text{Fe}_{40}\text{Ni}_{40}(\text{Si}+\text{B})_{19}\text{Mo}_{1-2}$ amorphous ribbon was investigated by Mössbauer spectroscopy, X-ray diffraction, scanning electron microscope, differential thermal analysis, vibrating sample magnetometer and ferromagnetic resonance to observe the evolution of the crystalline formations and magnetic properties.

In the first stage of crystallization, all samples still remained in the amorphous phase. In the second stage, the amorphous phase was partially converted to the crystalline phase, while in the third stage, the ribbon completely crystallized. The crystal structures were determined by XRD, the crystallization temperature by DTA and the morphology by SEM. In the first stage, the amorphous ribbon $\text{Fe}_{40}\text{Ni}_{40}(\text{Si}+\text{B})_{19}\text{Mo}_{1-2}$ was annealed at 350 °C and 400 °C for 2 hours in a furnace with heating rate 5 °C/min under argon atmosphere. The XRD patterns showed one broad peak and their hyperfine fields measured by Mössbauer spectrometer indicated, except for some reorientation of local magnetizations, that the samples were still in the amorphous phase. The direction of the local magnetization was out of the ribbon plane when the annealing temperature was raised. In the second stage, both Mössbauer spectra and XRD of annealed samples at 450 °C and 475 °C could be interpreted as consisting of amorphous and crystalline phases. The crystal phases were composed of α -Fe, α -Fe(Si) and t - Fe_2B , while at 500 °C, a new crystalline phase (fcc -FeNi) was observed. In the third stage, Mössbauer results showed t - Fe_5SiB_2 and t - Fe_3B crystal structures at 525 °C, while α -Fe and α -Fe(Si) disappeared at 550 °C. At 600 °C, the t - Fe_5SiB_2 phase vanished, while XRD peak intensities of Ni-base compound increased.

SEM and AFM results could confirm that annealing the ribbon below 500° C for two hours would give rise to nanocrystalline structures. The average nanograin size increased with the annealing temperature. The magnetic properties measured by VSM showed that the magnetization increased with the temperature. The magnetization also exhibited hysteresis behaviour, which indicated the presence of some magnetic domains after heat treatments. FMR results showed that the magnetization of amorphous ribbon was in the plane and was more or less perpendicular to the ribbon plane after annealing at 600 °C. The peak-to-peak line width of FMR also indicated the magnetic interactions are of short-range order for the amorphous phase and longer-range order for the crystallized phases.

KEY WORDS: MÖSSBAUER SPECTROSCOPY/AMORPHOUS MATERIAL/

X-RAYS DIFFRACTION

ผลของการให้ความร้อนที่มีต่อการเกิดผลึกขนาดนาโนเมตรในแผ่นอะมอร์ฟัส $\text{Fe}_{40}\text{Ni}_{40}(\text{Si}+\text{B})_{19}\text{Mo}_{1-2}$ (EFFECT OF HEAT TREATMENT ON NANOCRYSTALLINE FORMATION IN $\text{Fe}_{40}\text{Ni}_{40}(\text{Si}+\text{B})_{19}\text{Mo}_{1-2}$ AMORPHOUS RIBBONS)

สมเจตน์ ชัยเส็ง 4236042 SCPC/M

วท.ม. (เคมีเชิงฟิสิกส์)

คณะกรรมการควบคุมวิทยานิพนธ์: พงศ์ทิพย์ วิโนทัย, Ph.D(PHYSICS), I-MING TANG, Ph.D.(PHYSICS), เสาวภย์ ลิ้มเจริญ, Dr. rer. nat(CHEMISTRY),

บทคัดย่อ

ในช่วงแรกของการเปลี่ยนแปลงแผ่นอะมอร์ฟัสยังคงมีโครงสร้างแบบอะมอร์ฟัสทั้งหมด ส่วนช่วงที่สองจะมีการเปลี่ยนแปลงเกิดโครงสร้างผลึกขึ้นบางส่วน ในขณะที่ช่วงที่สามจะมีการเปลี่ยนแปลงเป็นโครงสร้างผลึกโดยสมบูรณ์ โครงสร้างผลึกที่เกิดขึ้นสามารถยืนยันโดย XRD อุณหภูมิของการเกิดโครงสร้างผลึกยืนยันโดย DTA สังเกตลักษณะของผลึกโดย AFM และ SEM และศึกษาคุณสมบัติทางแม่เหล็กโดย FMR และ VSM ในช่วงแรกของการศึกษาจะให้ความร้อนที่อุณหภูมิ 350 °C และ 400 °C ในเตาเผา เป็นเวลา 2 ชั่วโมง ในอัตราการให้ความร้อน 5 °C ต่อนาที ภายใต้บรรยากาศอาร์กอน ผลจากเอ็กซ์เรย์ดิฟแฟรคชันพบว่าแผ่นอะมอร์ฟัสยังคงมีโครงสร้างเป็นอะมอร์ฟัสทั้งหมด ผลจากมอสบาวเออร์สเปกโทรมิเตอร์แสดงให้เห็นว่าทิศทางของ magnetization ไม่อยู่ในระนาบของแผ่นอะมอร์ฟัส ในช่วงที่สองทำการให้ความร้อนแก่แผ่นอะมอร์ฟัสที่ 450 °C และ 475 °C ภายใต้เงื่อนไขเดียวกัน พบว่าแผ่นอะมอร์ฟัสบางส่วนเกิดโครงสร้างผลึกของ $\alpha\text{-Fe}$ $\alpha\text{-Fe}(\text{Si})$ และ $t\text{-Fe}_2\text{B}$ ในขณะที่เมื่อให้ความร้อนที่ 500 °C มีโครงสร้างใหม่ของ $fcc\text{-FeNi}$ เกิดขึ้น ส่วนการเปลี่ยนแปลงในช่วงที่สามพบว่าโครงสร้างของแผ่นอะมอร์ฟัสกลายเป็นโครงสร้างผลึกอย่างสมบูรณ์ ที่อุณหภูมิ 525 °C พบโครงสร้างผลึกของ $t\text{-Fe}_5\text{SiB}_2$ และ $t\text{-Fe}_3\text{B}$ ในขณะที่เมื่อให้ความร้อนที่ 550 °C โครงสร้างผลึกของ $\alpha\text{-Fe}$ $\alpha\text{-Fe}(\text{Si})$ หายไป ไม่พบโครงสร้างใหม่เมื่อให้ความร้อนที่ 575 °C เมื่อให้ความร้อนที่ 600 °C โครงสร้างผลึกของ $t\text{-Fe}_5\text{SiB}_2$ หายไป ซึ่งการเปลี่ยนแปลงในช่วงที่สามนี้ ผลจาก XRD แสดงให้เห็นถึงสารประกอบของ Ni และปริมาณของสารประกอบ Ni จะเพิ่มขึ้นตามอุณหภูมิที่ให้แก่แผ่นอะมอร์ฟัส

ผลจากภาพ SEM และ AFM ที่อุณหภูมิต่ำกว่า 500 °C เกิดผลึกขนาดนาโนเมตรโดยที่ขนาดจะเพิ่มขึ้นตามอุณหภูมิที่สูงขึ้น ส่วนคุณสมบัติทางแม่เหล็กที่ศึกษาโดย VSM พบว่า ค่า magnetization มีค่าสูงขึ้นเมื่อให้ความร้อนแก่แผ่นอะมอร์ฟัสสูงขึ้น จาก FMR แสดงให้เห็นว่าทิศทางของ อยู่ในทิศเกือบตั้งฉากกับระนาบของแผ่นอะมอร์ฟัสหลังจากให้ความร้อน

112 หน้า. ISBN 974-04-3077-5

CONTENTS

	Page
ACKNOWLEDGEMENT	iii
ABSTRACT (English)	iv
ABSTRACT (Thai)	v
LIST OF TABLES	viii
LIST OF FIGURES	ix
LIST OF ABBREVIATIONS	xiv
CHAPTER	
I INTRODUCTION	1
1.1 Amorphous Materials	2
1.1.1 Preparation of Amorphous Materials	3
1.1.2 Application of Amorphous Materials	4
1.2 Nanocrystalline Materials	8
1.2.1 Nanocrystallization	11
1.2.2 Nanocrystallization Products	12
II OBJECTIVE	14
III LITERATURE	15
IV EXPERIMENTAL METHODS	17
4.1 Instruments	17
4.2 Materials	18
4.2.1 Annealing of the $\text{Fe}_{40}\text{Ni}_{40}(\text{Si}+\text{B})_{19}\text{Mo}_{1-2}$	18
4.3 Mössbauer Spectroscopy	18
4.3.1 Calibration of the Mössbauer Analyzer	19
4.3.2 Fitting Procedures for the Mössbauer Spectra in $\text{Fe}_{40}\text{Ni}_{40}(\text{Si}+\text{B})_{19}\text{Mo}_{1-2}$ Amorphous Ribbons	21

CONTENTS (Continued)

		Page
	4.4 Scanning Electron Microscope (SEM)	21
	4.5 Atomic Force Microscopy (AFM)	22
	4.6 X-ray Diffraction (XRD)	22
	4.7 Differential Thermal Analysis (DTA)	22
	4.8 Ferromagnetic Resonance (FMR)	23
	4.9 Vibrating sample analysis(VSM)	23
	4.10 Flow Diagram of Experimental Procedures	24
IV	RESULTS AND DISCUSSION	25
	5.1 Mössbauer Spectroscopy	25
	5.1.1 Folded of Mössbauer Spectra	25
	5.1.2 Least-Squares fit of Mössbauer Spectra	32
	5.2 Scanning Electron Microscope	48
	5.3 Atomic Force Microscopy	51
	5.3.1 Surface Roughness Parameters	51
	5.4 X-ray Diffraction	57
	5.4.1 The First Crystallization	58
	5.4.2 The Second Crystallization	59
	5.4.3 Average grain size	61
	5.5 Differential Thermal Analysis	63
	5.6 Vibrating Sample Magnetometer	64
	5.7 Ferromagnetic Resonance	66
	5.7.1 Method of analysis of FMR	66
VI	CONCLUSIONS	75
	REFERENCES	77
	APPENDIX	84
	BIOGRAPHY	109

LIST OF TABLES

Table		Page
1.1	Application of high-permeability materials.	7
5.1	Mössbauer parameters of spectra of amorphous phase taken at room temperature.	33
5.2	Mössbauer parameters of $Fe_{40}Ni_{40}(Si+B)_{19}Mo_{1-2}$ amorphous ribbon after annealing at 450 °C taken at room temperature by MagDist Theory. ...	39
5.3	Mössbauer parameters of $Fe_{40}Ni_{40}(Si+B)_{19}Mo_{1-2}$ amorphous ribbon after annealing at 475 °C taken at room temperature by MagDist Theory. ...	40
5.4	Mössbauer parameters of $Fe_{40}Ni_{40}(Si+B)_{19}Mo_{1-2}$ Amorphous Ribbon after annealing at 500 °C taken at room temperature by MagDist Theory. ...	41
5.5	Areas of amorphous phase with increasing annealing temperature.	42
5.6	Fitted Mössbauer parameters of $Fe_{40}Ni_{40}(Si+B)_{19}Mo_{1-2}$ Amorphous Ribbon after annealing at 525 °C taken at room temperature by NSext Theory.	43
5.7	Mössbauer parameters of $Fe_{40}Ni_{40}(Si+B)_{19}Mo_{1-2}$ Amorphous Ribbon after annealing at 550 °C taken at room temperature by NSext Theory.	44
5.8	Mössbauer parameters of $Fe_{40}Ni_{40}(Si+B)_{19}Mo_{1-2}$ Amorphous Ribbon after annealing at 575 °C taken at room temperature by NSext Theory.	45
5.9	Mössbauer parameters of $Fe_{40}Ni_{40}(Si+B)_{19}Mo_{1-2}$ Amorphous Ribbon after annealing at 600 °C taken at room temperature by NSext Theory.	46
5.10	Percent area of crystalline phases at various annealing temperatures.	47
5.11	Rms roughness of $Fe_{40}Ni_{40}(Si+B)_{19}Mo_{1-2}$ at various annealing temperatures.	56
5.12	Calculated average crystalline diameter from Scherrer formula.	63
5.12	VSM results.	66

LIST OF FIGURES

Figure	Page
1.1 Melt-spinning apparatus schematic used to produce amorphous metallic ribbons.	4
1.2 Relationship between permeability, μ (at 1 kHz) and saturation Polarization for soft magnetic materials.	5
1.3 Flow chart for the considerations in designing and developing a Nanocrystalline soft magnetic from an amorphous precursor route.	6
1.4 A schematic representation at atomic structure of two-dimensional nanocrystalline material distinguishing between the atoms associated with the individual grain (solid circle) and those consulting the grain boundary network (open circle).	9
1.5 Schematic of the four types of nanocrystalline material classified according to integral modulation dimensionality.	9
1.6 Hypothetical free energy diagram to illustrate the nanocrystallization of amorphous solids. am, α and β are respectively the free energy curves of the amorphous phase, a terminal solid solution and an intermetallic phase.	13
4.1 Amorphous Ribbons of $\text{Fe}_{40}\text{Ni}_{40}(\text{Si+B})_{19}\text{Mo}_{1-2}$	18
4.2 Experimental Set up.	20
4.3 Mössbauer spectrum of α -Fe Foil taken at room temperature used for velocity calibration.	20
5.1(a) Mössbauer Spectrum of $\text{Fe}_{40}\text{Ni}_{40}(\text{Si+B})_{19}\text{Mo}_{1-2}$ amorphous ribbon before annealing under argon atmosphere.	26
5.1(b) Mössbauer Spectrum of $\text{Fe}_{40}\text{Ni}_{40}(\text{Si+B})_{19}\text{Mo}_{1-2}$ amorphous ribbon after annealing at 350°C under argon atmosphere.	26
5.1(c) Mössbauer Spectrum of $\text{Fe}_{40}\text{Ni}_{40}(\text{Si+B})_{19}\text{Mo}_{1-2}$ amorphous ribbon after annealing at 400°C under argon atmosphere.	27

LIST OF FIGURES(continued)

Figure	Page
5.1(d) Mössbauer Spectrum of $\text{Fe}_{40}\text{Ni}_{40}(\text{Si+B})_{19}\text{Mo}_{1-2}$ amorphous ribbon after annealing at 450°C under Argon atmosphere.	27
5.1(e) Mössbauer Spectrum of $\text{Fe}_{40}\text{Ni}_{40}(\text{Si+B})_{19}\text{Mo}_{1-2}$ amorphous ribbon after annealing at 475°C under Argon atmosphere.	28
5.1(f) Mössbauer Spectrum of $\text{Fe}_{40}\text{Ni}_{40}(\text{Si+B})_{19}\text{Mo}_{1-2}$ amorphous ribbon after annealing at 500°C under Argon atmosphere.	28
5.1(g) Mössbauer Spectrum of $\text{Fe}_{40}\text{Ni}_{40}(\text{Si+B})_{19}\text{Mo}_{1-2}$ amorphous ribbon after annealing at 525°C under Argon atmosphere.	29
5.1(h) Mössbauer Spectrum of $\text{Fe}_{40}\text{Ni}_{40}(\text{Si+B})_{19}\text{Mo}_{1-2}$ amorphous ribbon after annealing at 550°C under Argon atmosphere.	29
5.1(i) Mössbauer Spectrum of $\text{Fe}_{40}\text{Ni}_{40}(\text{Si+B})_{19}\text{Mo}_{1-2}$ amorphous ribbon after annealing at 575°C under Argon atmosphere.	30
5.1 (j) Mössbauer Spectrum of $\text{Fe}_{40}\text{Ni}_{40}(\text{Si+B})_{19}\text{Mo}_{1-2}$ amorphous ribbon after annealing at 600°C under Argon atmosphere.	30
5.2 Overlay of Mössbauer Spectra of annealed $\text{Fe}_{40}\text{Ni}_{40}(\text{Si+B})_{19}\text{Mo}_{1-2}$ amorphous ribbon.	31
5.3(a) Fitted Mössbauer Spectrum of $\text{Fe}_{40}\text{Ni}_{40}(\text{Si+B})_{19}\text{Mo}_{1-2}$ amorphous ribbon before annealing by NSing Theory.	34
5.3(b) Fitted Mössbauer Spectrum of $\text{Fe}_{40}\text{Ni}_{40}(\text{Si+B})_{19}\text{Mo}_{1-2}$ amorphous ribbon before annealing by MagDist Theory.	34
5.3(c) Fitted Mössbauer Spectrum of $\text{Fe}_{40}\text{Ni}_{40}(\text{Si+B})_{19}\text{Mo}_{1-2}$ amorphous ribbon after annealing at 350°C by NSing Theory.	35
5.3(d) Fitted Mössbauer Spectrum of $\text{Fe}_{40}\text{Ni}_{40}(\text{Si+B})_{19}\text{Mo}_{1-2}$ amorphous ribbon after annealing at 350°C by MagDist Theory.	35
5.3(e) Fitted Mössbauer Spectrum of $\text{Fe}_{40}\text{Ni}_{40}(\text{Si+B})_{19}\text{Mo}_{1-2}$ amorphous ribbon after annealing at 400°C by NSing Theory.	36

LIST OF FIGURES(continued)

Figure	Page
5.3(f) Fitted Mössbauer Spectrum of $\text{Fe}_{40}\text{Ni}_{40}(\text{Si}+\text{B})_{19}\text{Mo}_{1-2}$ amorphous ribbon after annealing at 400°C by MagDist Theory.	36
5.3(g) Histogram of Hyperfine Field Distribution of amorphous phase of $\text{Fe}_{40}\text{Ni}_{40}(\text{Si}+\text{B})_{19}\text{Mo}_{1-2}$ ribbon.	37
5.3 (h) Histogram of Hyperfine Field Distribution of amorphous phase of $\text{Fe}_{40}\text{Ni}_{40}(\text{Si}+\text{B})_{19}\text{Mo}_{1-2}$ ribbon after annealing at 350 °C.	37
5.3(i) Histogram of Hyperfine Field Distribution of amorphous phase of $\text{Fe}_{40}\text{Ni}_{40}(\text{Si}+\text{B})_{19}\text{Mo}_{1-2}$ ribbon after annealing at 400 °C.	38
5.3(j) Fitted Mössbauer Spectrum of $\text{Fe}_{40}\text{Ni}_{40}(\text{Si}+\text{B})_{19}\text{Mo}_{1-2}$ amorphous ribbon after annealing at 450°C by MagDist Theory.	39
5.3(k) Fitted Mössbauer Spectrum of $\text{Fe}_{40}\text{Ni}_{40}(\text{Si}+\text{B})_{19}\text{Mo}_{1-2}$ amorphous ribbon after annealing at 475°C by MagDist Theory.	40
5.3(l) Fitted Mössbauer Spectrum of $\text{Fe}_{40}\text{Ni}_{40}(\text{Si}+\text{B})_{19}\text{Mo}_{1-2}$ amorphous ribbon after annealing at 500°C by MagDist Theory.	41
5.3(m) Fitted Mössbauer Spectrum of $\text{Fe}_{40}\text{Ni}_{40}(\text{Si}+\text{B})_{19}\text{Mo}_{1-2}$ amorphous ribbon after annealing at 525°C by NSext Theory.	43
5.3(n) Fitted Mössbauer Spectrum of $\text{Fe}_{40}\text{Ni}_{40}(\text{Si}+\text{B})_{19}\text{Mo}_{1-2}$ amorphous ribbon after annealing at 550°C by NSext Theory.	44
5.3(o) Fitted Mössbauer Spectrum of $\text{Fe}_{40}\text{Ni}_{40}(\text{Si}+\text{B})_{19}\text{Mo}_{1-2}$ amorphous ribbon after annealing at 575°C by NSext Theory.	45
5.3(p) Fitted Mössbauer Spectrum of $\text{Fe}_{40}\text{Ni}_{40}(\text{Si}+\text{B})_{19}\text{Mo}_{1-2}$ amorphous ribbon after annealing at 600°C by NSext Theory.	46
5.3 Percent area of crystallized phases determined by fitting Mössbauer Spectra.	47
5.5(a) As-quenched of $\text{Fe}_{40}\text{Ni}_{40}(\text{Si}+\text{B})_{19}\text{Mo}_{1-2}$ amorphous ribbon..	49
5.5(b) $\text{Fe}_{40}\text{Ni}_{40}(\text{Si}+\text{B})_{19}\text{Mo}_{1-2}$ amorphous ribbon after annealing at 500 °C. ...	49
5.5(c) $\text{Fe}_{40}\text{Ni}_{40}(\text{Si}+\text{B})_{19}\text{Mo}_{1-2}$ amorphous ribbon after annealing at 525 °C. ...	49

LIST OF FIGURES(continued)

Figure	Page
5.5 (d) Fe ₄₀ Ni ₄₀ (Si+B) ₁₉ Mo ₁₋₂ amorphous ribbon after annealing at 550 °C. ...	49
5.5 (e) Fe ₄₀ Ni ₄₀ (Si+B) ₁₉ Mo ₁₋₂ amorphous ribbon after annealing at 575 °C. ...	50
5.5 (f) Fe ₄₀ Ni ₄₀ (Si+B) ₁₉ Mo ₁₋₂ amorphous ribbon after annealing at 600 °C. ...	50
5.6 Schematic of grain boundary of nanoparticles.	50
5.7(a) Tapping mode image of AFM scan of as-quenched sample.	52
5.7(b) Tapping mode image of AFM scan of of Fe ₄₀ Ni ₄₀ (Si+B) ₁₉ Mo ₁₋₂ ribbon after annealing at 450 °C.	53
5.7(c) Tapping mode image of AFM scan of of Fe ₄₀ Ni ₄₀ (Si+B) ₁₉ Mo ₁₋₂ ribbon after annealing at 500 °C.	54
5.7(d) Tapping mode image of AFM scan of of Fe ₄₀ Ni ₄₀ (Si+B) ₁₉ Mo ₁₋₂ ribbon after annealing at 550 °C.	55
5.8 XRD patterns of Fe ₄₀ Ni ₄₀ (Si+B) ₁₉ Mo ₁₋₂ amorphous ribbon annealed at different temperatures.	57
5.9(a) Amorphous phase of Fe ₄₀ Ni ₄₀ (Si+B) ₁₉ Mo ₁₋₂ ribbon.	58
5.9(b) Crystalline phases of partially crystallized of Fe ₄₀ Ni ₄₀ (Si+B) ₁₉ Mo ₁₋₂ ribbon.	59
5.9(c) Crystalline phases of completely crystallized of Fe ₄₀ Ni ₄₀ (Si+B) ₁₉ Mo ₁₋₂ ribbon.	60
5.10 Illustration of the effect of fine particle broadening in XRD (a) fine particles and (b) perfect crystal.	62
5.11(a) First DTA scan of Fe ₄₀ Ni ₄₀ (Si+B) ₁₉ Mo ₁₋₂ ribbon from 0 - 800 °C under argon atmosphere.	63
5.11(b) The second DTA scan of Fe ₄₀ Ni ₄₀ (Si+B) ₁₉ Mo ₁₋₂ ribbon from 0 - 800 °C under argon atmosphere.	64
5.12(a) Hysteresis loops taken at room temperature of Fe ₄₀ Ni ₄₀ (Si+B) ₁₉ Mo ₁₋₂ amorphous ribbon before annealing.	64
5.12(b) Hysteresis loops taken at room temperature of Fe ₄₀ Ni ₄₀ (Si+B) ₁₉ Mo ₁₋₂ amorphous ribbon after annealing at 450°C.	65

LIST OF FIGURES(continued)

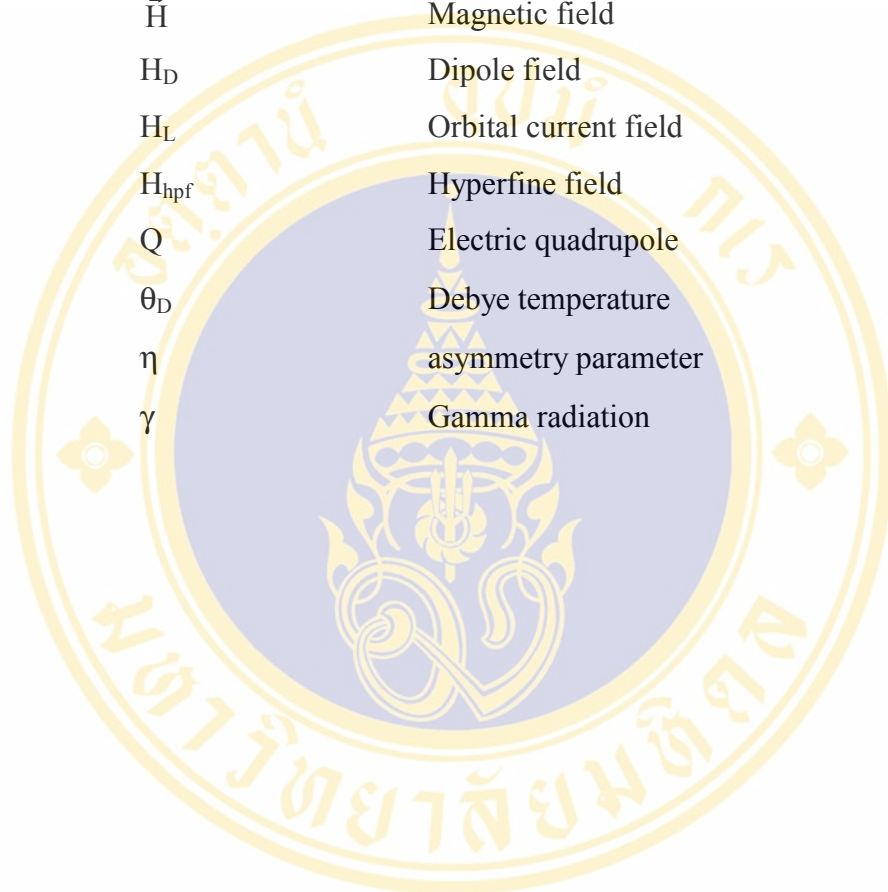
Figure	Page
5.12(c) Hysteresis loops taken at room temperature of $\text{Fe}_{40}\text{Ni}_{40}(\text{Si+B})_{19}\text{Mo}_{1-2}$ amorphous ribbon after annealing at 525°C	65
5.12(d) Hysteresis loops taken at room temperature of $\text{Fe}_{40}\text{Ni}_{40}(\text{Si+B})_{19}\text{Mo}_{1-2}$ amorphous ribbon after annealing at 600°C	66
5.13 Schematic illustrations of the coordinate system used in the analysis of FMR.	68
5.14(a) FMR spectra of $\text{Fe}_{40}\text{Ni}_{40}(\text{Si+B})_{19}\text{Mo}_{1-2}$ before annealing at various angles(ϕ) of the applied external field.	69
5.14(b) FMR spectra of $\text{Fe}_{40}\text{Ni}_{40}(\text{Si+B})_{19}\text{Mo}_{1-2}$ before annealing at various angles(θ) of the applied external field.	70
5.14(c) FMR spectra of $\text{Fe}_{40}\text{Ni}_{40}(\text{Si+B})_{19}\text{Mo}_{1-2}$ after annealing at 600°C at various angles(ϕ) of the applied external field.	71
5.14(d) FMR spectra of $\text{Fe}_{40}\text{Ni}_{40}(\text{Si+B})_{19}\text{Mo}_{1-2}$ after annealing at 600°C at various angles(θ) of the applied external field.	72
5.15 Schematic representation the direction of the magnetization, magnetic field and ribbon plane.	74

LIST OF ABBREVIATIONS

XRD	X-ray diffractometer
SEM	Scanning electron microscope
AFM	Atomic Force Microscopy
VSM	Vibrating sample analysis
FMR	Ferromagnetic resonance
DTA	Differential thermal analysis
n_{Fe}	Nearest-neighbor iron-57 atom
M_s	Saturation magnetization
H_c	Coercivity
σ	Specific saturation magnetization
S	Electron spin
IS	Isomer shift
Γ	Line width
B_θ	Breadth of the X-ray peak (Full Width at Half Maximum, FWHM)
δE_Q	Quadrupole splitting
E_e	Energy excited state
E_g	Energy ground state
E_γ	Energy of gamma ray
E_D	Doppler effect energy
E_R	Recoil energy
k_B	Boltzmann constant
k_γ	γ -ray wave vector
g	Nuclear factor
μ_n	Nuclear magnetons
\bar{I}	Nuclear spin
m_l	Magnetic quantum number
$\bar{\mu}$	Nuclear magnetic dipole

LIST OF ABBREVIATIONS (continued)

μ_B	Bohr magneton
h	Planck's constant
\vec{H}	Magnetic field
H_D	Dipole field
H_L	Orbital current field
H_{hpf}	Hyperfine field
Q	Electric quadrupole
θ_D	Debye temperature
η	asymmetry parameter
γ	Gamma radiation



CHAPTER I

INTRODUCTION

Magnetic materials have been an important part of technological advances of the past century. Most notable in recording media such as tapes and discs, they also have crucial roles in many other areas; motors, actuators, sensors and a variety of industrial processes. Magnetic materials are very important and highly sophisticated engineering materials. They play a fundamental role in many of the electrical and electronic systems that characterize modern society. Among the magnetic materials, permanent magnetic materials are those, which remain magnetized, while soft magnetic materials exhibit magnetic properties when, subjected to a magnetic field. Soft magnetic materials play a key role in power distribution, make possible the conversion between electrical and mechanical energy, underlie microwave communication, and provide both the transducers and the active storage material for data storage in information systems. Soft magnetic materials exhibit magnetic properties only when they are subjected to a magnetizing force such as the magnetic field created when current is passed through the wire surrounding a soft magnetic core. Soft ferromagnetic materials are generally associated with electrical circuits where they are used to amplify the flux generated by the electric currents. These materials can be used in a.c. as well as d.c. electrical circuits.

In the last few years the study of amorphous and nanocrystalline materials had been a topic of growing technological and scientific interest. As it is well known, the 3d-metal based amorphous alloys obtained by rapid-quenching of the melt are excellent soft magnetic materials, i.e. they exhibit very low value of the coercive field and relatively high saturation magnetization. Such magnetic softness originates from the absence of magnetocrystalline anisotropy in these alloys. Similarly, excellent magnetic softness of nanocrystalline alloys is related with the condition that the exchange correlation length is much higher than the average grain size

The amorphous ribbons obtained by the melt-spinning technique have widely been introduced as the soft magnetic materials in 1970s. Their excellent magnetic softness and high wear and corrosion resistance made them very attractive in recording head and microtransformer industries.

1.1 Amorphous Metal

Amorphous metals are materials with good electric and thermal conductivity with lustrous appearance and with other common metallic properties, but with atomic arrangements, which are not periodically ordered as, in more familiar crystalline metallic solids. Noncrystalline, amorphous and vitreous are equivalent terms used to describe solids in which atoms are not periodically arranged. The term 'glass' has often been reserved for amorphous solids formed by continuous solidification of a liquid, but metallic glasses are now commonly considered to include amorphous metals produced by various methods, including evaporation, sputtering and electro- and chemical deposition, as well as cooling from the liquid state.

The first report in which a range of amorphous, Brenner et al^[1], claimed to have made amorphous metallic materials by electrodepositing nickel-phosphorous materials. They observed only broad diffuse peak in the X-ray scattering pattern. Such alloys had been used for many years as hard wear and corrosion resistant coating. It was not until 1960 that Duwez^[2] and his coworker discovered a method of preparing amorphous alloys by direct quenching from the melt.

The production of amorphous metals by known techniques i.e., either through a rapid quench of the melt or by deposition, severely limits the form in which the amorphous metal can be obtained. For example, when the amorphous metal is obtained from the melt, the rapid quench has been achieved by spreading the molten alloy in a thin layer against a metal substrate such as Cu or Al held at below room temperature. Various procedures have been proposed to provide rapid quenching by spreading the molten liquid in a thin layer against a metal substrate. Typical examples of such techniques are the gun technique by P. Duwez and R.H. Willens^[2], in which a gaseous shock wave propels a drop of molten metal against substrate made of a metal

such as copper. The piston and anvil technique described by P. Pietrokowsky^[2,3] in which two metal plates come together rapidly and flatten out and quench a drop of molten metal falling between them. The casting technique described by R. Poud, Jr. and R. Maddin^[2], in which a molten metal stream impinges on the inner surface of a rapidly rotating hollow cylinder open at one end. Rotating double-roll technique described by H.S. Chen and C.E. Miller^[4], in which the molten metal is squirted into the nip of a pair of rapidly rotating metal rollers. This technique produces small foils or ribbon-shaped samples.

The first amorphous metal quenched directly from the melt was obtained by Duwez and his collaborators^[5], Au₈₀Si₂₀. This amorphous was not stable at room temperature and was not suitable to analyze it. Soon after the first discovery of a liquid - quenched amorphous metallic system, Cohen and Turbell^[6] pointed out that eutectic temperature was in part responsible for glass formation in metallic systems. A new glassy phase was found in Pd-Si system containing 15-23 at % Si. The discovery of this system is important for the following reasons. First, The Pd – Si glassy system is stable at room temperature with crystallization temperature more than 400 °C and secondly, the element Pd is a transition metal and can be partially replaced by other transition metals.

The most important series^[7] of amorphous alloys based on the composition T_{100-x}M_x where T is one or more of such transition metals as Fe, Ni, Co, Mo, Pd etc. and M is one or more of the metalloids or glass forming elements, P, B Si or C.

These alloys have attracted a great deal of research effort. They are potentially useful as high magnetic- permeability alloy with comparable or superior properties.

1.1.1 Preparation of Amorphous Ribbons.

Amorphous ferromagnetic alloys usually contain one or more ferromagnetic transition metals Fe, Ni, Co, Mo and glass-forming elements Si, B, P or C which increase the viscosity and its temperature dependence of the liquid alloy.

The alloys are melt under an inert atmosphere to prevent oxidation They are then injected into a cold copper drum which is rotating at high speed as shown in Fig. 1.1, so that if the molten alloy is cooled sufficiently rapidly, causing a large increase in the

viscosity, which impedes the rearrangement of atom. This results in the formation of an amorphous material, at low temperatures or ambient temperatures, the material may exist in the amorphous state almost indefinitely.

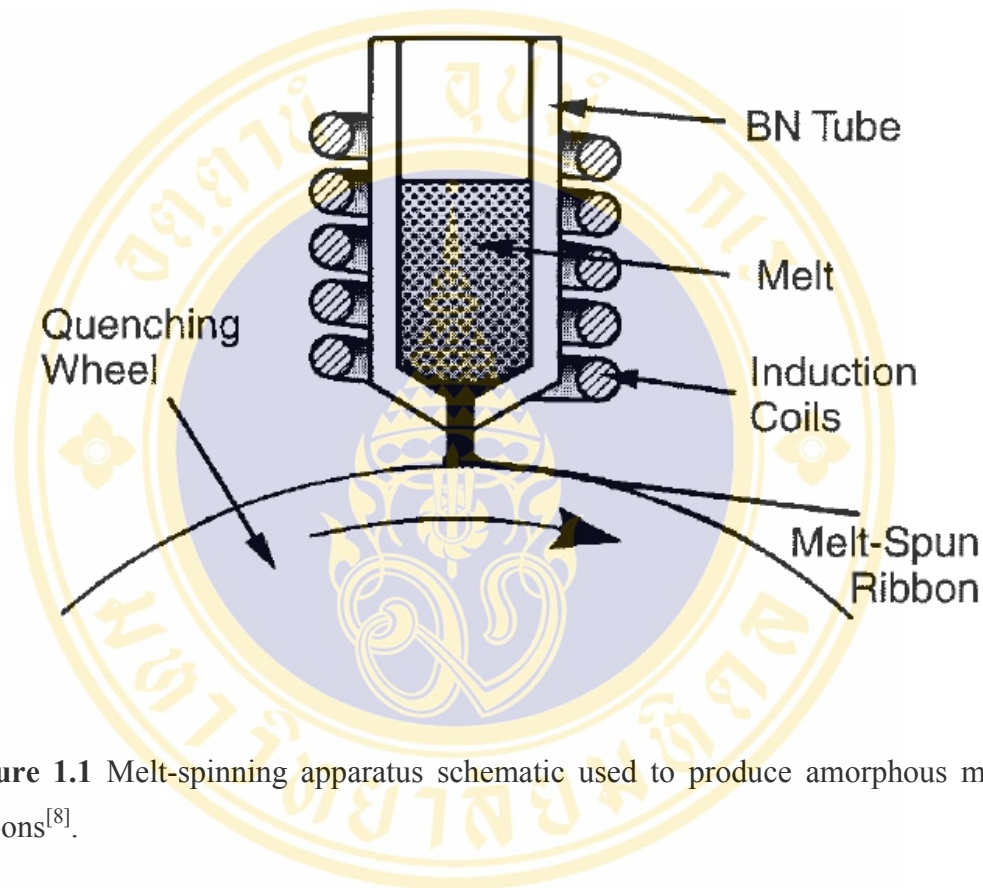


Figure 1.1 Melt-spinning apparatus schematic used to produce amorphous metallic ribbons^[8].

1.1.2 Applications of Amorphous Materials

The excellent soft magnetic properties noted from these materials namely - extremely low coercivities, high permeabilities, low energy losses, etc. -- has triggered major interest and research activity in both the academic, research community and the industrial community. Figure 1.2 shows relationship between saturation polarization for soft magnetic materials. Additionally, these Fe-based materials have potential as lower cost alternatives to the costly Co-based amorphous materials in many applications. The application of these materials as cores of transformers in switched-mode power supplies, chokes, etc., are already well on their way to commercialization. Other applications in high accuracy current transformers, ground fault interrupters,

etc., are being investigated. The applications of these materials that have the greatest cost and performance impact, and yet are the most challenging, are in cores of transformers for electrical power distribution. This is the application that needs to be facilitated through additional work on nanocrystalline soft magnetic alloys.

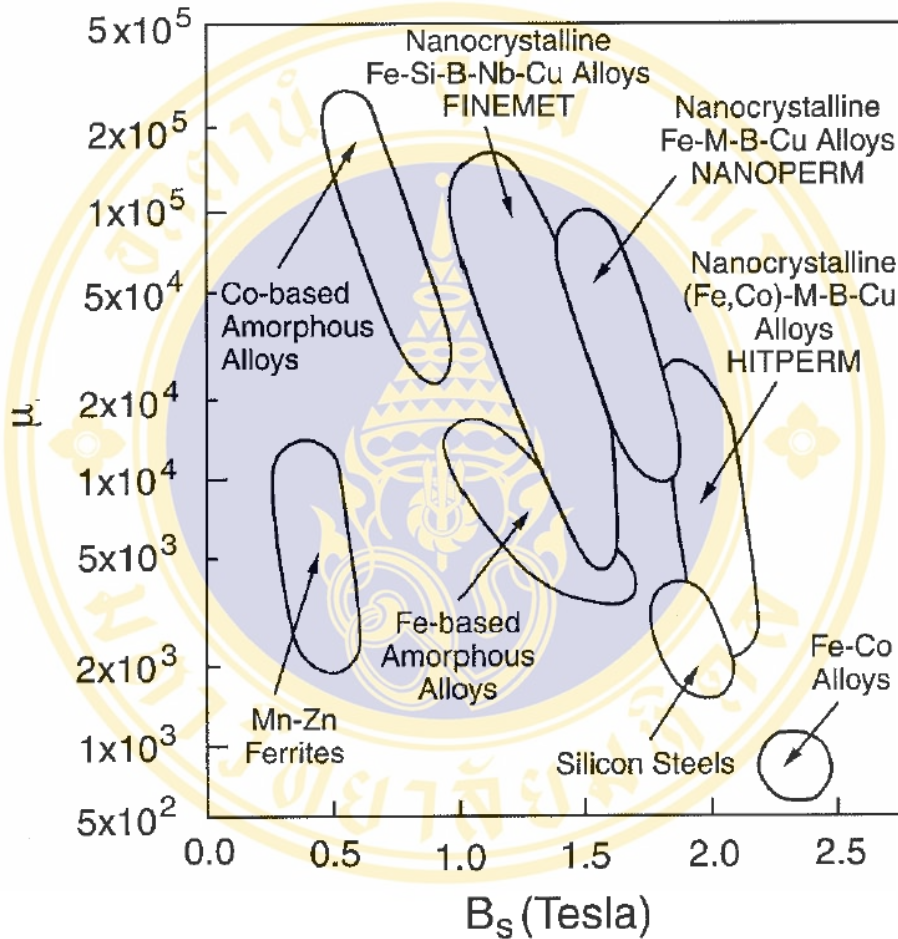


Figure 1.2 Relationship between permeability, μ (at 1 kHz) and saturation polarization for soft magnetic materials.

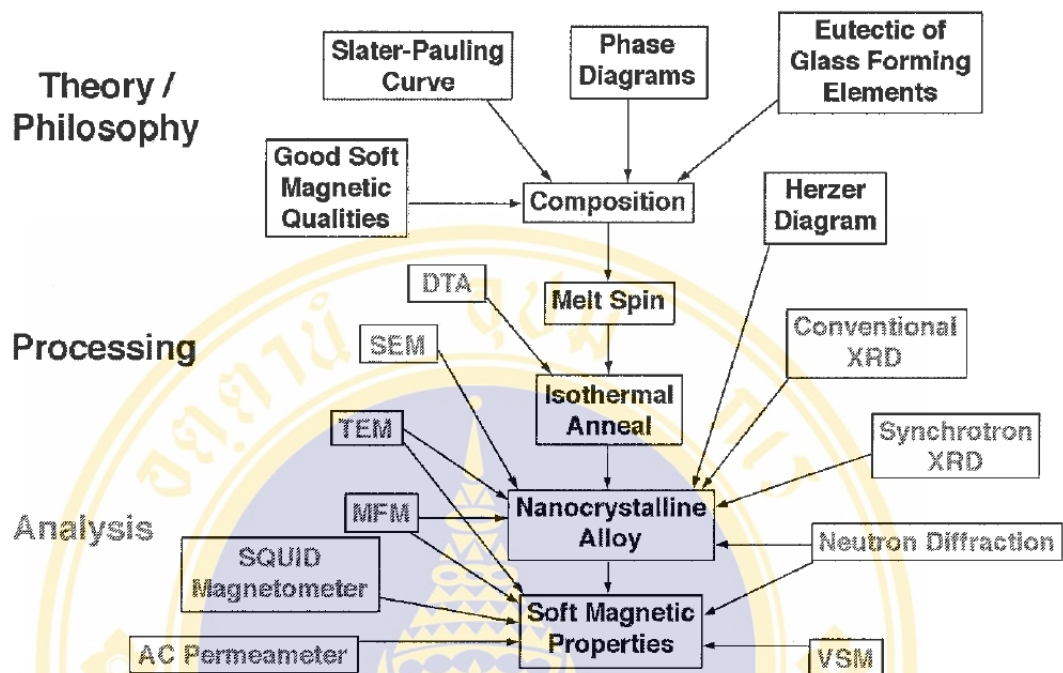


Figure 1.3 Flow chart for the considerations in designing and developing a nanocrystalline soft magnetic material from an amorphous precursor route.

Table 1.1 Applications of high-permeability materials.

Power applications	
Applications	Requirements
Distribution and power transformer	Low core losses, high permeability, high saturation magnetic polarization
High-quality motors and generators, stators and armatures, switched-mode power supplies	
Instrument transformers	
Applications	Requirements
Audiofrequency transformer	Low core losses, high permeability, high saturation magnetic polarization
Pulse transformer	High permeability
Cores for inductor coils	
Applications	Requirements
Audiofrequency	Low hysteresis, high permeability
Carrier frequency	Very low hysteresis and eddy current loss
Radiofrequency	High permeability at low fields
Miscellaneous	
Applications	Requirements
Relays, switches	High permeability, low remanence, low coercivity
Earth leakage circuit	
Magnetic shielding	Low core loss for AC applications
Magnetic recording heads	High initial permeability, low or zero remanence
Magnetic amplifiers	Rectangular hysteresis loops, low hysteresis loss
Saturable reactors	
Saturable transformer	
Transformer cores	
Magnetic shunts for temperature compensation in magnetic circuits	Low Curie temperature, appropriate decrease in permeability with increase temperature
Electromagnets in indicating instruments, fire detection, quartz watches, electro-mechanical devices	High permeability, high saturation magnetic polarization
Magnetic yokes in permanent magnet devices, such as lifting and holding magnets, loudspeaker	High permeability, high saturation magnetic polarization

1.2 Nanocrystalline Materials

Nanocrystalline materials are single- or multi- phase polycrystals with grain sizes in the nanometer region. Many properties of nanocrystalline materials are found to be fundamentally different from and often superior to those of the conventional polycrystals and the amorphous solids. For example, nanocrystalline materials may exhibit increased strength/hardness, impressed ductility/toughness, reduced elastic modulus, enhanced diffusivity, higher specific heat, enhanced thermal expansion coefficient and superior soft magnetic properties in comparison with conventional polycrystalline materials. In particular, the nanocrystalline structure might be significant in the improvement of ductility in brittle materials such as ceramics and some intermetallics. The basic idea of nanocrystalline materials was proposed by Gleiter^[9] in 1981, this involved generating a new class of materials by introducing such a high density of grain boundaries. Figure 1.4 shows a schematic illustration of a hard-sphere two-dimensional model of a hypothetical nanocrystalline structure: crystal atoms with neighbor configuration corresponding to the lattice and boundary atoms with a variety of interatomic spacing. Nanocrystalline materials can be classified into several categories according to the nanostructure dimensionality. They can be zero-dimensionality atom clusters and cluster assemblies, one- and two- dimensionally modulated multilayered and overlayers respectively and three- dimensional equiaxed nanocrystalline structures as indicated schematically in Figure 1.5. The nanocrystalline materials may contain crystalline, quasi - crystalline, or amorphous phases (sometimes called 'nanoglasses') and can be metal, intermetallic ceramics, semiconductors and composites. In recent years, most attention has been concentrated on the three - dimensional nanocrystalline material which are expected to find applications and based on their improved mechanical, magnetic and other properties. Pioneering explorations to synthesize nanocrystalline samples artificially were performed in Gleiter's group in the early 1980s^[10]. They synthesized ultrafine metallic particles using an inert gas condensation technique and consolidated them in situ into small disks under ultra-high vacuum conditions.

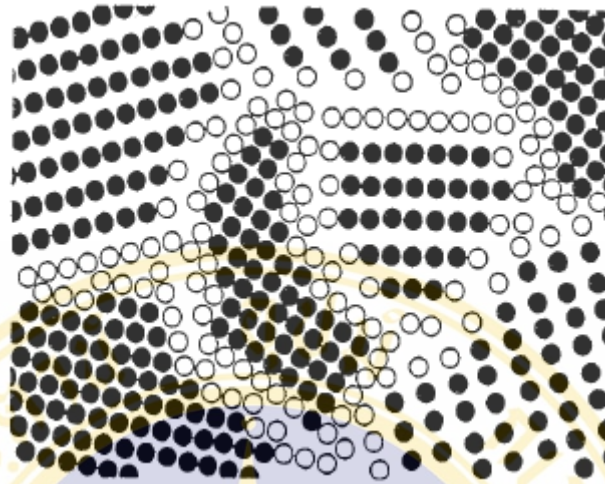


Figure 1.4 Schematic representation at atomic structure of two-dimensional nanocrystalline material distinguishing between the atoms associated with the individual grain (solid circle) and those consulting the grain boundary network (open circle).

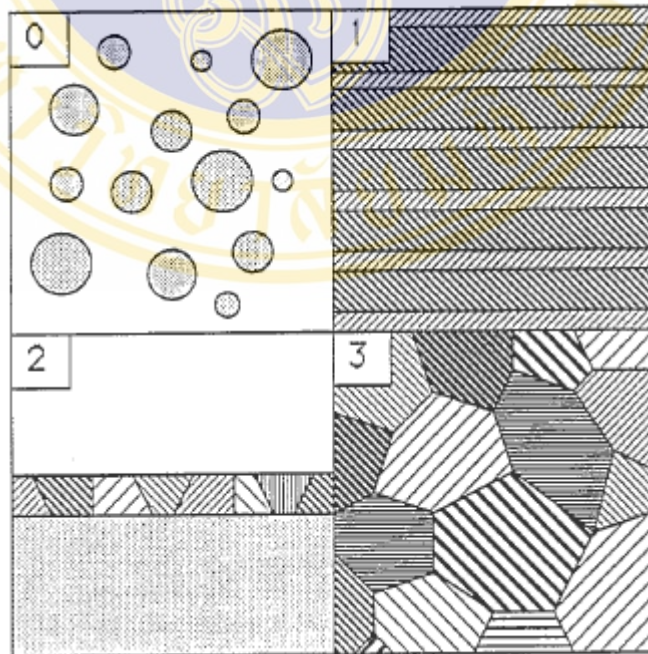


Figure 1.5 Schematic picture of the four types of nanocrystalline material classified according to integral modulation dimensionality.

Several different techniques can be used to synthesize nanocrystalline materials from starting materials in solid, liquid or glasses states. They include mechanical attrition (or mechanical alloying), spray conversion processing, severe plastic deformation, sputtering, electro-depositing, spark erosion rapid quenching and the complete crystallization of amorphous solids^[10]. Most well-known synthesis methods are those of mechanical alloying and crystallization technique. The basic principle for the crystallization method from amorphous solid is to control the crystallization kinetics by optimizing the heat treatment conditions (annealing temperature, time heating rate, etc.) so that the amorphous phase crystallized partially or completely into a crystalline material with ultrafine crystallites. The amorphous solids can be prepared by means of the existing routes, such as melt-spinning, splat-quenching, mechanical alloying, vapor deposition or electro-deposition, etc. Crystallization of amorphous solid has been successfully applied in producing nanometer-sized grains, e.g. on Fe-, Ni- and Co-based alloy^[10,11,12]. The complete crystallization of amorphous solids is being established as a promising method for synthesis of nanocrystalline materials because it possessed some unique advantages:

- (i) It is very simple and convenient to control in preparation procedures. Conventional annealing can realize the nanocrystallization in most alloy and element systems providing that they form into the amorphous state and can produce large quantities of nanocrystalline samples. Also, variable grain sizes with a wide size range (from a few nanometers to submicrometers) can be easily obtained by modifying the heat-treatment conditions.
- (ii) The complete crystallization method is an efficient way to produce porosity-free nanocrystalline materials^[13]. As no artificial consolidation process is involved and the nanometer-crystallites and their boundaries are formed via a solid state phase transformation, the nanocrystalline sample is dense and clean in the internal interfaces.
- (iii) Its capability to create different kinds of interfacial structure in the nanocrystalline material provides more opportunities for exploration of the nature of these nanocrystalline interfaces.
- (iv) By using of the crystallization method, some nanocrystalline intermetallics, supersaturated metallic solid solutions and composites can be easily synthesized

(v) The nanocrystallization itself provide us with a unique chance to study the interface formation process from the amorphous state experimentally. The nanocrystallization kinetics and thermodynamics of the amorphous solids are strongly affected by the presence of plenty of interfaces in the crystallization product. Consequently, it is possible to reveal some fundamental features of the interfaces in the nanocrystalline materials from the transformation kinetics and thermodynamics signals.

The controlled crystallization of amorphous alloys can be used to obtain partially crystallized materials with nanometer-sized crystallites embedded in the residual amorphous matrix. This special nanocrystal/amorphous composite structure with appropriate compositions allows the materials to exhibit excellent mechanical or magnetic properties. The Fe-Cu-Nb-Si-B alloys are a good sample, which was first, investigated by Yoshizawa and co-workers^[14], later by Herzer and others^[15].

1.2.1 Nanocrystallization

The amorphous solids are in thermodynamically metastable states and they can transform into more stable states under appropriate circumstances. Crystallization is a transformation from an amorphous phase into one or more metastable or stable polycrystalline phases. The driving force for the crystallization is the Gibbs free energy difference between the amorphous and the crystalline phases, when amorphous solids are subjected to heat treatment, irradiation, or mechanical alloying^[16]. Conventional thermal annealing is the most commonly utilized investigation on crystallization behavior of amorphous solids. The dimension of crystallites ranges from a few nanometers to a few micrometers and depends on the chemical composition of the amorphous materials and annealing conditions. The crystallization of amorphous solids into nanometer-sized polycrystalline phases is referred as "nanocrystallization". Nanocrystallization can be realized upon isothermal and anisothermal annealing in various amorphous solids of metallic alloys.

1.2.2 Nanocrystallization products

The phase and morphologies of nanocrystallization products are dominated by the transformation mechanism, which is closely related to chemical compositions of amorphous state and thermodynamic properties of the corresponding crystalline phases. During conventional crystallization of amorphous solids, three different types of transformation namely, polymorphous, eutectic and primary crystallization are identified depending on their chemical compositions, as described by Köster and co-workers^[17]. Similarly, all of these three types of transformation have been observed in nanocrystallization of amorphous solids in different systems. Fig 1.6 shows a hypothetical free energy diagram to illustrate these reactions occurring during nanocrystallization of the amorphous solids. The variation of free energy with composition of the glass and various nanocrystalline phases (in these case, two nanophases, a solid solution α and a compound β , are included) at a chosen annealing temperature is represented.

Polymorphous nanocrystallization is the process that an amorphous phase crystallizes into a single nanocrystalline phase of same chemical composition. This reaction can occur only in concentration ranges near the compound (C_1 in Fig.1.6) or the pure element (C_2). The polymorphous nanocrystallization (reaction (1) or (2)) may produce a single compound phase (β) or a supersaturated solid solution nanophase (α).

Eutectic nanocrystallization is the process that an amorphous phase crystallizes into two nanocrystalline phase simultaneously (e.g. reaction (3): $\alpha+\beta$), during which two nanophases grow in a coupled fashion analogously to the eutectic crystallization of liquids. The reaction has the main driving force and the overall composition of the two phases remains the same as that amorphous matrix. The eutectic nanocrystallization can occur within a concentration range around the equilibrium eutectic composition, rather than a specific eutectic composition as in the conventional crystallization. A possible reason might be that the nanocrystalline material contains a large amount of interface that may have higher energetic configurations and thus allow a relatively wide composition range.

Primary nanocrystallization is the process when an amorphous phase, with a composition deviating from that for either the eutectic or the polymorphous reaction

(C_4 in Fig 1.6), in the first step crystallizes into a primary nanophase embedded in the amorphous matrix. The residual amorphous phase crystallizes, in the second step, into nanophases in the mechanism of either the eutectic or the polymorphous nanocrystallization.

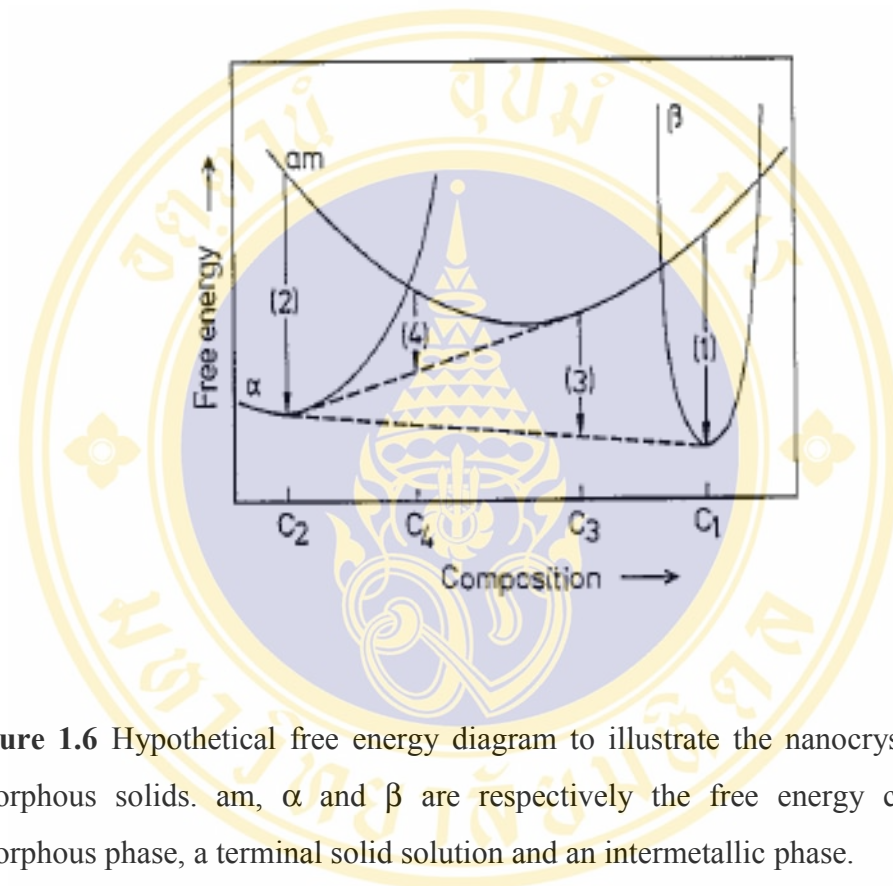


Figure 1.6 Hypothetical free energy diagram to illustrate the nanocrystallization of amorphous solids. am, α and β are respectively the free energy curves of the amorphous phase, a terminal solid solution and an intermetallic phase.

CHAPTER II

OBJECTIVE

The goal of this research is to study the crystallization behaviour of amorphous ribbon of $\text{Fe}_{40}\text{Ni}_{40}(\text{Si+B})_{19}\text{Mo}_{1-2}$ by annealing it under argon atmosphere in temperature range of $350\text{ }^{\circ}\text{C} - 600\text{ }^{\circ}\text{C}$. Under the thermal process the amorphous phase can be transformed to more ordered crystalline phases of iron-based compounds which can be monitored by various techniques. Nanocrystalline magnetic structures may be achieved at low temperature annealing between $450\text{ }^{\circ}\text{C} - 500\text{ }^{\circ}\text{C}$. ^{57}Fe Mössbauer spectroscopy is used to follow the evolution of magnetic structures of these compounds. Mössbauer spectra will be analyzed by PC-Mos II software package. X-ray diffraction (XRD) technique is employed to confirm phase changes and to detect any non iron-based structure which can not be observed by ^{57}Fe Mössbauer spectroscopy. Average grain size analysis will be determined by scanning electron microscope (SEM) and Scherrer formula (XRD pattern analysis). A differential thermal analyzer (DTA) will be used to monitor crystallization temperatures of the primary crystallization and the secondary crystallization of the residual matrix. Furthermore, some magnetic properties will be examined by ferromagnetic resonance (FMR) and a vibrating sample magnetometer (VSM).

CHAPTER III

LITERATURE

The crystallization of amorphous metals has been studied mainly in Fe-based amorphous alloys because of their novel magnetic properties in the nanocrystalline state. Many techniques were used to investigate Fe-based amorphous alloys. The properties of amorphous and crystalline phase of Fe-B^[18-25], Fe-B-Si^[26-32], Fe-B-Si-C^[33-38] have been reported. F.H. Sánchez^[21] and co-worker had studied the crystallization behavior of Fe_{100-x}B_x amorphous alloys by heating process. The results indicated that the annealed alloys gave *t*-Fe₂B (*t* stands for tetragonal), *o*-Fe₃B (*o* stands for orthorhombic), *t*-Fe₃B and structures. P.Ruuskanan^[22] and J.Balogh^[23] studied the same series but made by mechanical alloying. M. Arshed^[24] and co-worker had studied annealed Fe-B system, they found that type of Fe-B compound depended on the B concentration. The Fe₂B compound was observed at a low B concentration while the Fe₃B compound was found at a high concentration of B. In comparison, Fe-B-Si systems^[26-32] showed similar crystallization behavior to the Fe-B system but a new phase, α-Fe(Si) was found. The influence of other elements replacing of Fe element in amorphous alloy such as Ni, Co, Sm and Al have been studied by several researchers^[39-60]. The addition of Cu acts as a nucleating agent whereas Nb and Mo inhibit the grain growth of α-Fe(Si) phases that crystallize from amorphous matrix. On the other hand, Nb and Mo enhance the thermal stability of residual amorphous phase, consequently the borides are hard to precipitate. The Fe-B-Si alloy loses its soft magnetic properties when it is induced to crystallize. The addition of the inhibitors can prevent residual amorphous from crystallization.

The basic magnetic properties of amorphous ribbons may be carried out by several experimental techniques such as HysteresisGraph, SQUID (Superconducting Quantum Interference Device) Magnetometer and VSM (Vibrating Sample Magnetometer). In recent years, their properties were measured by a broad band ferromagnetic resonance spectrometer (FMR) and determined *g*-factor, magnetic

anisotropy, magnetic coupling damping information, etc. R.S. Biasi^[61-62] successfully applied the FMR technique to investigate the crystalline behavior of Co-based amorphous ribbons. D.S. Schmool and J.M. Barandiaran^[63] performed FMR on Fe-Cu-Nb-Si-B, Fe-Zr-Cu-B system and gave a theory consideration on multiphase ferromagnet. Some works on FMR technique have been studied by several researchers^[64-72].



CHAPTER IV

EXPERIMENTAL METHODS

4.1 Instruments

The instruments used in this experiment are listed below:

- Mössbauer Spectrometer (Model MR-351)
- X-ray Diffractometer (Bruker, Model D8 Advanced)
- Scanning Electron Microscope (JEOL, Model JSM-6301F)
- Atomic Force Microscopy (Digital Instruments Dimension 3100)
- Differential Thermal Analysis (NETZSCH, Model STA 409 C)
- Furnace (Lenton, Model EHF 18/5)
- Electron Spin Resonance Spectrometer (JEOL, Model JES-RE2X)
- Vibrating Sample Magnetometer (Lakeshore 7300)

4.2 Materials

The amorphous ribbon of $\text{Fe}_{40}\text{Ni}_{40}(\text{Si+B})_{19}\text{Mo}_{1-2}$ has been prepared by melt spinning technique purchased from Good Fellow Company.

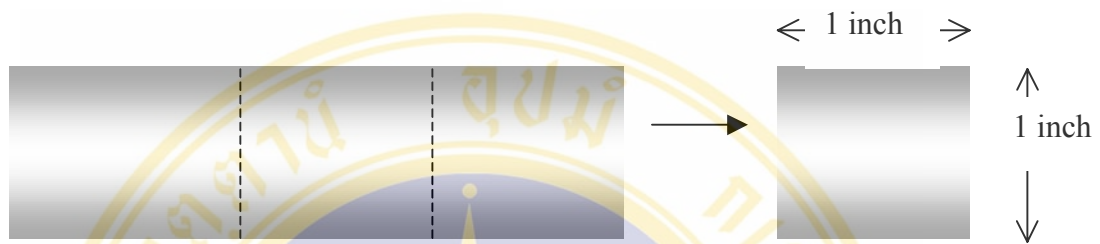


Figure 4.1 Amorphous Ribbon $\text{Fe}_{40}\text{Ni}_{40}(\text{Si+B})_{19}\text{Mo}_{1-2}$

4.2.1 Annealing of the $\text{Fe}_{40}\text{Ni}_{40}(\text{Si+B})_{19}\text{Mo}_{1-2}$

Amorphous ribbons of $\text{Fe}_{40}\text{Ni}_{40}(\text{Si+B})_{19}\text{Mo}_{1-2}$ were cut into one inch wide and one inch long strips and annealed in an argon atmosphere in the Lenton furnace with the heating rate of 5 °C per minute. Nine amorphous ribbons were separately subjected to isothermal treatments for two hours at 350 °C, 400 °C, 450 °C, 475 °C, 500 °C, 525° C, 550 °C, 575 °C and 600 °C respectively. The treatments were performed under argon atmosphere to avoid oxidation of the materials. After completing the heat treatment, the samples were slowly cooled down to room temperature in the furnace.

4.3 Mössbauer Spectroscopy

Mössbauer spectra of the samples were collected at room temperature (~ 300 K) with a constant acceleration spectrometer using ^{57}Co source. The velocity of the source must be calibrated by using a natural $\alpha\text{-Fe}$ foil before these data could be analyzed. Transmission spectra were least-squares fitted to Lorentzian line shapes for Mössbauer parameters of crystallized phases by PC-Mos II software. The software was developed by Gerhard Grobe, which could generally iterate and optimize within a certain number of iterations. Mössbauer data for each sample were accumulated over twenty four hours or approximately one million counts per channel.

4.3.1 Calibration of the Mössbauer Analyzer.

In experiment, a ^{57}Co source was placed on the transducer. A Doppler effect was caused by the Mössbauer source, the energy of the Mössbauer source would be $E + E_\gamma(1 + \frac{v}{c})$ where v is the velocity of the transducer and c is the velocity of light.

Since there is a Zeeman splitting of the nuclear levels, the absorption takes at six different energies. The Doppler shift energy is related to the transition energy by

$$E = (1 + \frac{v}{c}) E_\gamma = E'_\gamma - H \left(\frac{\mu_e m_e}{I_e} - \frac{\mu_g m_g}{I_g} \right)$$

Here E'_γ takes into account the isomer shift already. H is the internal magnetic field at the nucleus, μ_e and μ_g are the magnetic moments of the excited and the ground states respectively. m_e and m_g are the magnetic quantum numbers having $(2I_e + 1)$ and $(2I_g + 1)$ values. I_e and I_g are the nuclear spins of the excited and ground states respectively. Thus if μ_g and the velocity of source are known, then H and μ_e can be calculated from the line positions of $(\frac{3}{2} \rightarrow \frac{1}{2})$, $(\frac{1}{2} \rightarrow \frac{1}{2})$ and $(\frac{1}{2} \rightarrow -\frac{1}{2})$ transitions. μ_g of ^{57}Fe has been accurately determined to be 0.0903 ± 0.0007 nuclear magneton. The hyperfine field at the ^{57}Fe nuclei of a natural iron foil has been carefully measured by Miglierini et al^[73-74] and has given the value of 330 kOe. They simulated the Mössbauer spectra of nanocrystallines Fe-Cu-Nb-Si-B and Fe(Cu)ZrB alloys.

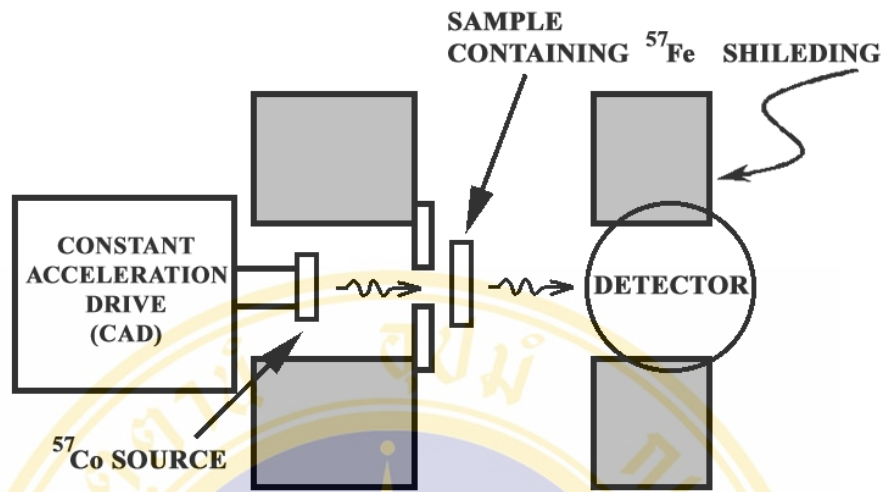


Figure 4.2 Experimental Set up

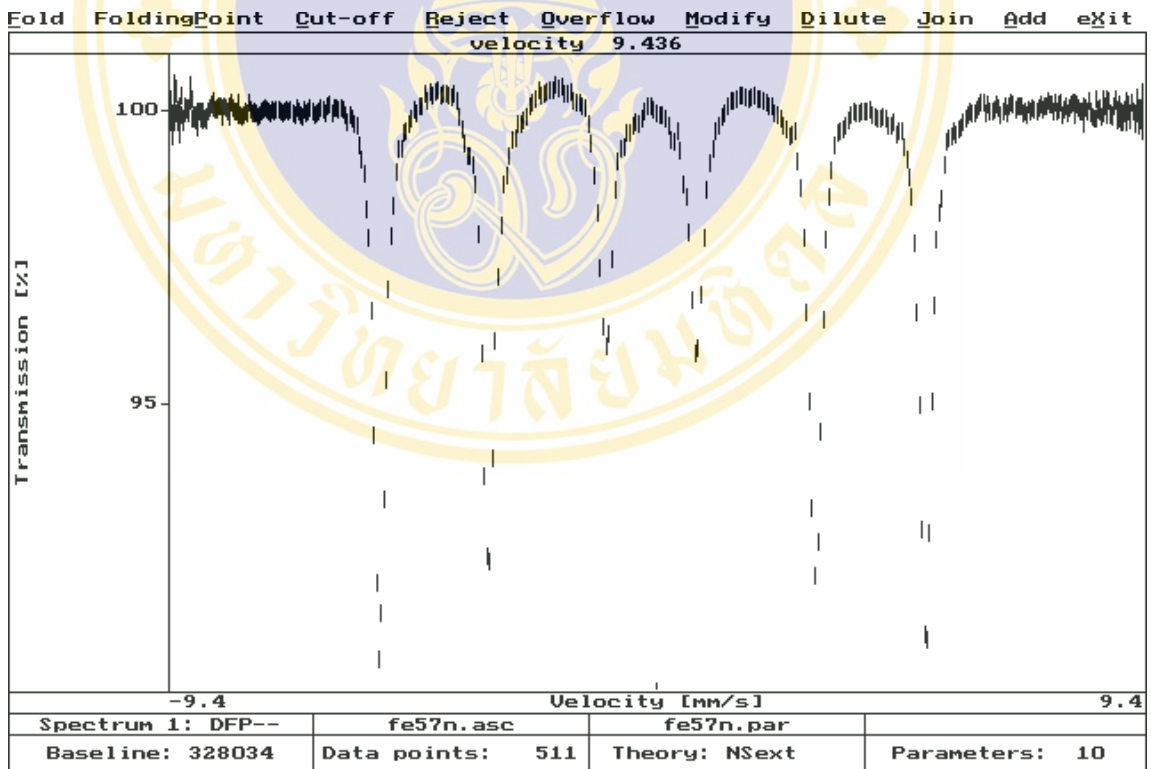


Figure 4.3 Mössbauer spectrum of α -Fe Foil at room temperature used for velocity calibration.

4.3.2 Fitting Procedures For the Mössbauer Spectra in $\text{Fe}_{40}\text{Ni}_{40}(\text{Si+B})_{19}\text{Mo}_{1-2}$ Amorphous Ribbons.

The evaluation of Mössbauer parameters can be accomplished by fitting of a theoretically motivated curve to the measured spectrum. A least-squares fit routine also lies in the heart of PC-Mos II. The advantage of PC-Mos II is the ability to fit more than one subspectra simultaneously. The suffix files .asc, .par and .hdr must be created for PC Mos II first. Then the computer software will read the count rate of spectrum (which are in suffix file .asc) and corresponding channel numbers. An initial guess of Mössbauer parameters from a theoretical curve must be put into a .par suffix file. In crystalline phases in which there are magnetic orders, a sextet normally arise from the Mössbauer transitions of ^{57}Fe nuclei in a strong hyperfine field. Each equivalent site of ^{57}Fe will give rise to one sextet. For N different sites, one has N overlapping sextets and Nsext subroutine is needed for fitting. It builds theoretical curve from N (magnetic) sextets of Lorentzians curves. The relative intensities of the Lorentzians are calculated under the assumption of polycrystalline specimens. For an amorphous phase, the MagDist subroutine is used to builds its theoretical curve from a distribution of magnetic fields experienced by ^{57}Fe nuclei. If the spectra are from partially crystallized phases, the MagDist may be used to fit a theoretical curve describing a certain number of sextets and doublets. The spectrum from the theoretical curve has to be very close to the experimental one. The amounts of irons in crystalline phases are taken to be proportional to their absorption areas. The distribution of hyperfine field enables a better visualization of the evolution of the Mössbauer spectra with the annealing temperature and duration of heat treatment.

4.4 Scanning Electron Microscopy (SEM)

Scanning electron microscope (SEM) observations were carried out with the acceleration voltage of 15 kV, in a JEOL Scanning Electron Microscope (Model JSM-6301F). The samples were cut into 3 mm^2 and placed on sample stub by two-sided sticky tape. The magnification of seven thousand was selected for SEM photograph. At this magnification, grains of various sizes in the samples could be easily observed.

4.5 Atomic Force Microscopy (AFM)

Tapping Mode AFM studies were performed using a Digital Instruments Dimension 3100. In these experiments, the samples were cut into 3 mm² and placed on sample stub and a scanned size of 5 μm² was selected. The scan speed of one Hz to determine surface roughness was chosen.

4.6 X-ray Diffraction (XRD)

X-ray diffraction patterns of Fe₄₀Ni₄₀(Si+B)₁₉Mo₁₋₂ ribbons were obtained by using the Bruker AXS D8 Advance powder diffractometer which was controlled by the latest DIFFRAC PLUS software and linked to the 2000 release of the PDF-2 database, with step angle of 0.03 degree per second from 2θ of 20 to 110 degrees (CuKα radiation, 30 kV/ 30 mA). The spectra of all Fe₄₀Ni₄₀(Si+B)₁₉Mo₁₋₂ ribbons, can be identified them as amorphous or crystalline phases depending on the annealing temperature.

4.7 Differential Thermal Analysis (DTA)

The DTA analysis was made by Simultaneous Thermal Analyzer Netzsch STA 409. The ribbon was first heated from room temperature up to 800 °C and cooled down to room temperature and heated again up to the same temperature to detect any remaining amorphous phase. To prevent oxidation these experiments were performed under argon atmosphere with a slow heating rate of 5 °C/min. The second heating was carried out in similar operating conditions and immediately after the first heat treatment. The second experimental data were used as the baseline of the first heating process.

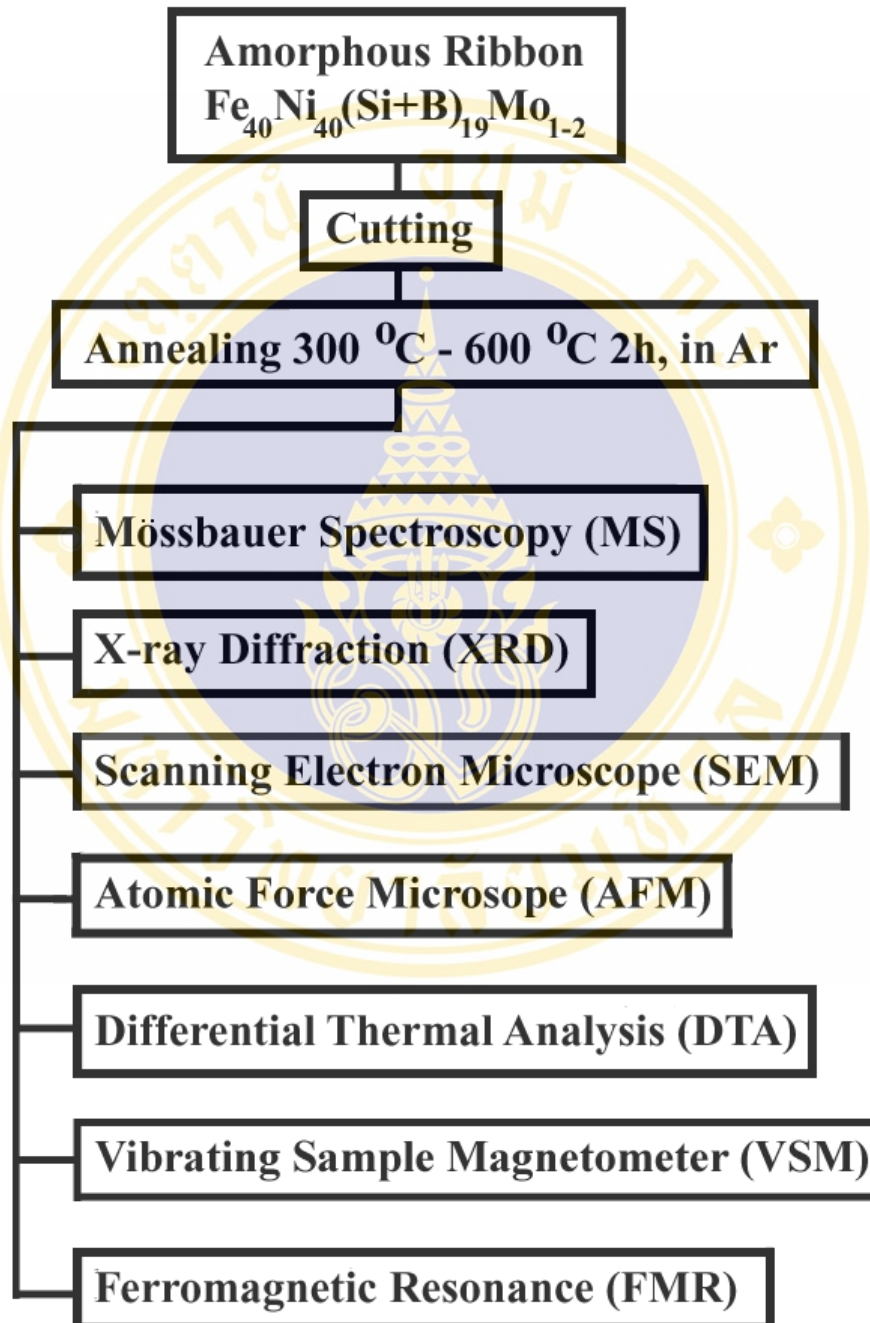
4.8 Ferromagnetic Resonance (FMR)

Ferromagnetic resonance experiments were performed at room temperature at a fixed microwave frequency of ~ 9.5 GHz (X-band), in a JEOL ESR spectrometer. The magnetic field was modulated by 0.5 mT at 100 kHz. The samples were mounted on a very clean sample tube with a goniometer attached and put in a resonant measuring cavity of the apparatus such that the externally applied static field was in the plane of the sample. There were two sets of experiments, the first with the magnetic field was in the perpendicular direction to the sample plane and the second with the magnetic field was in the plane. The goniometer allowed full sample rotations about a chosen axis.

4.9 Vibrating sample magnetometer (VSM)

Macroscopic magnetization measurements were performed in a vibrating sample magnetometer (VSM) in the applied magnetic field perpendicular to the film plane upto 10000 Oe under room temperature. The magnetization (M_s) and coercive field (H_c) were calculated from the hysteresis loops.

4.10 Flow Diagram of Experimental Procedures



CHAPTER V

RESULTS AND DISCUSSION

5.1 Mössbauer Spectroscopy

5.1.1 Folded of Mössbauer Spectra

Mössbauer spectra that were collected from annealed samples at 350 °C, 400 °C, 450 °C, 475 °C, 500 °C, 525 °C, 550 °C, 575 °C, and 600 °C clearly exhibited the behavior of crystallization processes. Figures 5.1 (a)-(j) represented spectra of $\text{Fe}_{40}\text{Ni}_{40}(\text{Si}+\text{B})_{19}\text{Mo}_{1-2}$ ribbons at each annealing temperature. All spectra were measured at room temperature for a period of 2 hours. They were least-squares fit to find Mössbauer parameters.

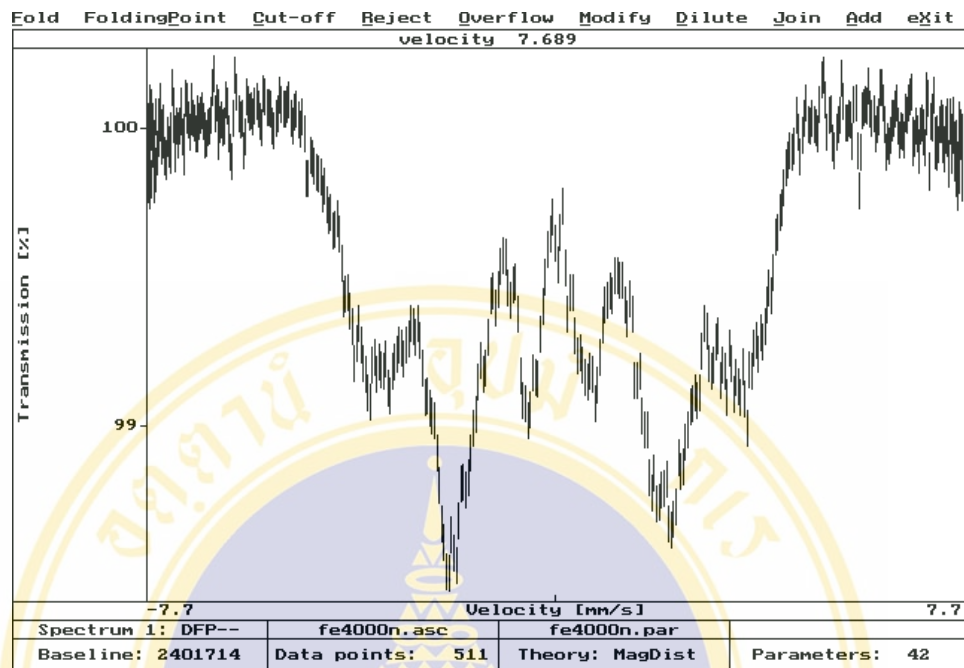


Figure 5.1 (a) Mössbauer spectrum of $\text{Fe}_{40}\text{Ni}_{40}(\text{Si+B})_{19}\text{Mo}_{1-2}$ ribbon before annealing.

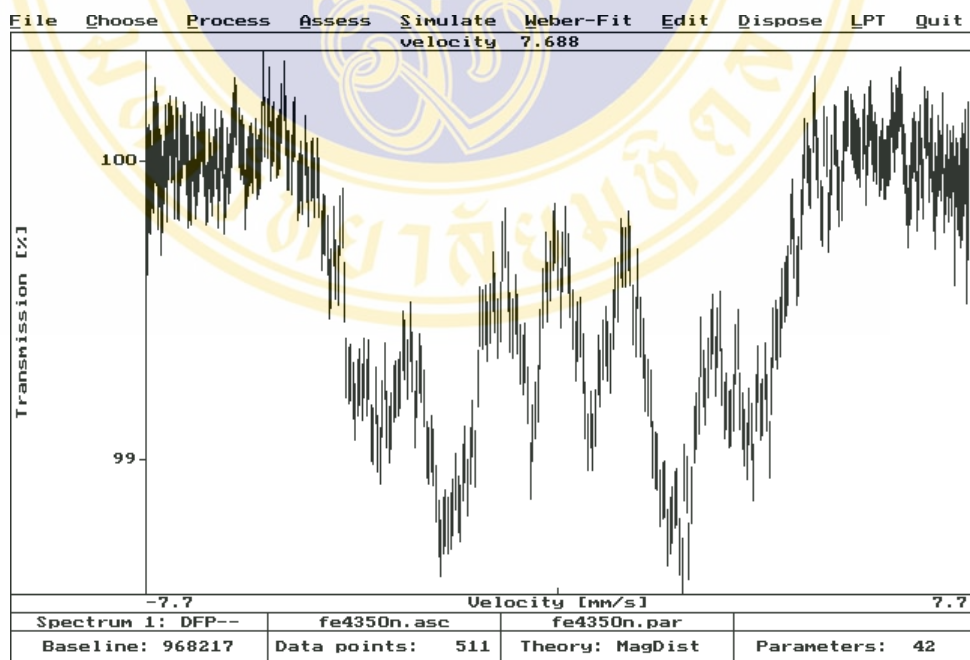


Figure 5.1 (b) Mössbauer spectrum of $\text{Fe}_{40}\text{Ni}_{40}(\text{Si+B})_{19}\text{Mo}_{1-2}$ ribbon after annealing at 350 °C under argon atmosphere.

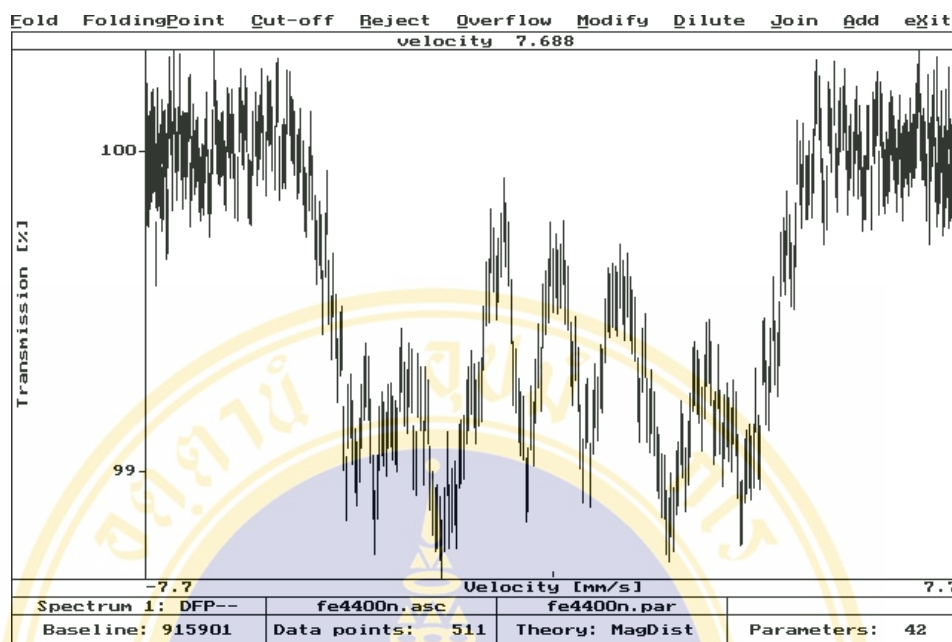


Figure 5.1 (c) Mössbauer spectrum of $\text{Fe}_{40}\text{Ni}_{40}(\text{Si+B})_{19}\text{Mo}_{1-2}$ ribbon after annealing at 400 °C under argon atmosphere.

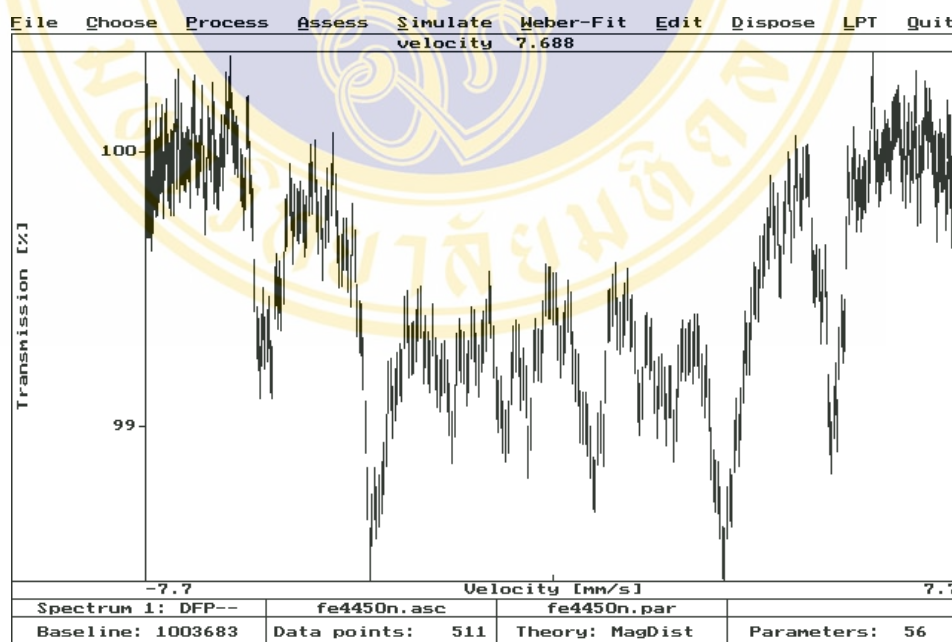


Figure 5.1 (d) Mössbauer spectrum of $\text{Fe}_{40}\text{Ni}_{40}(\text{Si+B})_{19}\text{Mo}_{1-2}$ ribbon after annealing at 450 °C under argon atmosphere.

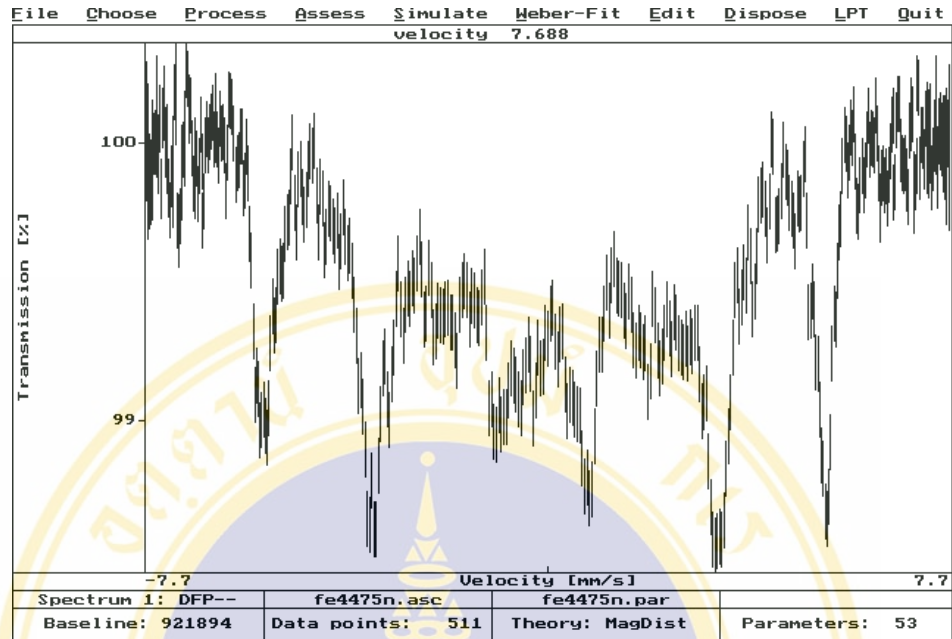


Figure 5.1 (e) Mössbauer spectrum of $\text{Fe}_{40}\text{Ni}_{40}(\text{Si+B})_{19}\text{Mo}_{1-2}$ ribbon after annealing at 475 °C under argon atmosphere.

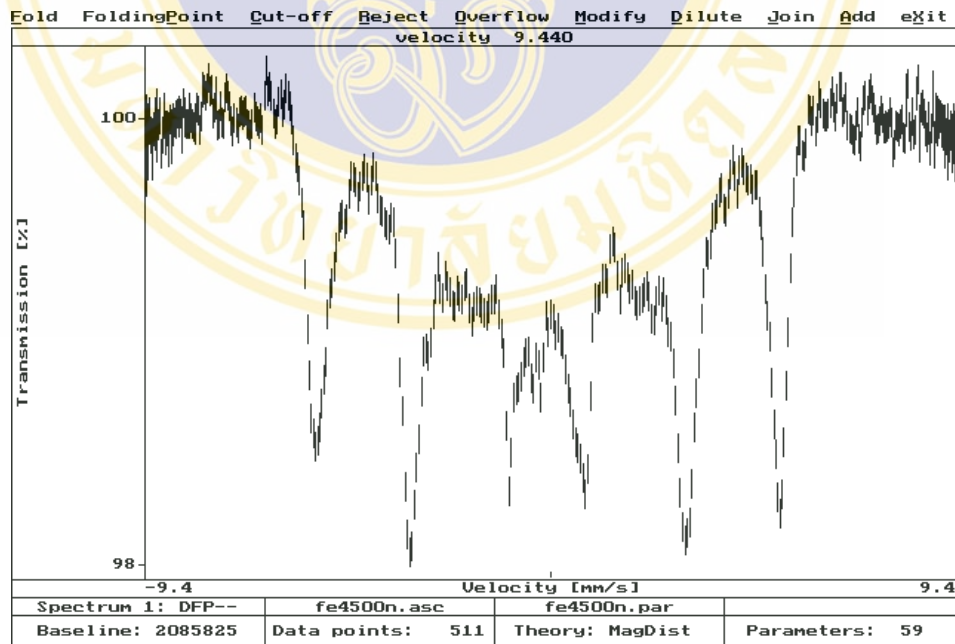


Figure 5.1 (f) Mössbauer spectrum of $\text{Fe}_{40}\text{Ni}_{40}(\text{Si+B})_{19}\text{Mo}_{1-2}$ ribbon after annealing at 500 °C under argon atmosphere.

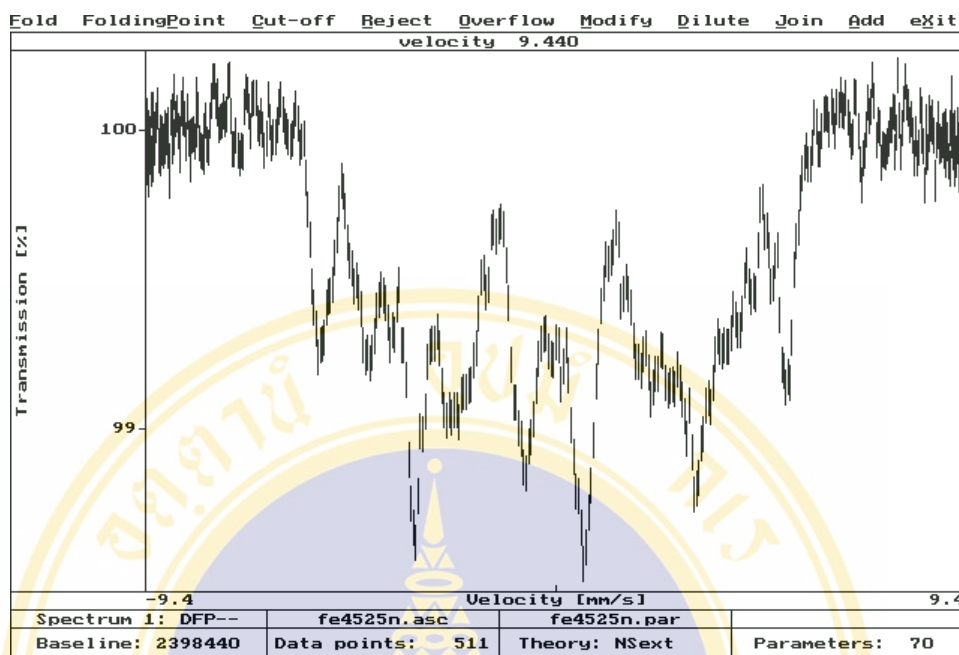


Figure 5.1 (g) Mössbauer spectrum of $\text{Fe}_{40}\text{Ni}_{40}(\text{Si+B})_{19}\text{Mo}_{1-2}$ ribbon after annealing at 525 °C under argon atmosphere.

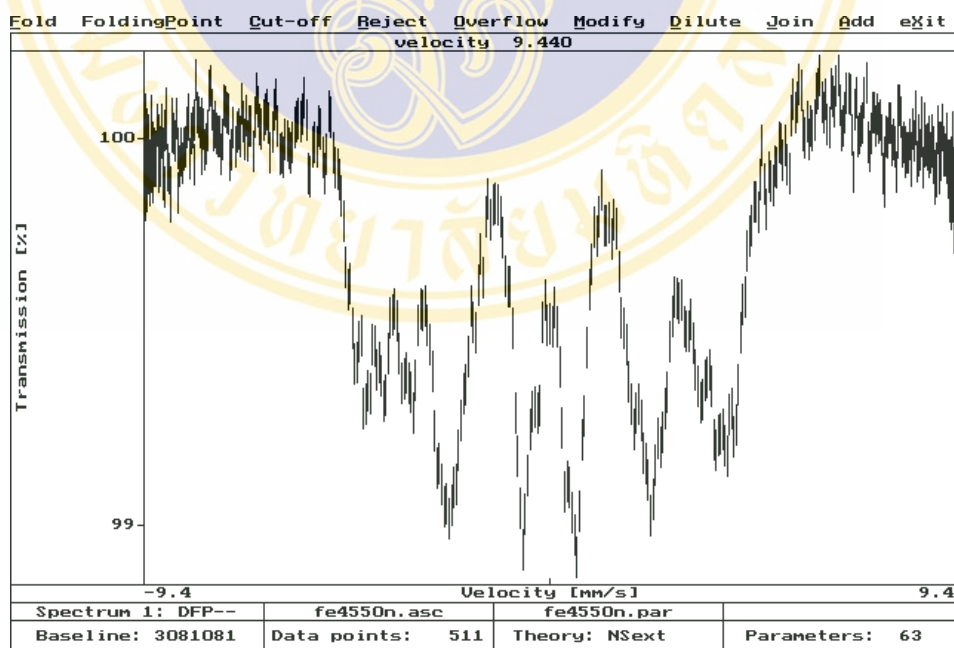


Figure 5.1 (h) Mössbauer spectrum of $\text{Fe}_{40}\text{Ni}_{40}(\text{Si+B})_{19}\text{Mo}_{1-2}$ ribbon after annealing at 550 °C under argon atmosphere.

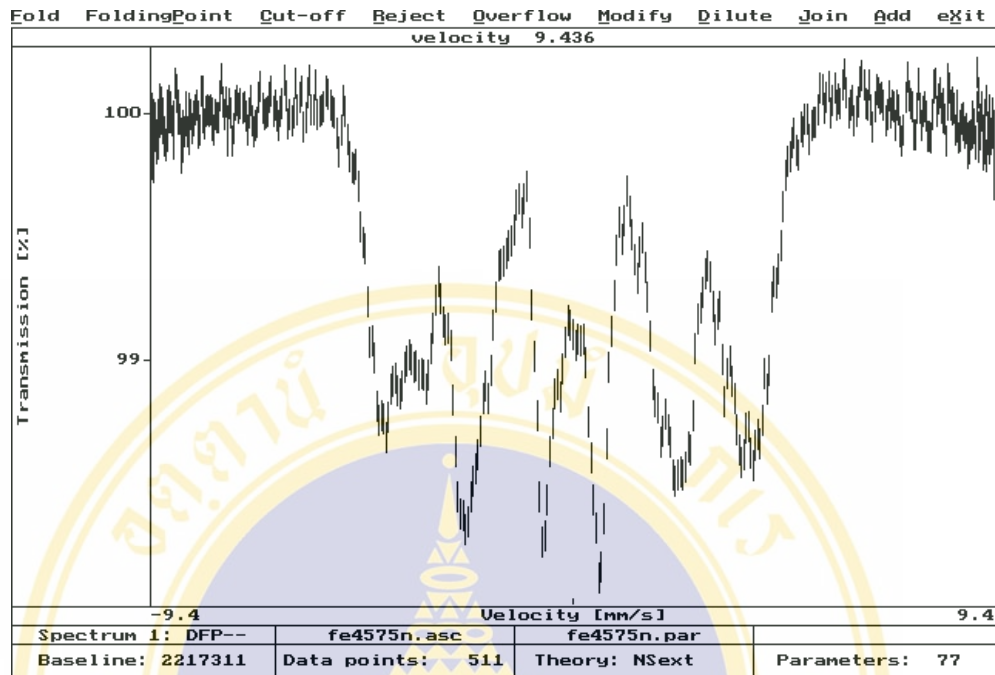


Figure 5.1 (i) Mössbauer spectrum of $\text{Fe}_{40}\text{Ni}_{40}(\text{Si+B})_{19}\text{Mo}_{1-2}$ ribbon after annealing at 575 °C under argon atmosphere.

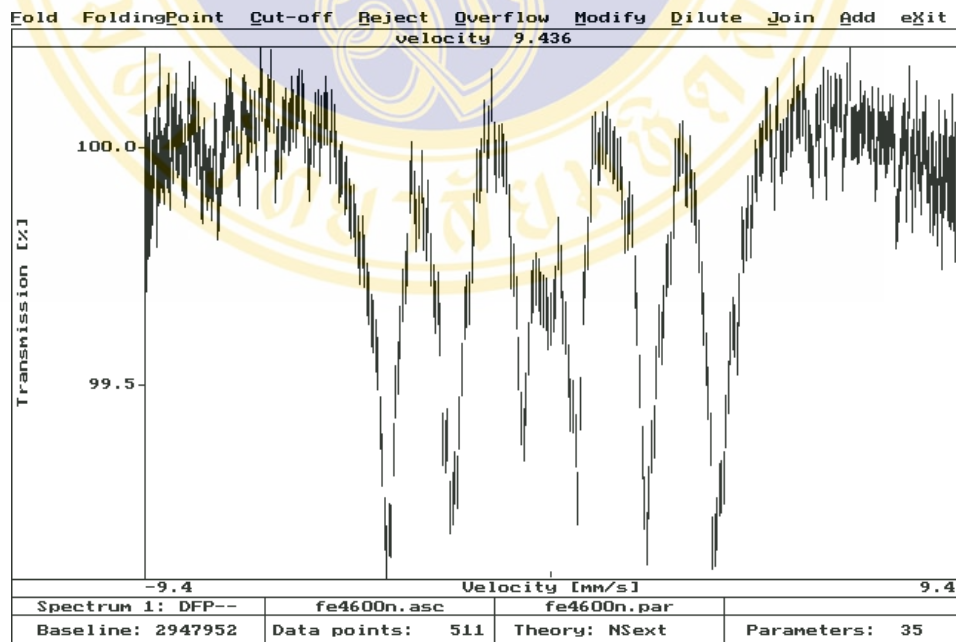


Figure 5.1 (j) Mössbauer spectrum of $\text{Fe}_{40}\text{Ni}_{40}(\text{Si+B})_{19}\text{Mo}_{1-2}$ ribbon after annealing at 600 °C under argon atmosphere.

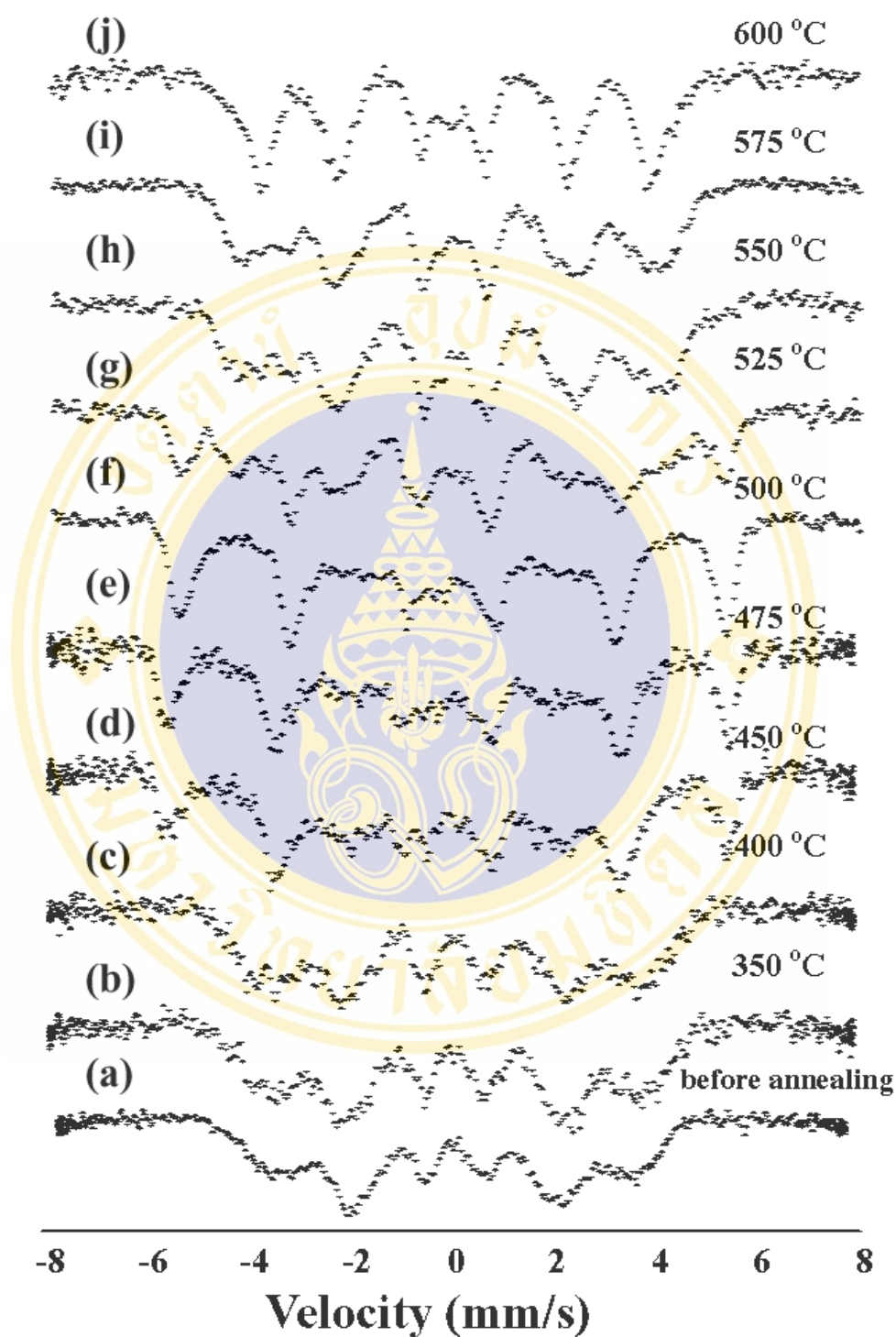


Figure 5.2 Evolution of Mössbauer spectra of annealed $\text{Fe}_{40}\text{Ni}_{40}(\text{Si+B})_{19}\text{Mo}_{1-2}$ ribbons.

Figure 5.2 shows the evolution of Mössbauer spectra of the amorphous ribbons annealed at different temperatures. The spectrum of as-quenched sample showed six broad peaks due to a wide distribution of hyperfine field ^{57}Fe nuclei experienced. After annealing at 350 °C and 400 °C, the spectra similar to as-quenched samples were obtained indicating that the samples annealed still remained in an amorphous phase. However, the ribbon annealed at 450 °C in Figure 5.2 (d) started to show new sharp peaks in addition to the broad peaks. These new features represented new phases of Fe-based magnetic structures while the broadening regions represented the remaining amorphous phase. The results at 475 °C and 500 °C were similar to that ribbon heated at 450 °C that were composed of sharp peaks and broad ones. In Figure 5.2 (g), the intensities of the old sharp peaks decreased as the appearance of new sharp peaks could be observed while broad ones disappeared. The decrease of intensities was caused by transformation of the former Fe-based magnetic structures into new structures. The disappearance of some of sharp peaks or changing in peak intensities could be observed in spectra in Figure 5.2 (h) and (i) respectively. Finally, Figure 5.2 (j), exhibited all new sextets and some quadrupole splittings as the amorphous ribbons completely crystallized.

5.1.2 Least-Squares Fit of Mössbauer Spectra

Figure 5.3 (a)-(p) represent least-squares fitted spectra of $\text{Fe}_{40}\text{Ni}_{40}(\text{Si+B})_{19}\text{Mo}_{1-2}$ ribbon annealing at various temperatures. They could be divided into three groups. The first group consisted of as-quenched [Fig. 5.3 (a)-(b)] and annealed samples at 350 °C [Fig. 5.3 (c)-(d)] and 400 °C [Fig. 5.3 (e)-(f)], all of which still remained in an amorphous phase. The iteration process was achieved by using only MagDist theory in PC-MosII software resulting in a distribution of hyperfine field and other Mössbauer parameters. In the second group, the samples annealed at 450 °C, 475 °C and 500 °C were partially crystallized. They were fitted by MagDist theory and certain numbers of sextets were added to accommodate crystalline phases. Finally, the third group of samples annealed at 525 °C, 550 °C, 575 °C and 600 °C, showed a complete crystallization and NSext theory was needed to do the least squares best fit. All of the subspectra in Figure 5.3 (j) were from the crystalline phases. The increasing of the

number of sextets with the annealed temperature corresponded to the number of ^{57}Fe sites in the crystalline phases.

The Mössbauer spectra of amorphous phase displayed in Figures 5.3 (a), 5.3 (c) and 5.3 (e) were fitted by using Nsing theory corresponding to the least-squares fit of N independent Lorentzian curves. The resulting Mössbauer parameters were listed in table 5.1. Since the annealing temperature was below the crystallization temperature (450 °C) of the ribbon, the effects of thermal treatment only caused the reorientation of the local magnetizations. This could be assessed by the intensity ratio between line 2 and 3, which was related to the direction of the local magnetizations and varied from 0 to 4 following the relation (1)

$$D_{23} = I_{(2,5)}/I_{(3,4)} = 4\sin^2\theta / (1 + \cos^2\theta) \quad (1)$$

Here θ is the angle between the resonant radiation and the average nuclear spin direction. The metallic glasses obtained by rapid quenching under pressure of molten metal alloys would result in the spins of iron nuclei mainly parallel to the surface.

The D_{23} parameter of the as-quenched sample showed the preferred orientation of spins along the ribbon plane. After annealing, the samples increased in randomness of the orientation of the magnetic domain.

Table 5.1 Mössbauer parameters of spectra of amorphous phase taken at room temperature.

Temperature	D_{23}	Isomer shift (mm/s)	Quadrupole Splitting (mm/s)	Average Hyperfine Field (T*)
Before heating	3.87	0.05	-0.02	11.21
350 °C	3.34	0.08	-0.03	11.22
400 °C	2.79	0.06	-0.02	11.25

*T=Tesla

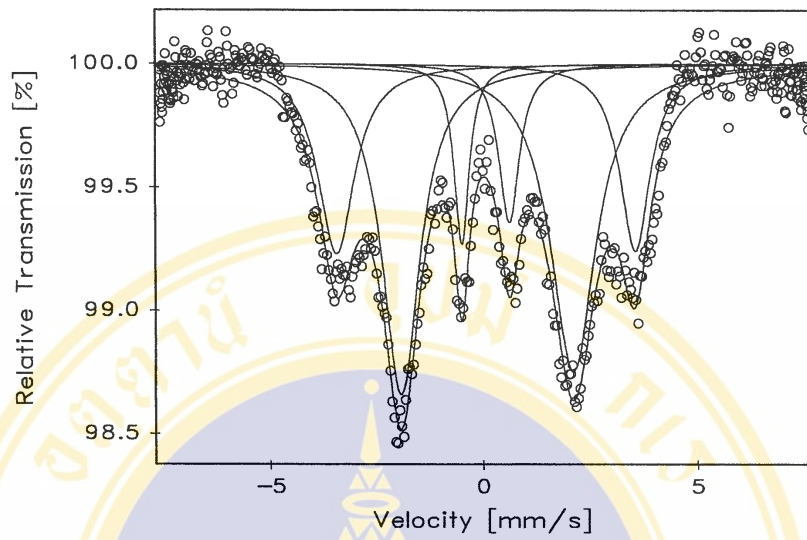


Figure 5.3 (a) Fitted Mössbauer spectrum of $\text{Fe}_{40}\text{Ni}_{40}(\text{Si+B})_{19}\text{Mo}_{1-2}$ ribbon before annealing by Nsing Theory.

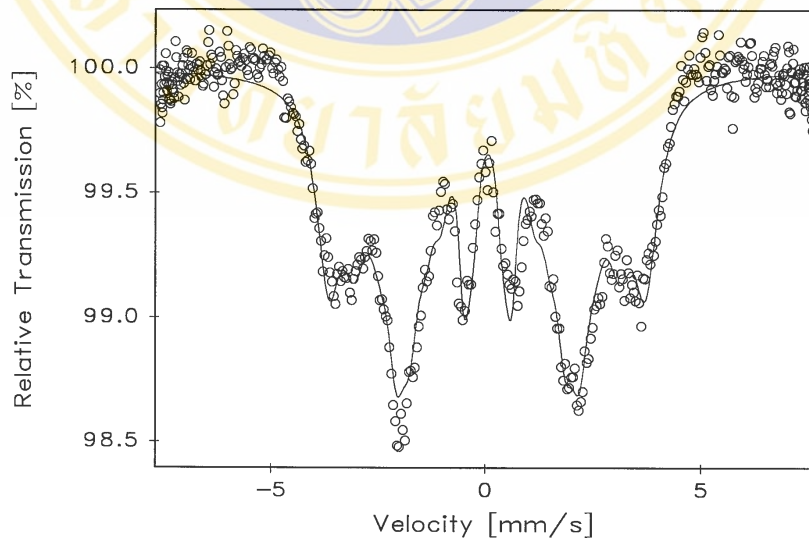


Figure 5.3 (b) Fitted Mössbauer spectrum of $\text{Fe}_{40}\text{Ni}_{40}(\text{Si+B})_{19}\text{Mo}_{1-2}$ ribbon before annealing by MagDist Theory.

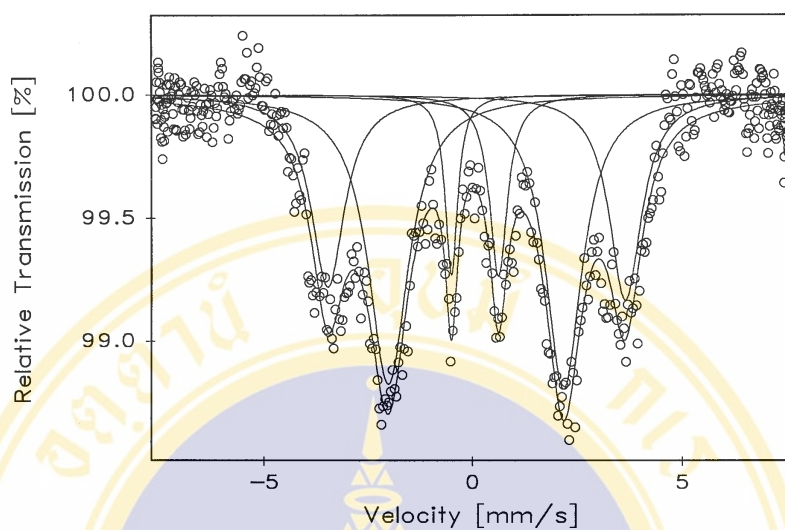


Figure 5.3 (c) Fitted Mössbauer spectrum of $\text{Fe}_{40}\text{Ni}_{40}(\text{Si+B})_{19}\text{Mo}_{1-2}$ after annealing at 350 °C by Nsing Theory.

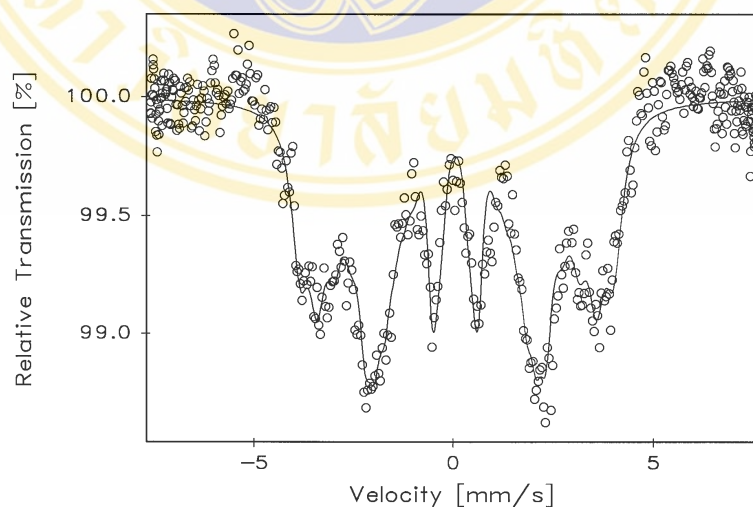


Figure 5.3 (d) Fitted Mössbauer spectrum of $\text{Fe}_{40}\text{Ni}_{40}(\text{Si+B})_{19}\text{Mo}_{1-2}$ ribbon after annealing at 350 °C by MagDist Theory.

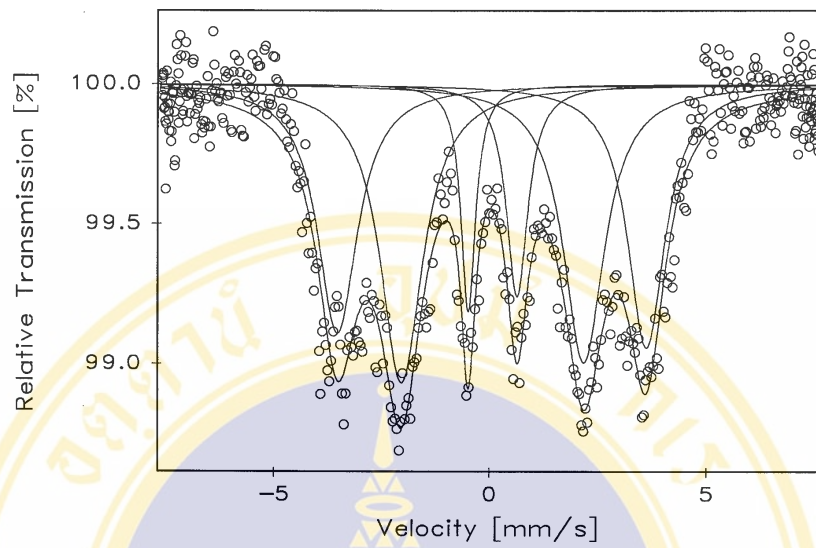


Figure 5.3 (e) Fitted Mössbauer spectrum of $\text{Fe}_{40}\text{Ni}_{40}(\text{Si+B})_{19}\text{Mo}_{1-2}$ after annealing at 400 °C by Nsing Theory.

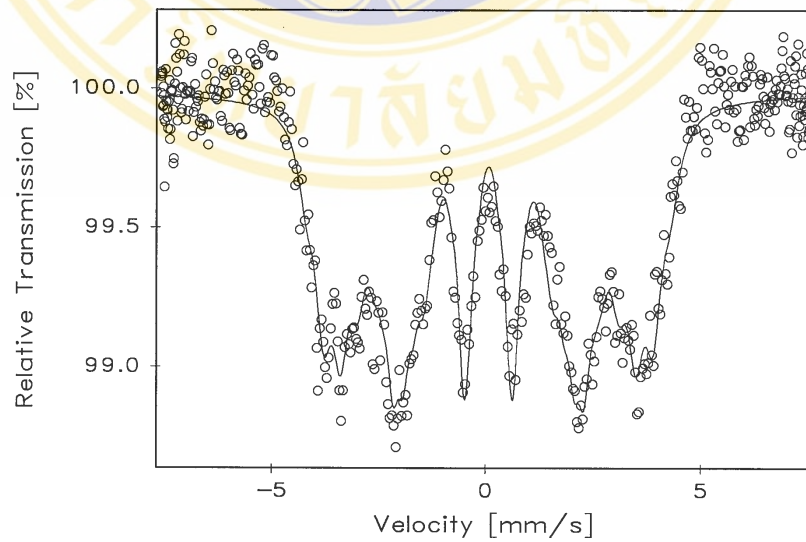


Figure 5.3 (f) Fitted Mössbauer spectrum of $\text{Fe}_{40}\text{Ni}_{40}(\text{Si+B})_{19}\text{Mo}_{1-2}$ ribbon after annealing at 400 °C by MagDist Theory.

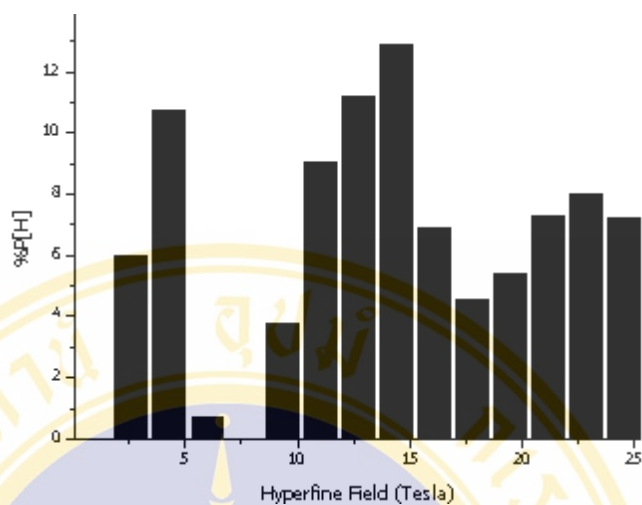


Figure 5.3 (g) Histogram of hyperfine field distribution of amorphous phase of $\text{Fe}_{40}\text{Ni}_{40}(\text{Si+B})_{19}\text{Mo}_{1-2}$ ribbon.

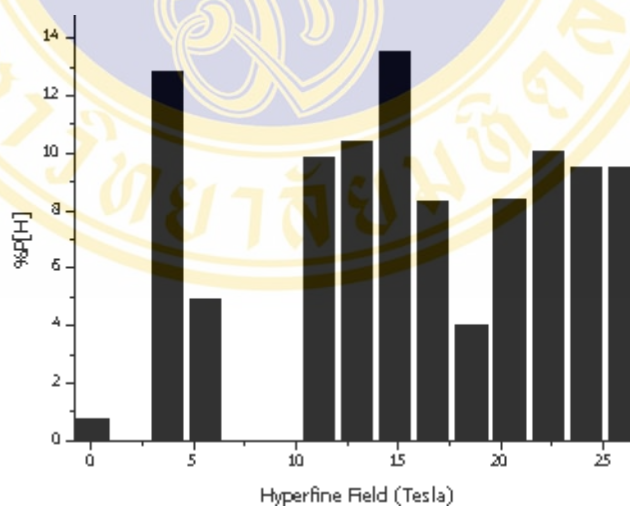


Figure 5.3 (h) Histogram of hyperfine field distribution of amorphous phase of $\text{Fe}_{40}\text{Ni}_{40}(\text{Si+B})_{19}\text{Mo}_{1-2}$ ribbon after annealing at 350 °C.

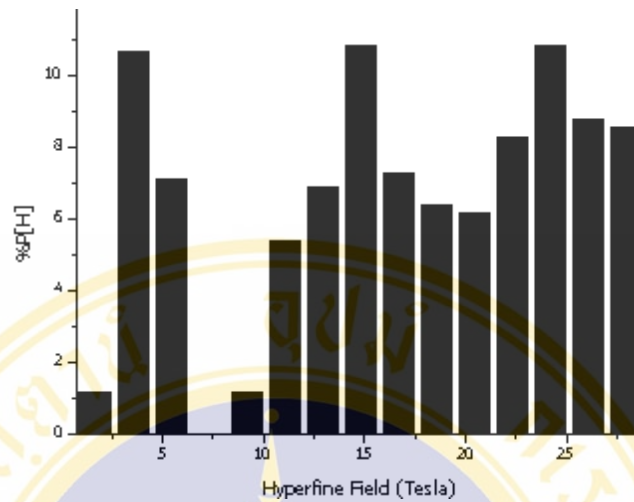


Figure 5.3 (i) Histogram of hyperfine field distribution of amorphous phase of $\text{Fe}_{40}\text{Ni}_{40}(\text{Si+B})_{19}\text{Mo}_{1-2}$ ribbon after annealing at 400 °C.

The histogram of hyperfine field distribution $P(H)$ showed the plots between hyperfine distribution $P(H)$ and the width of hyperfine field distribution (ΔH) in which ^{57}Fe nuclei experienced. The broad distribution of $P(H)$ of amorphous and interface phases were due to randomly located ^{57}Fe nuclei.

Figure 5.3 (g)-(i) show the $P(H)$ distribution of the amorphous phase at each annealing temperature which could suggest changing in environment between iron and its nearest neighbors. As the annealing temperature increased, the width of hyperfine decreased, which could be explained by the fact that decreasing concentration in the disorder matrix. The width of hyperfine field distribution of the interface phase thus decreased as iron atoms orderly increased.

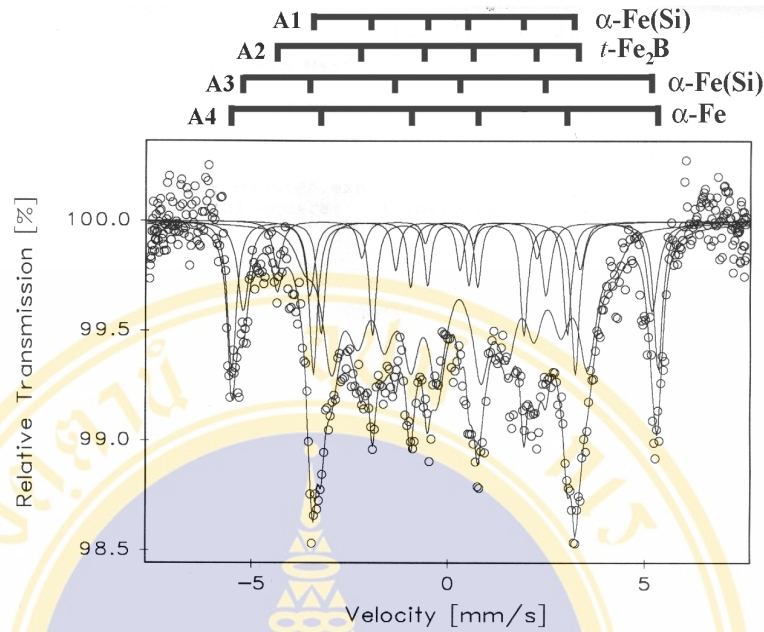


Figure 5.3 (j) Fitted Mössbauer spectrum of $Fe_{40}Ni_{40}(Si+B)_{19}Mo_{1-2}$ ribbon after annealing at 450 °C by MagDist Theory.

Table 5.2 Mössbauer parameters of $Fe_{40}Ni_{40}(Si+B)_{19}Mo_{1-2}$ ribbon after annealing at 450 °C by MagDist Theory.

$H_{Min.}(T)$	$H_{Max.}(T)$	Hyperfine Field (T)	Quadrupole Splitting (mm/s)	Isomer Shift (mm/s)	Width(mm/s)	Relative Area(%)	Assign	Noted
3.43	28.62		0.89	-0.08	0.57	12.71	} Amorphous phase	
						10.15		
						8.76		
						8.33		
						13.66		
		20.67	-0.14	0.05	0.25	13.38	α -Fe(Si)	A1
		23.92	-0.56	-0.14	0.28	4.80	t -Fe ₂ B	A2
		32.23	0.47	-0.17	0.35	11.27	α -Fe(Si)	A3
		33.59	-0.02	0.00	0.27	14.20	α -Fe	A4

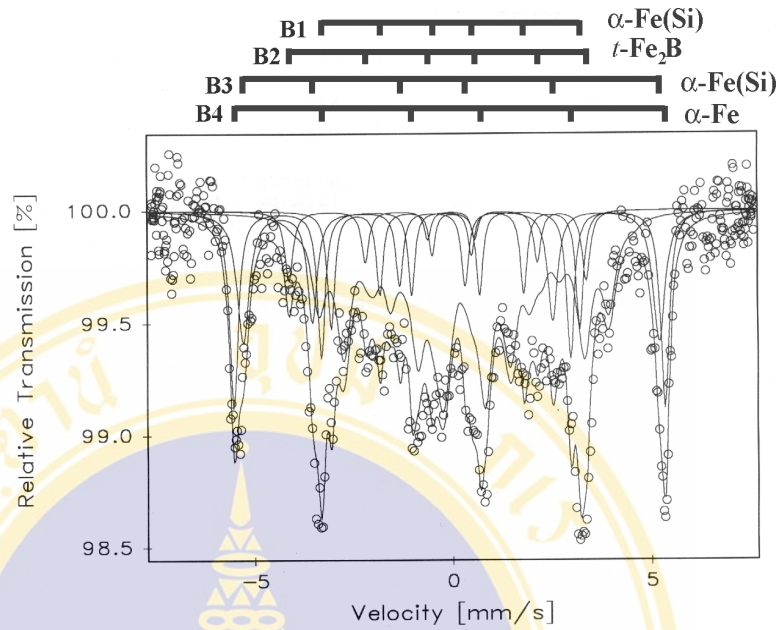


Figure 5.3 (k) Fitted Mössbauer spectrum of $\text{Fe}_{40}\text{Ni}_{40}(\text{Si}+\text{B})_{19}\text{Mo}_{1-2}$ ribbon after annealing at $475\text{ }^{\circ}\text{C}$ by MagDist Theory.

Table 5.3 Mössbauer parameters of $\text{Fe}_{40}\text{Ni}_{40}(\text{Si}+\text{B})_{19}\text{Mo}_{1-2}$ ribbon after annealing at $475\text{ }^{\circ}\text{C}$ by MagDist Theory.

$H_{\text{Min.}}(\text{T})$	$H_{\text{Max.}}(\text{T})$	Hyperfine Field (T)	Quadrupole Splitting (mm/s)	Isomer Shift (mm/s)	Width(mm/s)	Relative Area(%)	Assign	Noted
3.36	26.55		0.08	0.32	0.44	11.71	Amorphous phase	
						10.76		
						2.93		
						3.42		
						12.24		
						8.10		
		19.50	0.06	0.41	0.25	9.84	$\alpha\text{-Fe}(\text{Si})$	B1
		23.49	-0.42	-0.13	0.25	5.89	$t\text{-Fe/B}$	B2
		32.51	0.43	-0.18	0.37	16.73	$\alpha\text{-Fe}(\text{Si})$	B3
		33.68	0.05	-0.03	0.26	17.73	$\alpha\text{-Fe}$	B4

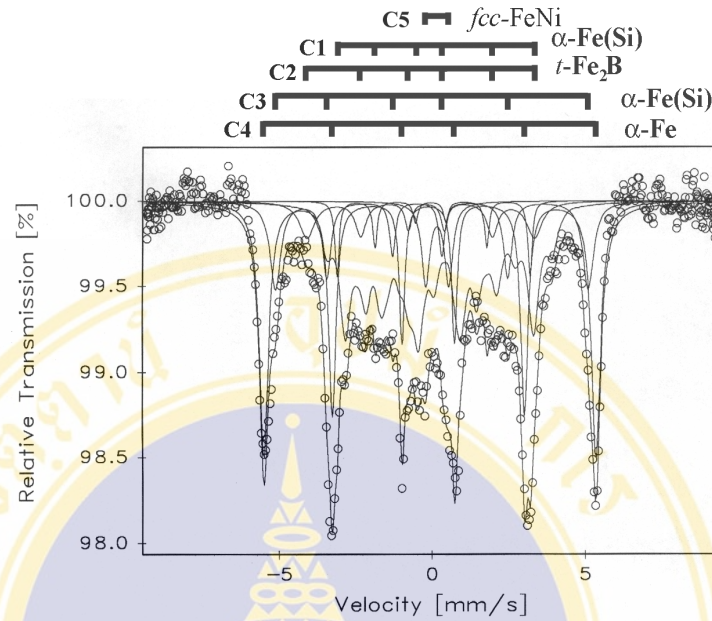


Figure 5.3 (I) Fitted Mössbauer spectrum of $Fe_{40}Ni_{40}(Si+B)_{19}Mo_{1-2}$ ribbon after annealing at 500 °C by MagDist Theory.

Table 5.4 Mössbauer parameters of $Fe_{40}Ni_{40}(Si+B)_{19}Mo_{1-2}$ ribbon after annealing at 500 °C by MagDist Theory.

$H_{Min.}(T)$	$H_{Max.}(T)$	Hyperfine Field (T)	Quadrupole Splitting (mm/s)	Isomer Shift (mm/s)	Width(mm/s)	Relative Area(%)	Assign	Noted
4.22	26.51		0.56	-0.51	0.44	9.95	} Amorphous phase	
						3.37		
						7.16		
						3.83		
						12.18		
						4.04		
		19.56	0.06	-0.07	0.16	4.11	α -Fe(Si)	C1
		23.04	-0.21	-0.35	0.59	7.40	t -Fe ₂ B	C2
		31.67	0.45	-0.32	0.42	12.68	α -Fe(Si)	C3
		33.64	0.03	-0.17	0.35	30.96	α -Fe	C4
			0.73	0.10	0.32	4.55	fcc -FeNi	C5

The Mössbauer spectra were fitted successfully for the samples annealing at temperatures 450 °C, 475 °C and 500 °C and their relative areas could be obtained. The area of the amorphous phase was reduced with temperature increased. Tables 5.5 showed areas changing from 56.35 % at 450 °C, 49.81 % at 475 °C to 40.30 % at 500 °C respectively. Figure 5.3 (j) displays the Mössbauer spectrum of the sample annealing at 450 °C, showing the subspectra of crystalline and amorphous phases. The crystalline phases could be analyzed as listed in Table 5.2 as α -Fe(A4), t -Fe₂B(A2) and α -Fe(Si)(A1 and A3) respectively. These crystalline phases could still be observed when the annealing temperature was raised to 475 °C and 500 °C as shown in Table 5.3 and 5.4. A new paramagnetic phase appeared when annealed at 500 °C, which was assigned as fcc -FeNi^[76]. The subspectra of α -Fe(Si) was decomposed to two subspectra, and each spectra corresponded to difference number of nearest neighbors of Fe atom. The subspectra A1, B1 and C1 were α -Fe(Si) which composed of four neighbors of Fe atom while subspectra A3, B3 and C3 had been assigned to eight neighbors of Fe atom. The crystallization process could be described as followed:

At 450 °C and 475 °C

Amorphous -----> amorphous + α -Fe + α -Fe(Si) + t -Fe₂B

At 500 °C

Amorphous -----> amorphous + α -Fe + α -Fe(Si) + t -Fe₂B + fcc -FeNi

Table 5.5 Areas of amorphous phase with increasing annealing temperature.

Samples	Area of amorphous phase(%)
450 °C	56.35
475 °C	49.81
500 °C	40.30

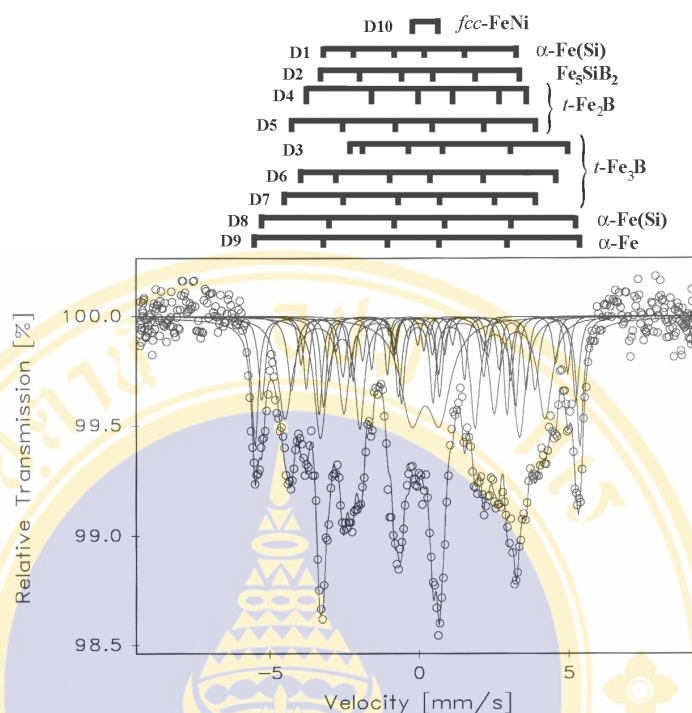


Figure 5.3 (m) Fitted Mössbauer spectrum of $\text{Fe}_{40}\text{Ni}_{40}(\text{Si+B})_{19}\text{Mo}_{1-2}$ ribbon after annealing at 525 °C by NSept Theory.

Table 5.6 Mössbauer parameters of $\text{Fe}_{40}\text{Ni}_{40}(\text{Si+B})_{19}\text{Mo}_{1-2}$ ribbon after annealing at 525 °C by NSept Theory.

Hyperfine Field (T)	Quadrupole Splitting (mm/s)	Isomer Shift (mm/s)	Width(mm/s)	Relative Area(%)	Assign	Noted
19.95	0.34	-0.25	0.22	6.51	α -Fe(Si)	D1
20.64	0.06	-0.10	0.49	19.57	Fe_5SiB_2	D2
22.53	1.09	0.69	0.21	4.15	t - Fe_3B	D3
22.81	-0.66	0.14	0.23	5.56	t - Fe_2B	D4
25.25	-0.02	-0.28	0.32	7.94	t - Fe_2B	D5
26.40	0.60	-0.09	0.22	3.60	t - Fe_3B	D6
26.97	-0.16	-0.15	0.58	19.47	t - Fe_3B	D7
32.53	-0.06	-0.07	0.27	7.64	α -Fe(Si)	D8
33.65	0.12	-0.21	0.27	11.61	α -Fe	D8
	0.92	0.13	0.91	13.96	fcc -FeNi	D10

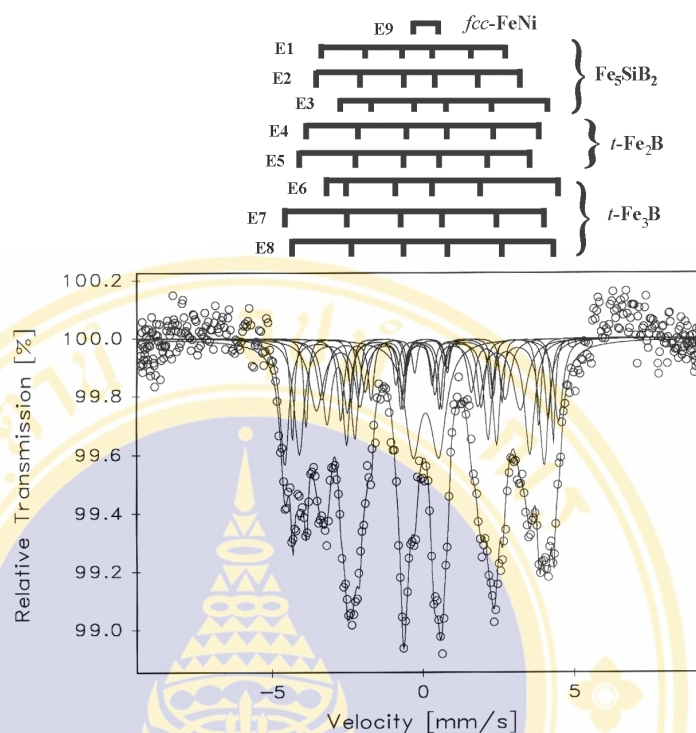


Figure 5.3 (n) Fitted Mössbauer spectrum of $\text{Fe}_{40}\text{Ni}_{40}(\text{Si+B})_{19}\text{Mo}_{1-2}$ ribbon after annealing at $550\text{ }^{\circ}\text{C}$ by NSext Theory.

Table 5.7 Mössbauer parameters of $\text{Fe}_{40}\text{Ni}_{40}(\text{Si+B})_{19}\text{Mo}_{1-2}$ ribbon after annealing at $550\text{ }^{\circ}\text{C}$ by NSext Theory.

Hyperfine Field (T)	Quadrupole Splitting (mm/s)	Isomer Shift (mm/s)	Width(mm/s)	Relative Area(%)	Assign	Noted
18.83	-0.18	-0.30	0.41	9.12	Fe_5SiB_2	E1
20.92	-0.04	-0.21	0.56	14.67	Fe_5SiB_2	E2
21.27	0.42	0.42	0.25	7.51	Fe_5SiB_2	E3
23.87	-0.15	-0.02	0.17	5.60	$t\text{-Fe}_3\text{B}$	E4
23.63	-0.25	-0.24	0.40	16.91	$t\text{-Fe}_2\text{B}$	E5
23.73	0.92	0.12	0.36	11.02	$t\text{-Fe}_2\text{B}$	E6
26.61	-0.26	-0.24	0.36	16.67	$t\text{-Fe}_3\text{B}$	E7
26.75	-0.15	-0.01	0.16	6.24	$t\text{-Fe}_3\text{B}$	E8
	0.83	0.03	0.63	12.27	fcc-FeNi	E9

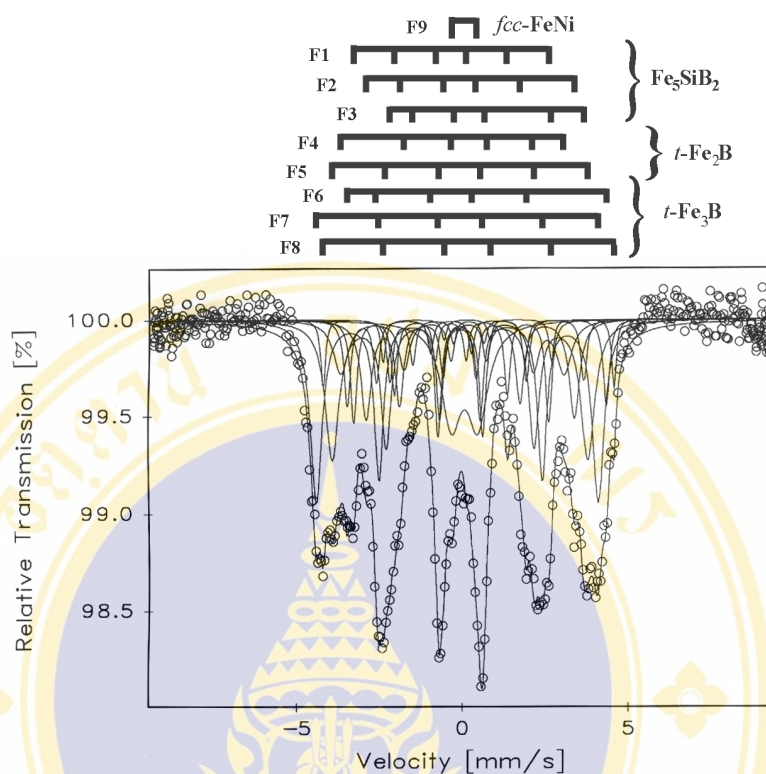


Figure 5.3 (o) Fitted Mössbauer spectrum of $\text{Fe}_{40}\text{Ni}_{40}(\text{Si+B})_{19}\text{Mo}_{1-2}$ ribbon after annealing at $575\text{ }^\circ\text{C}$ by N Sext Theory.

Table 5.8 Mössbauer parameters of $\text{Fe}_{40}\text{Ni}_{40}(\text{Si+B})_{19}\text{Mo}_{1-2}$ ribbon after annealing at $575\text{ }^\circ\text{C}$ by N Sext Theory.

Hyperfine Field (T)	Quadrupole Splitting (mm/s)	Isomer Shift (mm/s)	Width(mm/s)	Relative Area(%)	Assign	Noted
18.26	-0.01	-0.40	0.23	7.46	Fe_5SiB_2	F1
19.48	0.29	0.02	0.38	11.70	Fe_5SiB_2	F2
18.12	0.52	0.41	0.22	4.31	Fe_5SiB_2	F3
20.90	-0.52	-0.12	0.54	9.11	$t\text{-Fe}_2\text{B}$	F4
23.93	-0.03	-0.14	0.50	21.89	$t\text{-Fe}_2\text{B}$	F5
24.23	0.74	-0.01	0.23	6.24	$t\text{-Fe}_3\text{B}$	F6
26.41	-0.13	-0.17	0.43	24.41	$t\text{-Fe}_3\text{B}$	F7
27.20	0.01	0.10	0.16	3.51	$t\text{-Fe}_3\text{B}$	F8
	0.78	0.01	0.74	11.37	fcc-FeNi	F9

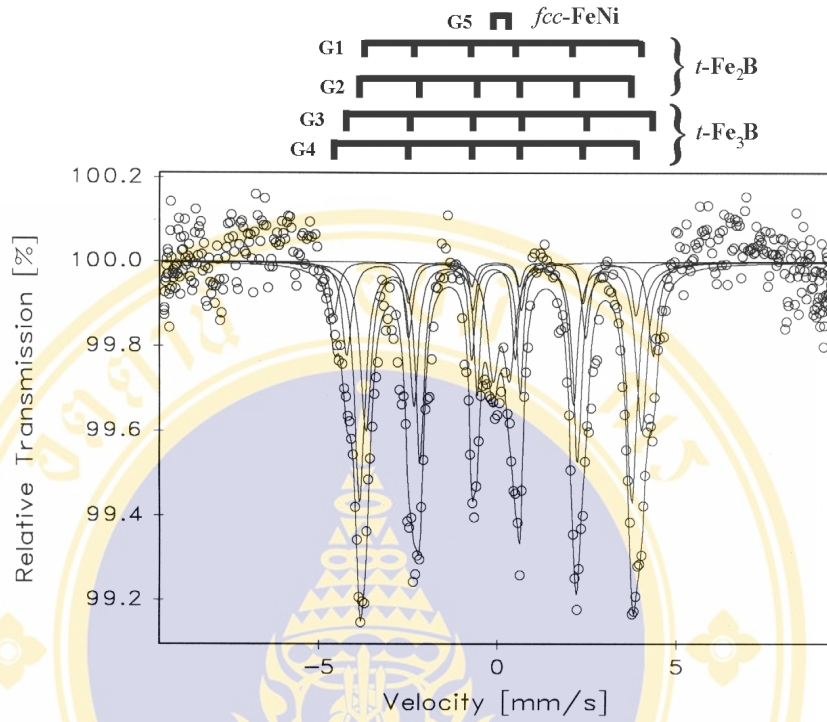


Figure 5.3 (p) Fitted Mössbauer spectrum of $\text{Fe}_{40}\text{Ni}_{40}(\text{Si+B})_{19}\text{Mo}_{1-2}$ ribbon after annealing at $600\text{ }^{\circ}\text{C}$ by N Sext Theory.

Table 5.9 Mössbauer parameters of $\text{Fe}_{40}\text{Ni}_{40}(\text{Si+B})_{19}\text{Mo}_{1-2}$ ribbon after annealing at $600\text{ }^{\circ}\text{C}$ by N Sext Theory.

Hyperfine Field (T)	Quadrupole Splitting (mm/s)	Isomer Shift (mm/s)	Width(mm/s)	Relative Area(%)	Assign	Noted
23.93	0.26	0.12	0.37	29.62	$t\text{-Fe}_2\text{B}$	G1
23.65	-0.10	0.09	0.35	39.43	$t\text{-Fe}_2\text{B}$	G2
26.61	0.06	0.12	0.32	14.37	$t\text{-Fe}_3\text{B}$	G3
26.21	-0.32	-0.11	0.28	7.13	$t\text{-Fe}_3\text{B}$	G4
	0.44	0.22	0.38	9.46	$fcc\text{-FeNi}$	G5

Table 5.10 Percent area of crystalline phases at various annealing temperatures.

Annealing Temperature	Area(%)					
	α -Fe	α -Fe(Si)	<i>t</i> -Fe ₂ B	<i>t</i> -Fe ₃ B	<i>t</i> -Fe ₅ SiB ₂	<i>fcc</i> -FeNi
As-quenched	0	0	0	0	0	0
350	0	0	0	0	0	0
400	0	0	0	0	0	0
450	14.20	24.65	4.80	0	0	0
475	17.73	26.57	5.89	0	0	0
500	30.96	16.79	7.40	0	0	4.55
525	11.61	14.15	13.50	27.22	19.57	13.96
550	0	0	22.51	33.92	31.30	12.27
575	0	0	31.00	34.16	23.47	11.37
600	0	0	69.04	21.50	0	9.46

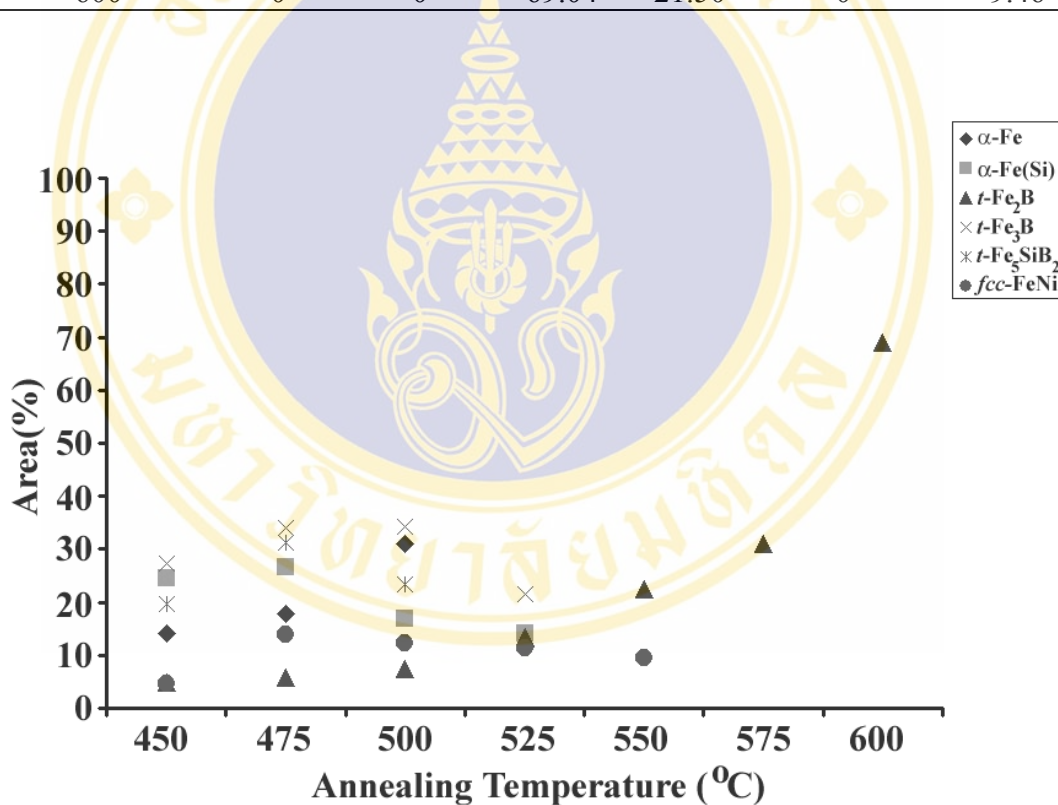


Figure 5.4 Percent area of crystallized phases determined by fitting Mössbauer spectra

existence of ten sites (D1-D10) of ^{57}Fe described by hyperfine field, isomer shift and quadrupole splitting. It can be concluded that subspectra D1 and D8 correspond to $\alpha\text{-Fe}(\text{Si})$ phases, while D9 belongs to $\alpha\text{-Fe}$ phase respectively. D3, D6 and D7 can be assigned $t\text{-Fe}_3\text{B}$ while D4 and D5 belong to $t\text{-Fe}_2\text{B}$ and the D10 belongs to $fcc\text{-FeNi}$ structure.

The fitted subspectra of crystallized phases (E1 to E9) of annealed sample at 550 °C were shown in Table 5.7. The E1 to E3 subspectra belong to $t\text{-Fe}_5\text{SiB}_2$, while E6 to E8 arise from the $t\text{-Fe}_3\text{B}$ phase. The E4 and E5 sites correspond to $t\text{-Fe}_2\text{B}$ whereas E9 is assigned as $fcc\text{-FeNi}$. The $\alpha\text{-Fe}$ and $\alpha\text{-Fe}(\text{Si})$ phases could not be observed at this annealing temperature.

The fitted Mössbauer results of the annealed sample at 575 °C were shown in Table 5.8, which composed of nine subspectra (F1 to F9). The assignment of subspectra is similar to those at 550 °C (as shown in Table 5.7) but different in relative areas. The F1 to F3 subspectra correspond to $t\text{-Fe}_5\text{SiB}_2$, while F6 to F8 arise from $t\text{-Fe}_3\text{B}$. The F4 and F5 subspectra are assigned to $t\text{-Fe}_2\text{B}$ and E9 belongs to the $fcc\text{-FeNi}$ phase.

The fitted Mössbauer parameters of the completely crystallized sample at 600 °C were shown in Table 5.9. The $t\text{-Fe}_5\text{SiB}_2$ phases disappeared while $t\text{-Fe}_2\text{B}$ (G1 and G2), $t\text{-Fe}_3\text{B}$ (G3 and G4) and $fcc\text{-FeNi}$ (G5) were still observed at this annealing temperature.

5.2 Scanning Electron Microscope

Figures 5.4 (a) – (f) show grain sizes of $\text{Fe}_{40}\text{Ni}_{40}(\text{Si}+\text{B})_{19}\text{Mo}_{1-2}$ amorphous ribbon after annealed at different temperatures. The appearance of larger grain sizes in samples annealed at higher temperatures supported the fact that the crystallization was at the expense of the amorphous phase.

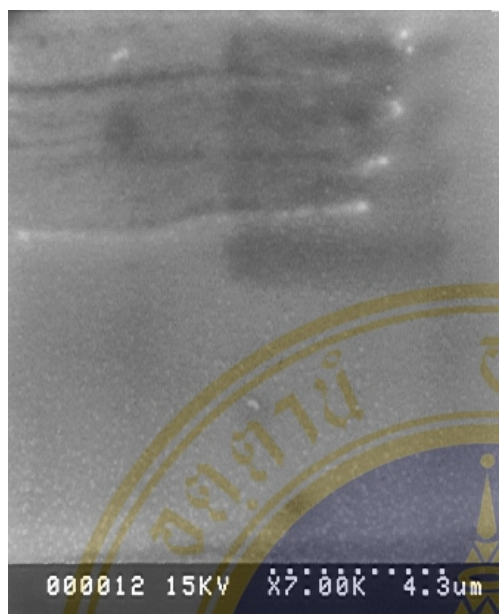


Figure 5.5 (a) As-quenched of $\text{Fe}_{40}\text{Ni}_{40}$ $(\text{Si+B})_{19}\text{Mo}_{1-2}$ ribbon.

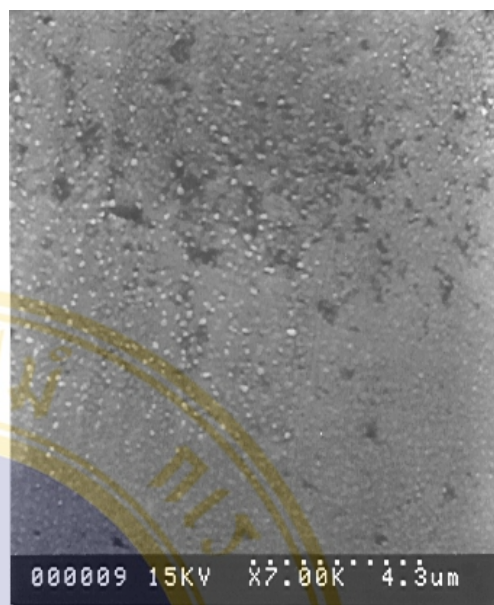


Figure 5.5 (b) $\text{Fe}_{40}\text{Ni}_{40}(\text{Si+B})_{19}\text{Mo}_{1-2}$ ribbon annealed at 500 °C.

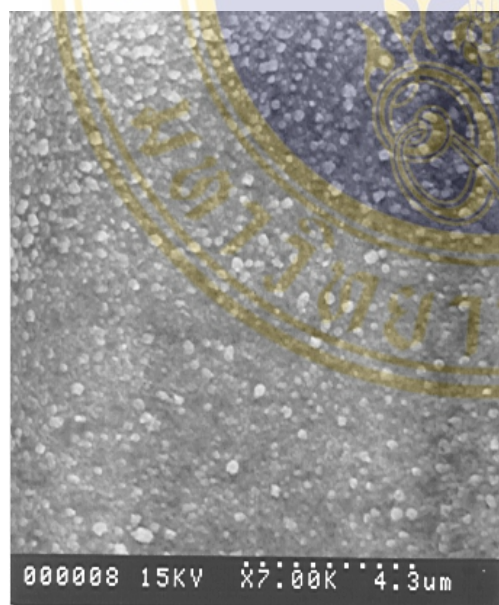


Figure 5.5 (c) $\text{Fe}_{40}\text{Ni}_{40}(\text{Si+B})_{19}\text{Mo}_{1-2}$ ribbon annealed at 525 °C.

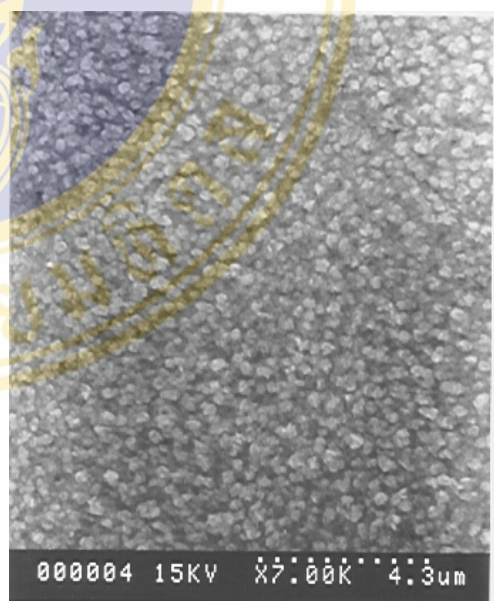


Figure 5.5 (d) $\text{Fe}_{40}\text{Ni}_{40}(\text{Si+B})_{19}\text{Mo}_{1-2}$ ribbon annealed at 550 °C.

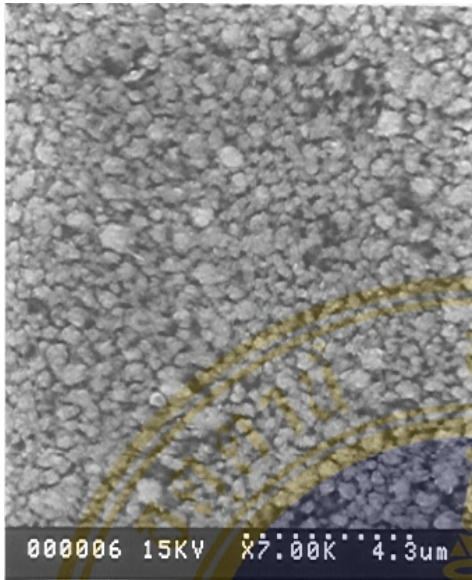


Figure 5.5 (e) $\text{Fe}_{40}\text{Ni}_{40}(\text{Si+B})_{19}\text{Mo}_{1-2}$ ribbon annealed at 575 °C.

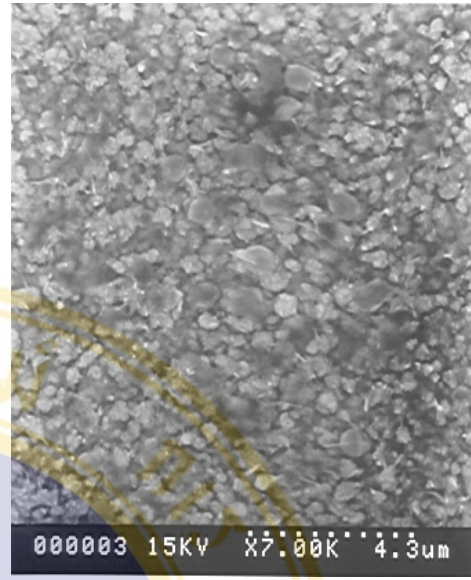
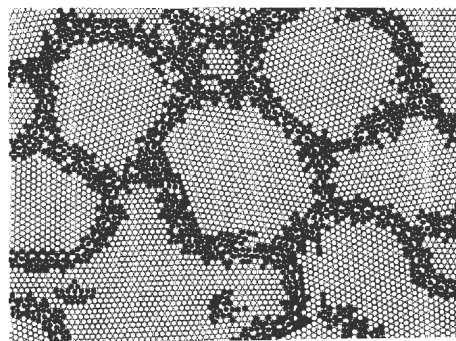


Figure 5.5 (f) $\text{Fe}_{40}\text{Ni}_{40}(\text{Si+B})_{19}\text{Mo}_{1-2}$ ribbon annealed at 600 °C.

Figure 5.5 (b) shows SEM image of $\text{Fe}_{40}\text{Ni}_{40}(\text{Si+B})_{19}\text{Mo}_{1-2}$ amorphous ribbon which partially crystallized. These SEM images displayed crystalline particles that were embedded in amorphous matrix. Figures 5.5 (c) to (f) show completely crystallization samples. The SEM images exhibited larger grain boundaries of crystalline particles, as annealing temperature was raised. The schematic diagram of grains and their grain boundaries were given in figure 5.6.



Figures 5.6 Schematic diagram of grain boundary of nanoparticles.

5.3 Atomic Force Microscopy

5.3.1 Surface roughness parameters

Surface topographical data can be obtained in one or two dimensions, i.e. $z(x)$ or $z(x, y)$. The data can be processed and then the following surface roughness parameters obtained, that is average surface roughness (R_a) and root-mean-square surface roughness (R_q).

Average surface roughness (R_a), the most frequently used roughness parameter is average surface roughness. It is expressed as

$$R_a = \frac{1}{n} \sum_{i=1}^n |z_i| \quad (2)$$

where z_i is the height or depth of the i th highest or lowest deviation and n is the number of discrete profile deviations.

Root-mean-square surface roughness (R_q), R_q is defined as the root-mean-square of the deviations in height from the profile mean and it is

$$R_q = \sqrt{\frac{1}{n} \sum_{i=1}^n z_i^2} \quad (3)$$

Roughness R_a and R_q are often used as quantitative parameters. However, they cannot describe irregularity or complexity of surface.

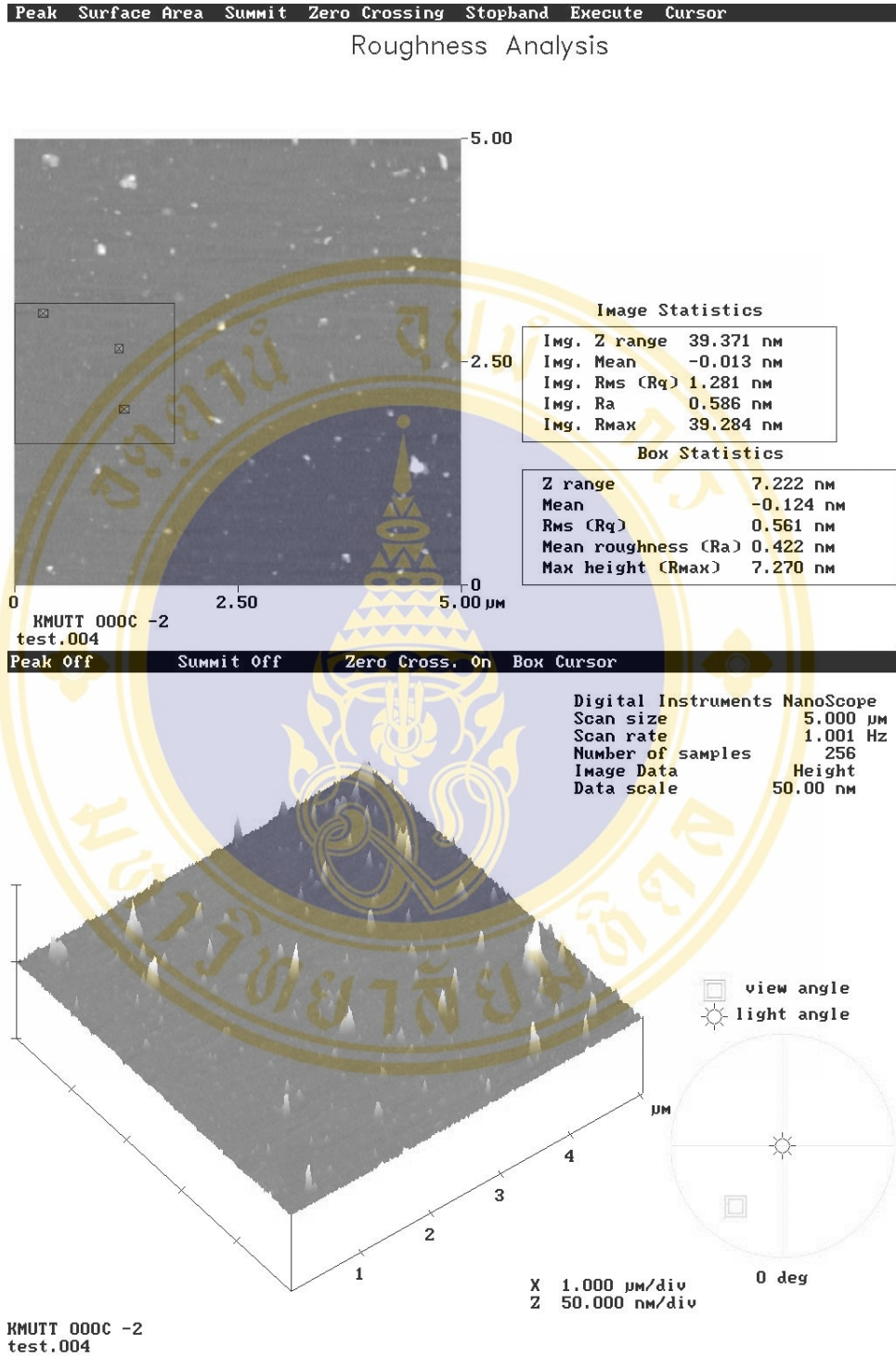


Figure 5.7 (a) Tapping mode image of AFM scan of as-quenched sample.

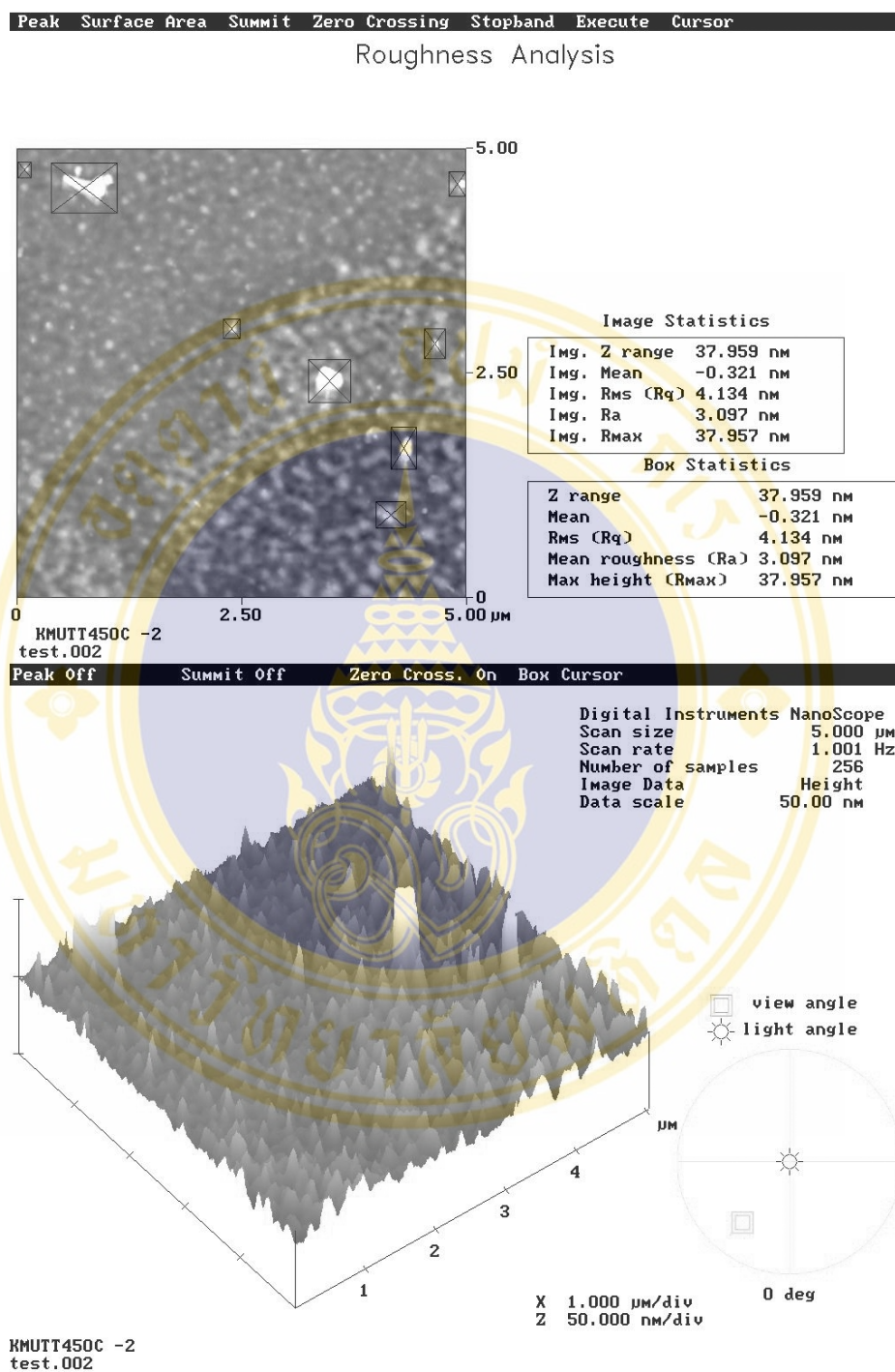


Figure 5.7 (b) Tapping mode image of AFM scan of $\text{Fe}_{40}\text{Ni}_{40}(\text{Si+B})_{19}\text{Mo}_{1-2}$ ribbon after annealing at 450 °C.

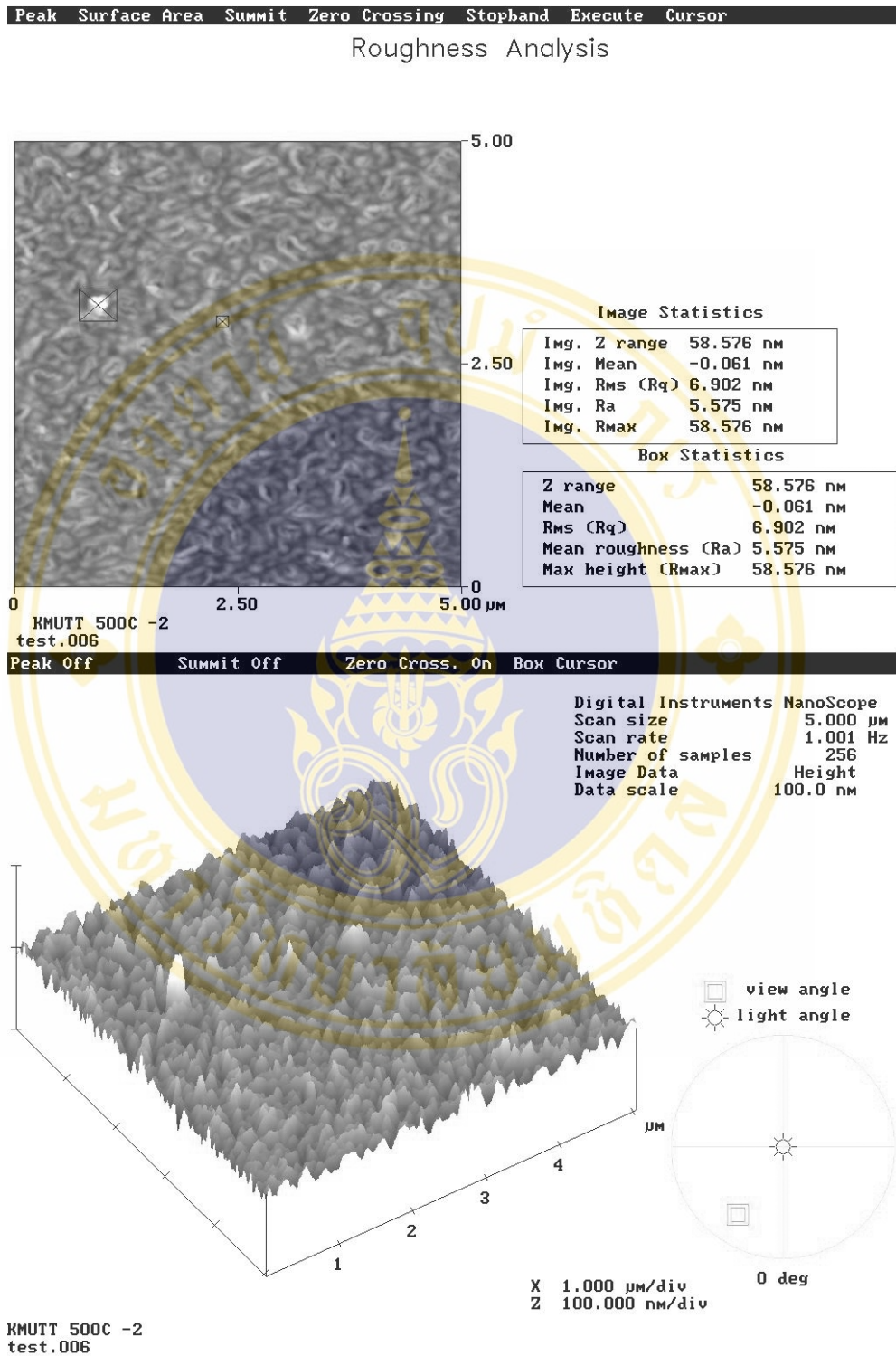


Figure 5.7 (c) Tapping mode image of AFM scan of $\text{Fe}_{40}\text{Ni}_{40}(\text{Si}+\text{B})_{19}\text{Mo}_{1-2}$ ribbon after annealing at 500 °C.

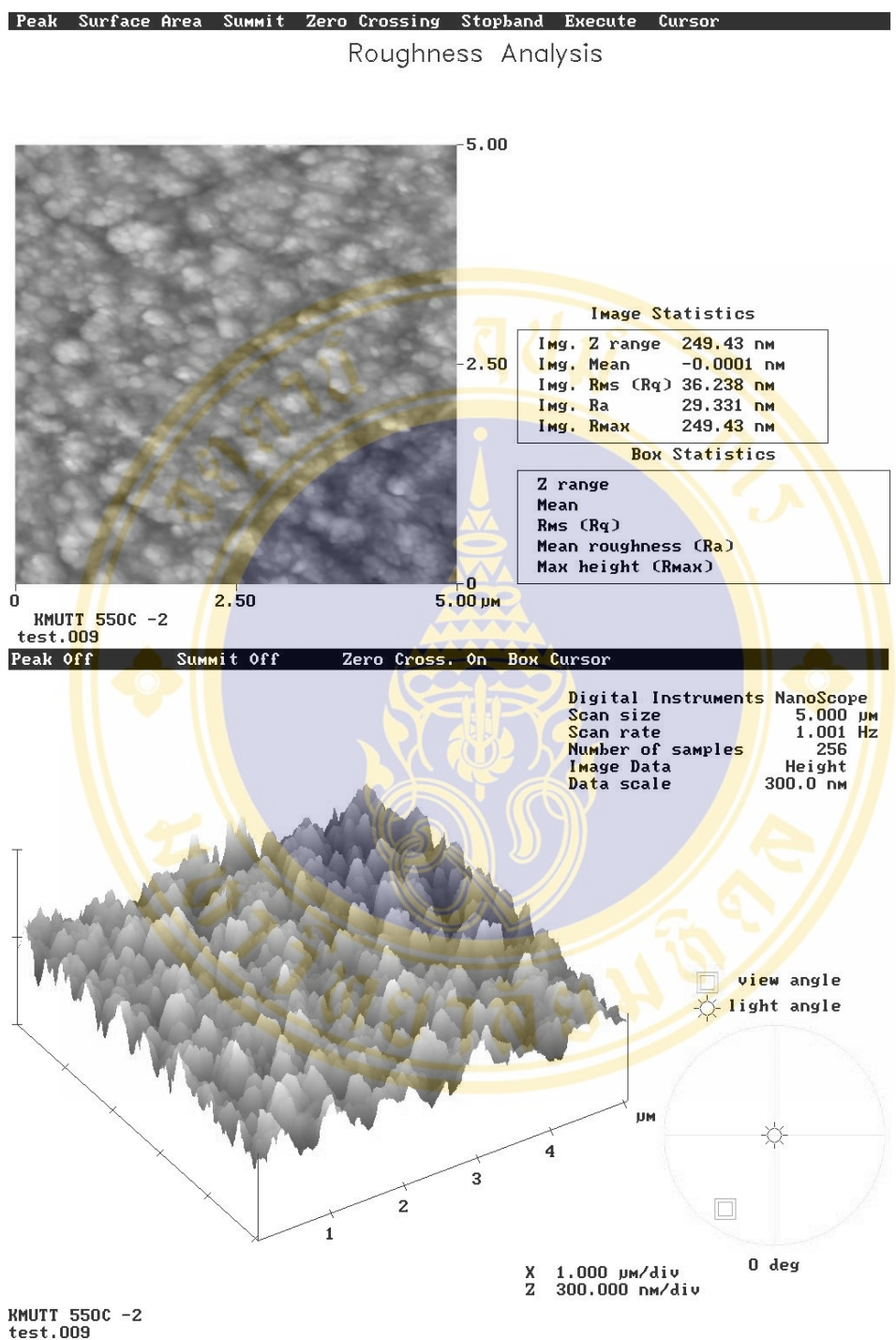


Figure 5.7 (d) Tapping mode image of AFM scan of $\text{Fe}_{40}\text{Ni}_{40}(\text{Si+B})_{19}\text{Mo}_{1-2}$ ribbon after annealing at 550 °C.

Atomic force microscopy (AFM) is a technique, which provides quantitative topographic data of solid surfaces. A sharp tip, which is attached to a cantilever-like spring, tracks the sample surface with sub-nanometer resolution. Therefore, molecular topographic features on a solid surface can be imaged on a routine basis. Figure 5.7 (a) – (d) show the tapping mode image of AFM scan of $\text{Fe}_{40}\text{Ni}_{40}(\text{Si}+\text{B})_{19}\text{Mo}_{1-2}$ ribbon before annealing and after annealing at 450 °C, 500 °C and 550 °C. The Rms roughness results of samples were shown in Table 5.11, which increased with respect to annealing temperature.

Table 5.11 Rms roughness of $\text{Fe}_{40}\text{Ni}_{40}(\text{Si}+\text{B})_{19}\text{Mo}_{1-2}$ at various annealing temperatures.

Annealing Temperature(°C)	Rms roughness(nm)
as-quenched	1.281
450	4.134
500	6.902
550	36.238

5.4 X- Ray Diffraction

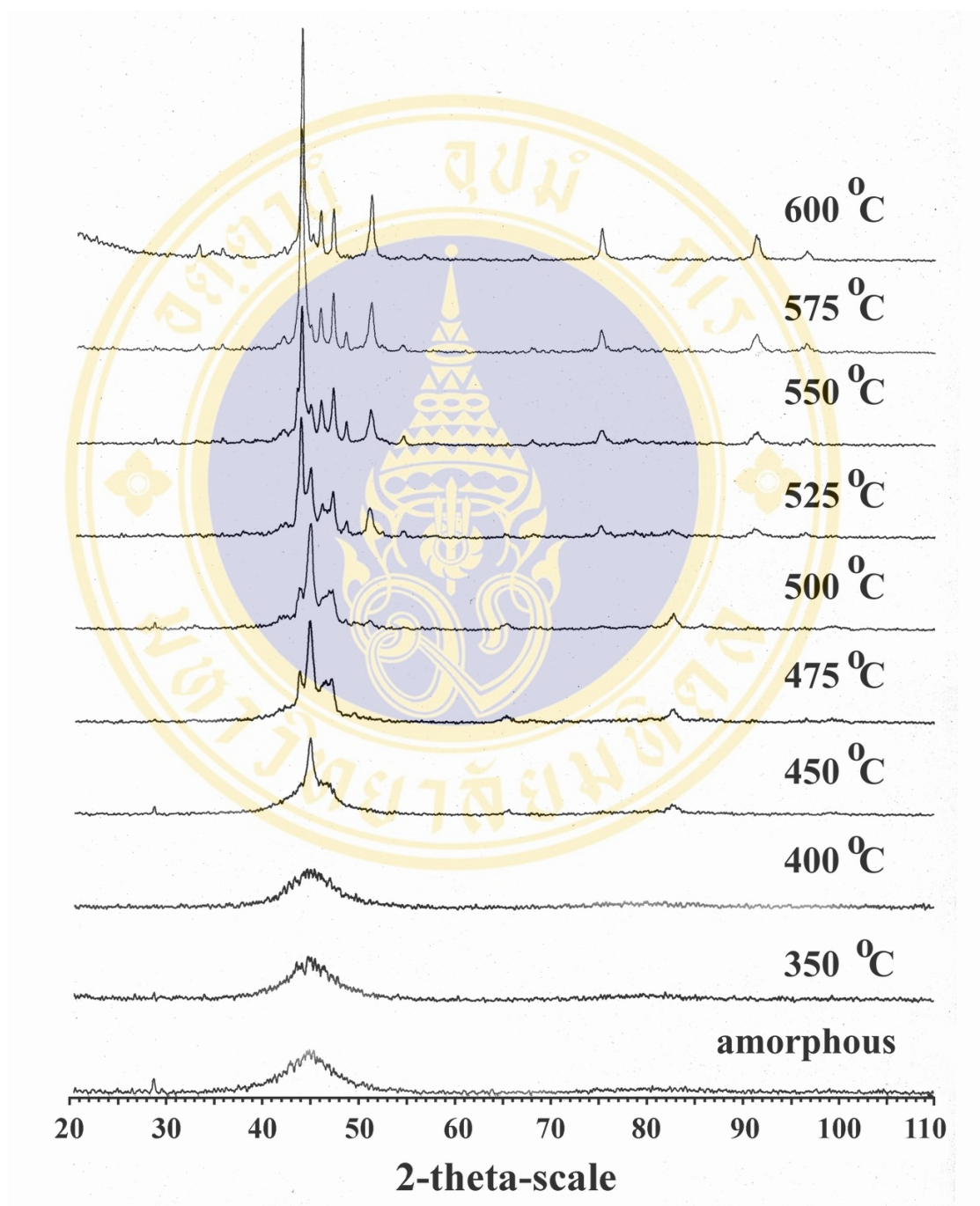


Figure 5.8 XRD patterns of $\text{Fe}_{40}\text{Ni}_{40}(\text{Si+B})_{19}\text{Mo}_{1-2}$ amorphous ribbon annealed at different temperatures.

The XRD patterns were analyzed to determine the structure of $\text{Fe}_{40}\text{Ni}_{40}(\text{Si}+\text{B})_{19}\text{Mo}_{1-2}$ at different temperatures. These patterns could be used to interpret any non-ferrous structure, which could not be observed by ^{57}Fe Mössbauer spectroscopy. Figures 5.8 showed the XRD patterns annealed at different temperatures. The broad peak in figure 5.9 (a) indicated the presence of the amorphous phase after annealing at 350 °C and 400 °C.

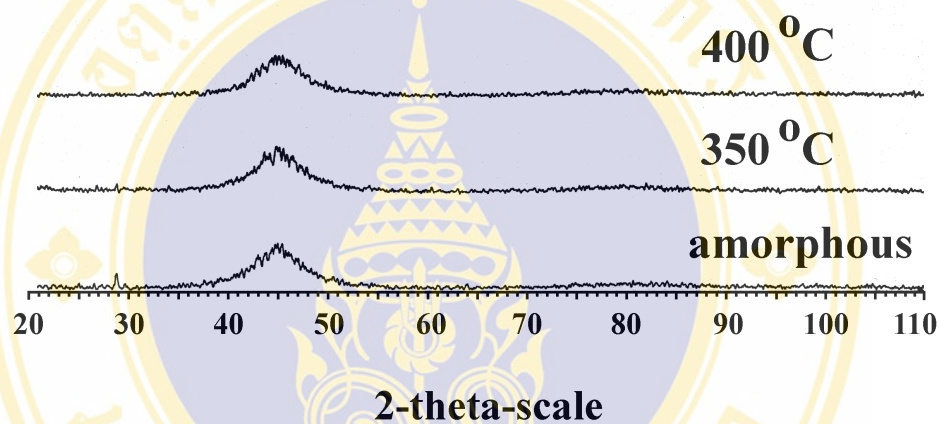


Figure 5.9 (a) Amorphous phase of $\text{Fe}_{40}\text{Ni}_{40}(\text{Si}+\text{B})_{19}\text{Mo}_{1-2}$ ribbon.

5.4.1 The First Crystallization

XRD results at 450 °C, 475 °C and 500 °C (fig. 5.9 (b)) showed the sharp peaks and the existence of a broad peak. The sharp peak belonged to the crystalline phase while the existence of a broad peak indicated the presence of remaining amorphous phase. At the first crystallization, the resulting phases were of $\alpha\text{-Fe}$, $\alpha\text{-Fe}(\text{Si})$ and $t\text{-Fe}_2\text{B}$ structure respectively. The increasing of intensities of sharp peaks with temperature was in agreement with the increasing amount of crystalline phases.

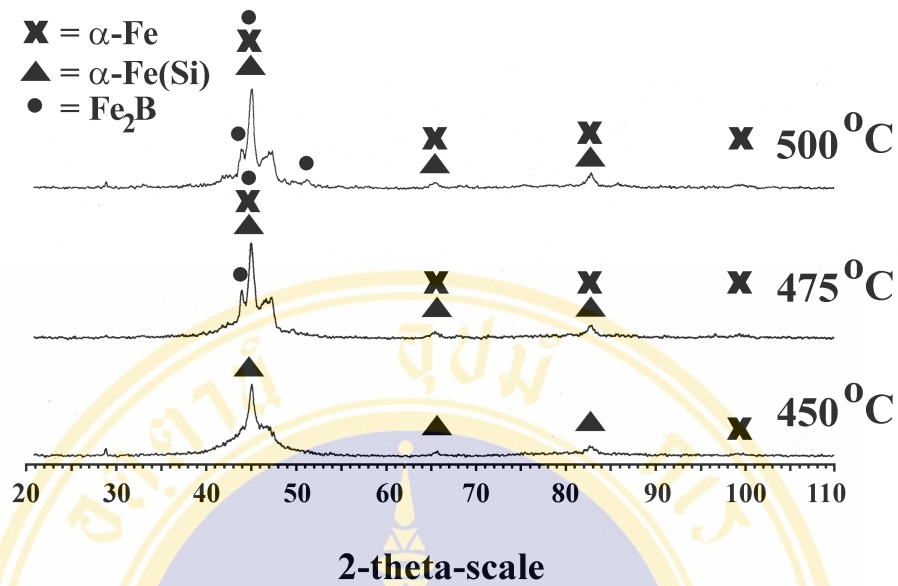


Figure 5.9 (b) Crystalline phases of partially crystallized of $\text{Fe}_{40}\text{Ni}_{40}(\text{Si}+\text{B})_{19}\text{Mo}_{1-2}$ ribbon.

5.4.2 The Second Crystallization

Figure 5.9 (c) shows the latter crystallization phases as the annealing temperature was raised further. At 525 °C, new sharp peaks appeared while the intensities of the peaks ($\approx 2\theta = 45^\circ, 65^\circ$ and 83°) of α -Fe and α -Fe(Si) were reduced. The increasing of the intensity of sharp peaks resulted from the crystallization of residual amorphous phase. The new crystalline phases were those of t - Fe_2B , t - Fe_3B , fcc -FeNi, c -Ni and Ni_2Si respectively. At 500 °C, all peaks belonging to α -Fe and α -Fe(Si) disappeared, while the peak intensities of t - Fe_2B , t - Fe_3B , fcc -FeNi, c -FeNi₃ and Ni_2Si phases increased. No new phase had been detected for the annealing temperature between 550 °C to 600 °C by XRD.

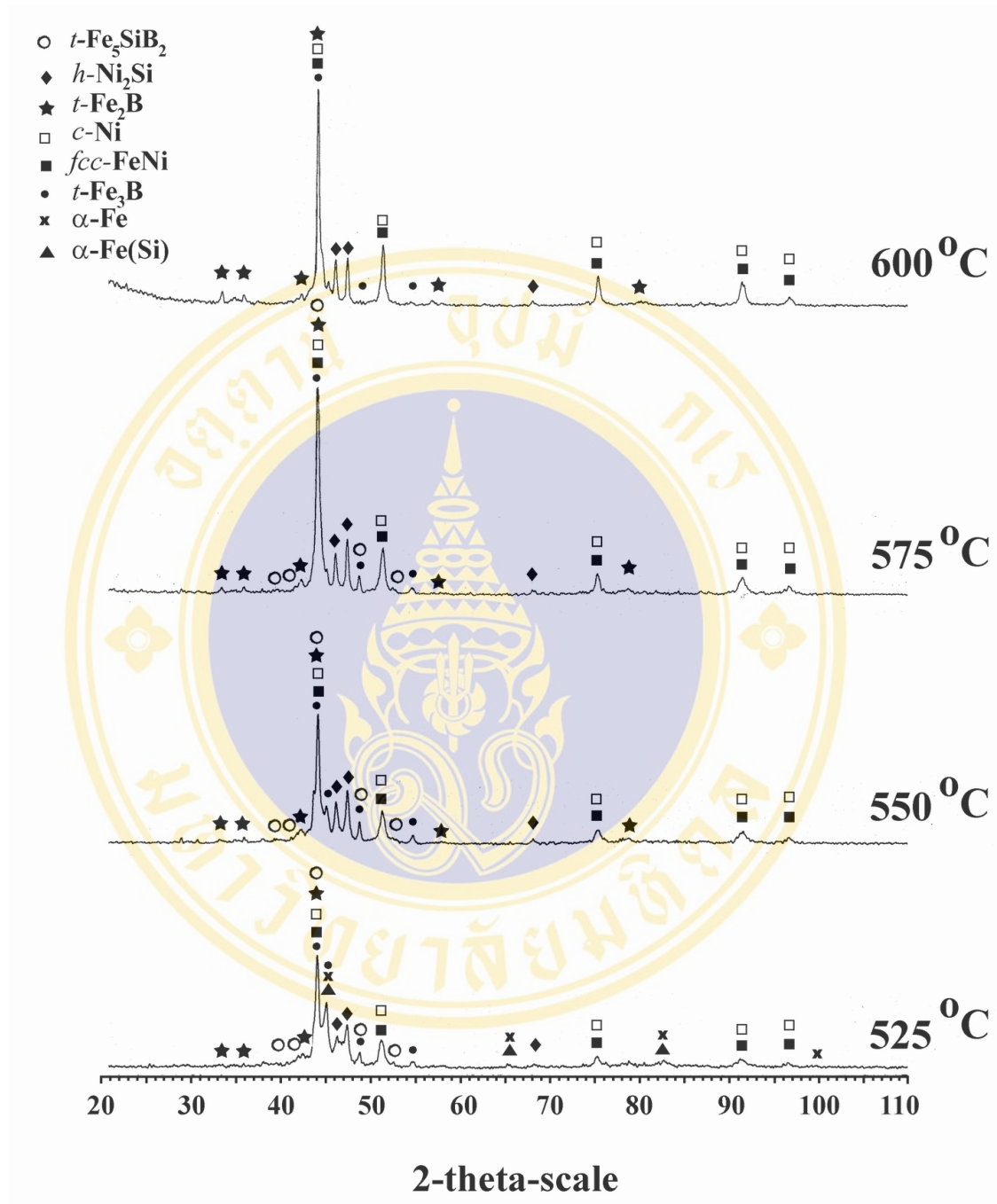


Figure 5.9 (c) Crystalline phases of completely crystallized of $\text{Fe}_{40}\text{Ni}_{40}(\text{Si+B})_{19}\text{Mo}_{1-2}$ ribbon .

5.4.3 Average grain size

Nanocrystalline alloys are above all crystalline and because of crystallinity they exhibit Bragg scattering peaks in X-ray diffraction experiments. However, due to their small size, significant fine particle broadening is observed in the Bragg peaks. The condition for constructive reinforcement of X-ray scattering from a crystalline solid is given by Bragg's Law:

$$n\lambda = 2d \sin \theta \quad (4)$$

This equates the path difference of X-rays scattered from parallel crystalline planes spaced $d=d_{hkl}$ apart to an integral (n) number of X-ray wavelengths λ . Here θ is the X-ray angle of incidence (and of diffraction) measured with respect to the crystalline planes. For an infinite crystal Bragg scattering occurs at discrete values of 2θ satisfying the Bragg condition, i.e. Bragg peaks are δ - functions. For finite sized crystals (Fig. 5.10) the peaks are broadened over a range of angles.

To better understand the phenomenon of fine particle broadening^[72], one considers a finite crystal of thickness, $t=md$, where m is an integer, and d is the distance between crystalline planes, i.e., there are m planes in t . Considering Fig. 25, if the broadened Bragg peak begins at an angle $2\theta_2$ and ends at $2\theta_1$, the breadth of the peak (or full width at half maximum) is given as:

$$B_\theta = \frac{1}{2}(2\theta_1 - 2\theta_2) = \theta_1 - \theta_2 \quad (5)$$

Now consider the path differences for each of the two angles θ_1 and θ_2 , for X-rays travelling the full thickness of the crystal:

$$(m+1)\lambda = 2t \sin \theta_1 \quad (6)$$

$$(m-1)\lambda = 2t \sin \theta_2 \quad (7)$$

and by subtraction:

$$\begin{aligned} t(\sin \theta_1 - \sin \theta_2) &= \lambda \\ &= 2t \cos\left(\frac{\theta_1 + \theta_2}{2}\right) \sin\left(\frac{\theta_1 - \theta_2}{2}\right) \end{aligned} \quad (8)$$

Now $\theta_1 + \theta_2 \sim 2\theta_B$ and $\sin((\theta_1 - \theta_2)/2) \sim (\theta_1 - \theta_2)/2$ so that

$$t = \frac{\lambda}{B_{\theta} \cos \theta_B} \quad (9)$$

A more exact empirical treatment yields:

$$t = \frac{0.9\lambda}{B_{\theta} \cos \theta_B} \quad (10)$$

which is known as the Scherrer formula. It states that for a crystal of thickness, t , we should expect a particle broadening of B of the Bragg peak at $2\theta_B$. For 50 nm particles an $\sim 0.20^\circ$ broadening is expected which is easily measured.

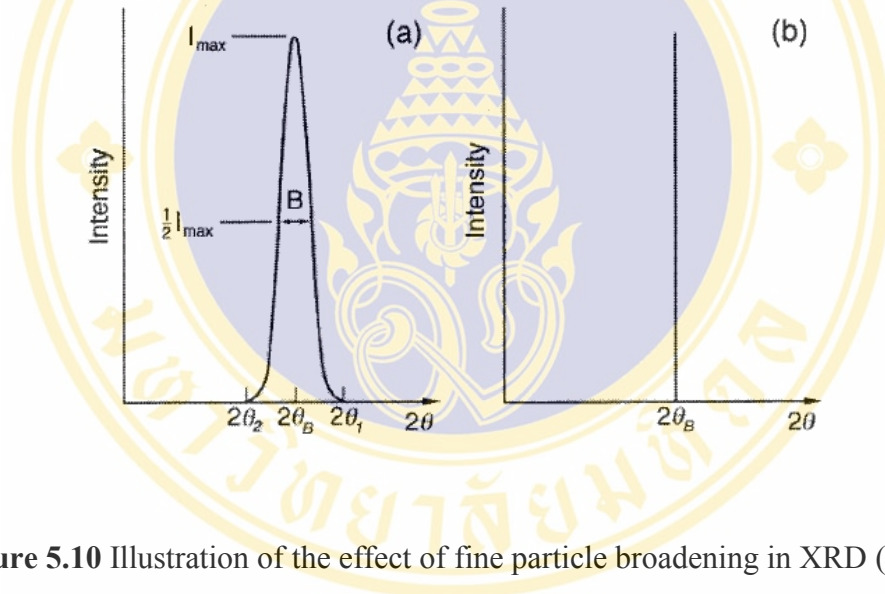


Figure 5.10 Illustration of the effect of fine particle broadening in XRD (a) fine particles and (b) perfect crystal ^[72].

The average grain sizes of α -Fe and α -Fe(Si) phases in the specimen were listed in Table 5.11, which showed that the average grain size of α -Fe increased with annealing temperature while the average grain size of α -Fe(Si) remained unchanged.

Table 5.12 Calculated average crystalline diameter from Scherrer formula.

Annealing temperature	Average grain size diameter(nm)	
	α -Fe	α -FeSi
450	36.59	37.79
475	51.57	29.92
500	54.65	37.99

5.5 Differential Thermal Analysis

Figures 5.11 (a) – (b) showed the differential thermal analysis (DTA) curves of $\text{Fe}_{40}\text{Ni}_{40}(\text{Si}+\text{B})_{19}\text{Mo}_{1-2}$ ribbon. The crystallization takes place in two stages: the first stage of crystallization at temperature 454 °C and the second at 525 °C. The former is due the crystallization from amorphous phase to crystalline phases, α -Fe and α -Fe(Si), while the latter corresponded to the crystallization of remaining amorphous phase and the transformation of α -Fe and α -Fe(Si) to t - Fe_3B , fcc -FeNi, c -Ni and Ni_2Si phases. The second run records the baseline of the first heating process.

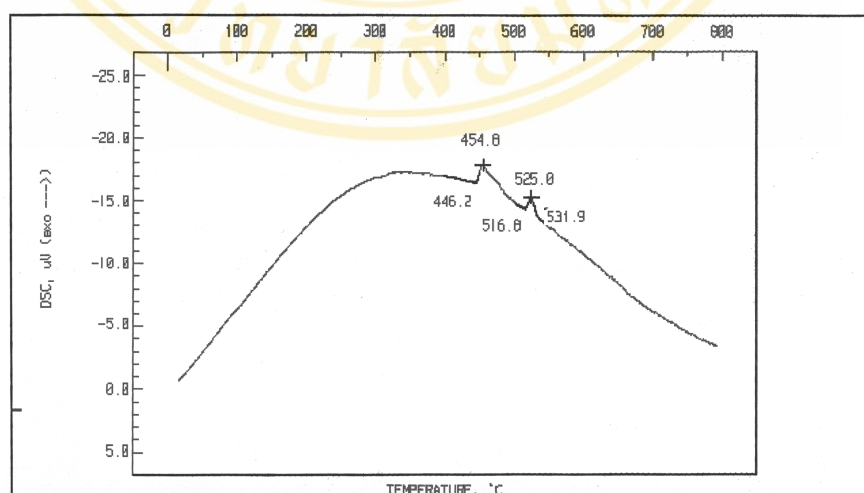


Figure 5.11 (a) First DTA scan of $\text{Fe}_{40}\text{Ni}_{40}(\text{Si}+\text{B})_{19}\text{Mo}_{1-2}$ ribbon from 0 - 800 °C under argon atmosphere.

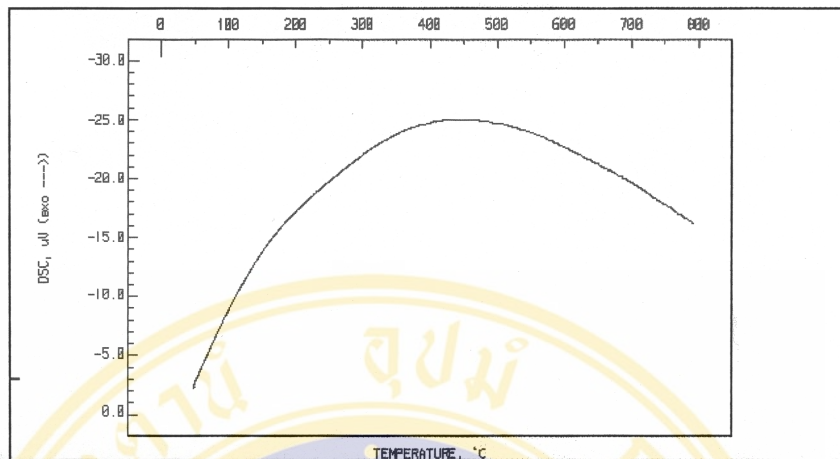


Figure 5.11 (b) Second DTA scan of $\text{Fe}_{40}\text{Ni}_{40}(\text{Si+B})_{19}\text{Mo}_{1-2}$ ribbon from 0 - 800 °C under argon atmosphere.

5.6 Vibrating Sample Magnetometer

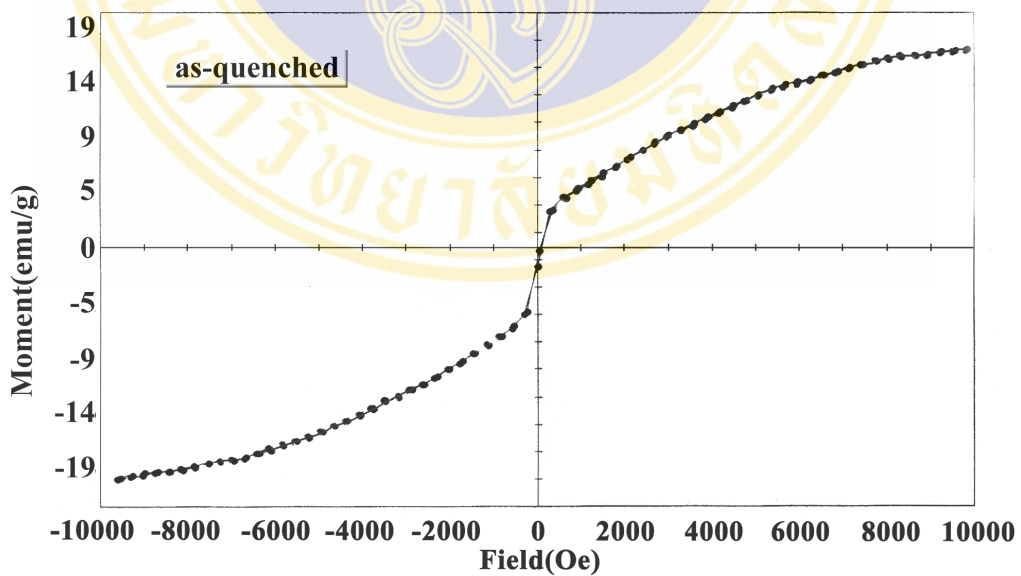


Figure 5.12 (a) Hysteresis loop at room temperature of $\text{Fe}_{40}\text{Ni}_{40}(\text{Si+B})_{19}\text{Mo}_{1-2}$ amorphous ribbon before annealing

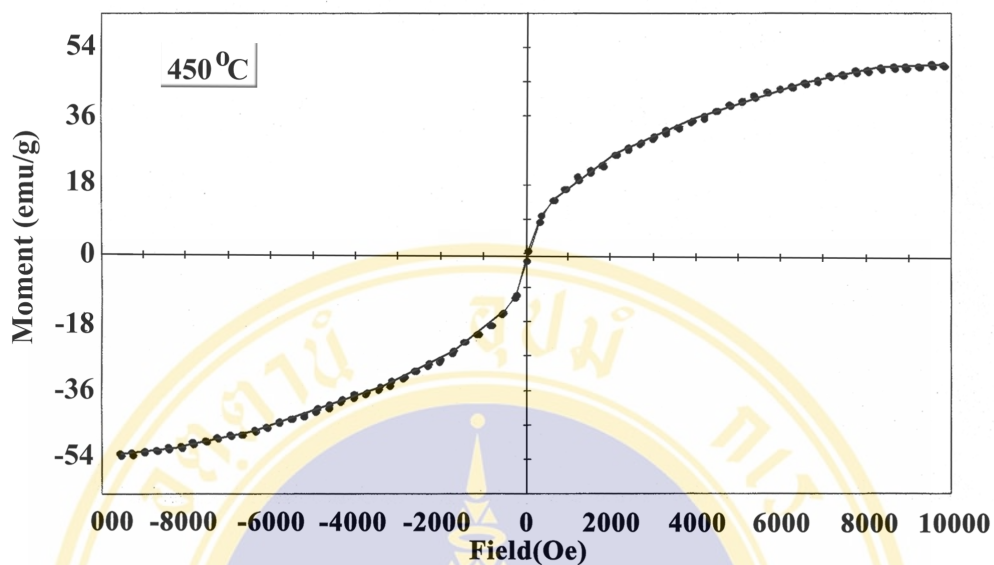


Figure 5.12 (b) Hysteresis loop at room temperature of $\text{Fe}_{40}\text{Ni}_{40}(\text{Si+B})_{19}\text{Mo}_{1-2}$ amorphous ribbon after annealing at 450 °C

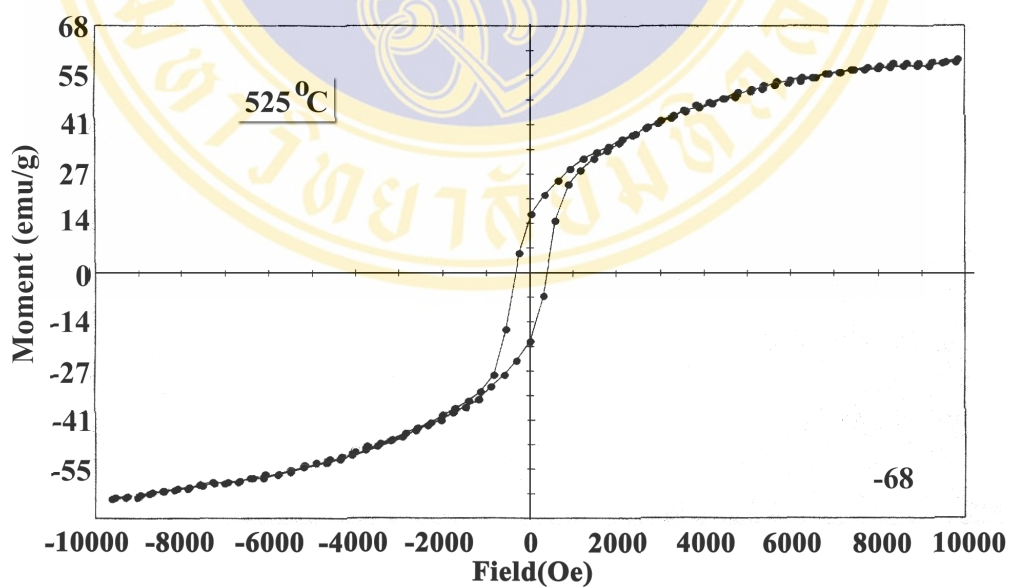


Figure 5.12 (c) Hysteresis loop at room temperature of $\text{Fe}_{40}\text{Ni}_{40}(\text{Si+B})_{19}\text{Mo}_{1-2}$ amorphous ribbon after annealing at 525 °C

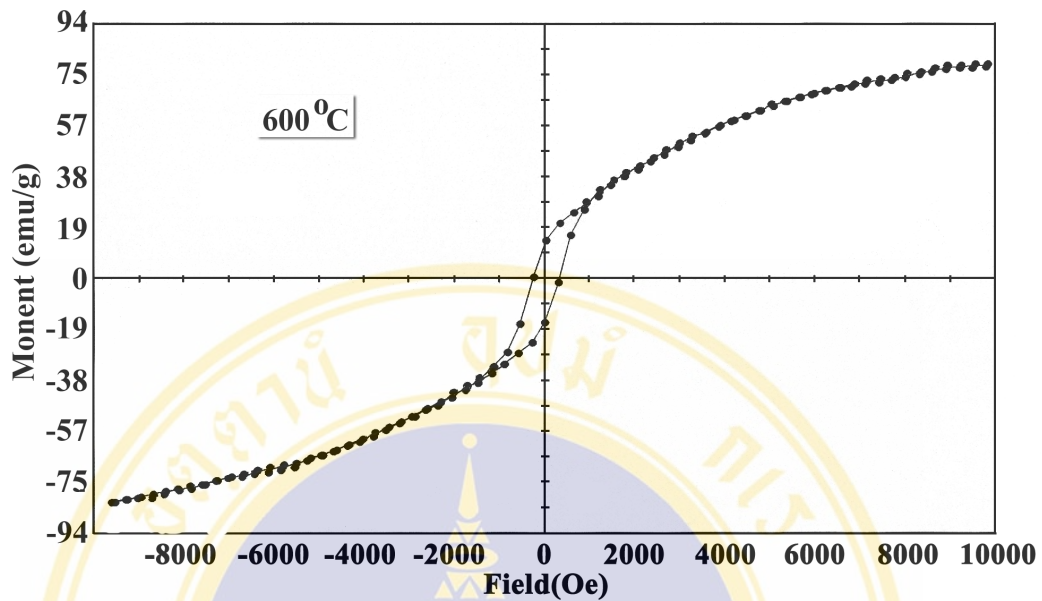


Figure 5.12 (d) Hysteresis loop at room temperature of $\text{Fe}_{40}\text{Ni}_{40}(\text{Si+B})_{19}\text{Mo}_{1-2}$ amorphous ribbon after annealing at $600\text{ }^{\circ}\text{C}$

Table 5.13 VSM results

Annealing Temperature ($^{\circ}\text{C}$)	Coercivity; H_c (Oe)	Remanant Magnetization; M_r (emu/g)	Magnetization; M_s (emu/g)
0	44.51	0.21	18.49
450	7.981	0.70	51.07
525	351.6	17.40	61.10
600	291.8	14.21	74.14

5.7 Ferromagnetic Resonance

5.6.1 Method of analysis of FMR

The coordinate system used for the analysis is shown in figure 5.13. H , M and h are the vectors of the DC magnetic field, magnetization and the small oscillating magnetic field of the microwave, respectively $\theta_{H(M)}$ and $\phi_{H(M)}$ are the polar and azimuthal angles of DC magnetic field (magnetization). The total magnetic energy per unit volume the ribbon is given by

$$E = -M_s H [\sin \theta_H \sin \theta_M \cos(\phi_H - \phi_M) + \cos(\theta_H - \theta_M)] + 2\pi M_s^2 \cos^2 \theta_M - K_{\perp} \cos^2 \theta_M \quad \dots(9)$$

where the first, second and third terms represent the Zeeman energy, the demagnetization energy and the perpendicular anisotropy energy, respectively. Here, K_{\perp} is the perpendicular magnetization anisotropy constant. The resonance field (H_R) of FMR spectrum is determined by the resonance condition ^[75], which is generally given by

$$\left(\frac{\omega}{\gamma}\right)^2 = \frac{1}{(M_s \sin \theta_M)^2} (E_{\theta_M \theta_M} E_{\phi_M \phi_M} - E_{\theta_M \phi_M}^2) \quad (10)$$

Here, ω and M_s are the angular frequency of microwave and saturation magnetization, respectively. γ is the gyromagnetic ratio, which is given by

$$\gamma = \frac{g\mu_B}{\hbar} \quad (11)$$

where g , μ_B and \hbar are g-factor, Bohr magneton and Plank's constant, respectively.

$E_{ij}(i, j = \theta_M, \phi_M)$ is the partial derivative of E . θ_M and ϕ_M at resonance are determined by $\frac{\partial E}{\partial \theta_M} = 0$ and $\frac{\partial E}{\partial \phi_M} = 0$. Using eq.(X), θ_M resonance is determined by solving the

following equation numerically,

$$\sin(2\theta_M) = \frac{(2H_R)}{4\pi M_{eff}} \sin(\theta_M - \theta_H) \quad (12)$$

and $\phi_M = \phi_H$. Here $4\pi M_{eff}$ is the effective demagnetization of the ribbon, which can written as

$$4\pi M_{eff} = 4\pi M_s - H_{\perp} \quad (13)$$

where $H_{\perp} = \frac{2K_{\perp}}{M_S}$ is the perpendicular anisotropy field. By using E_{ij} from eq. (10-13)

the following equation can be obtained,

$$\begin{aligned} \left(\frac{\omega}{\gamma}\right)^2 &= H_1 \times H_2 \\ H_1 &= H_R \cos(\theta_H - \theta_M) - 4\pi M_{eff} \cos^2 \theta_M \\ H_2 &= H_R \cos(\theta_H - \theta_M) - 4\pi M_{eff} \cos 2\theta_M \end{aligned} \quad (14)$$

H_R as a function of θ_H is calculated numerically using eq.(12)-(14) the parameters, $4\pi M_{eff}$ and g -factor.

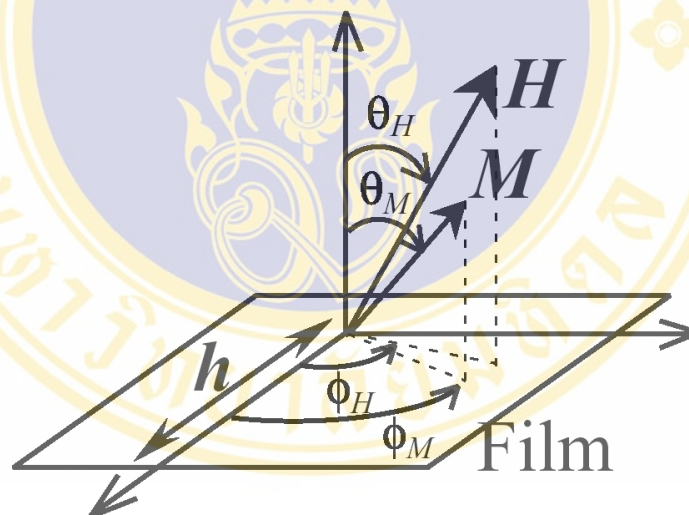


Figure 5.13 Schematic illustrations of the coordinate system used in the analysis of FMR

Amorphous

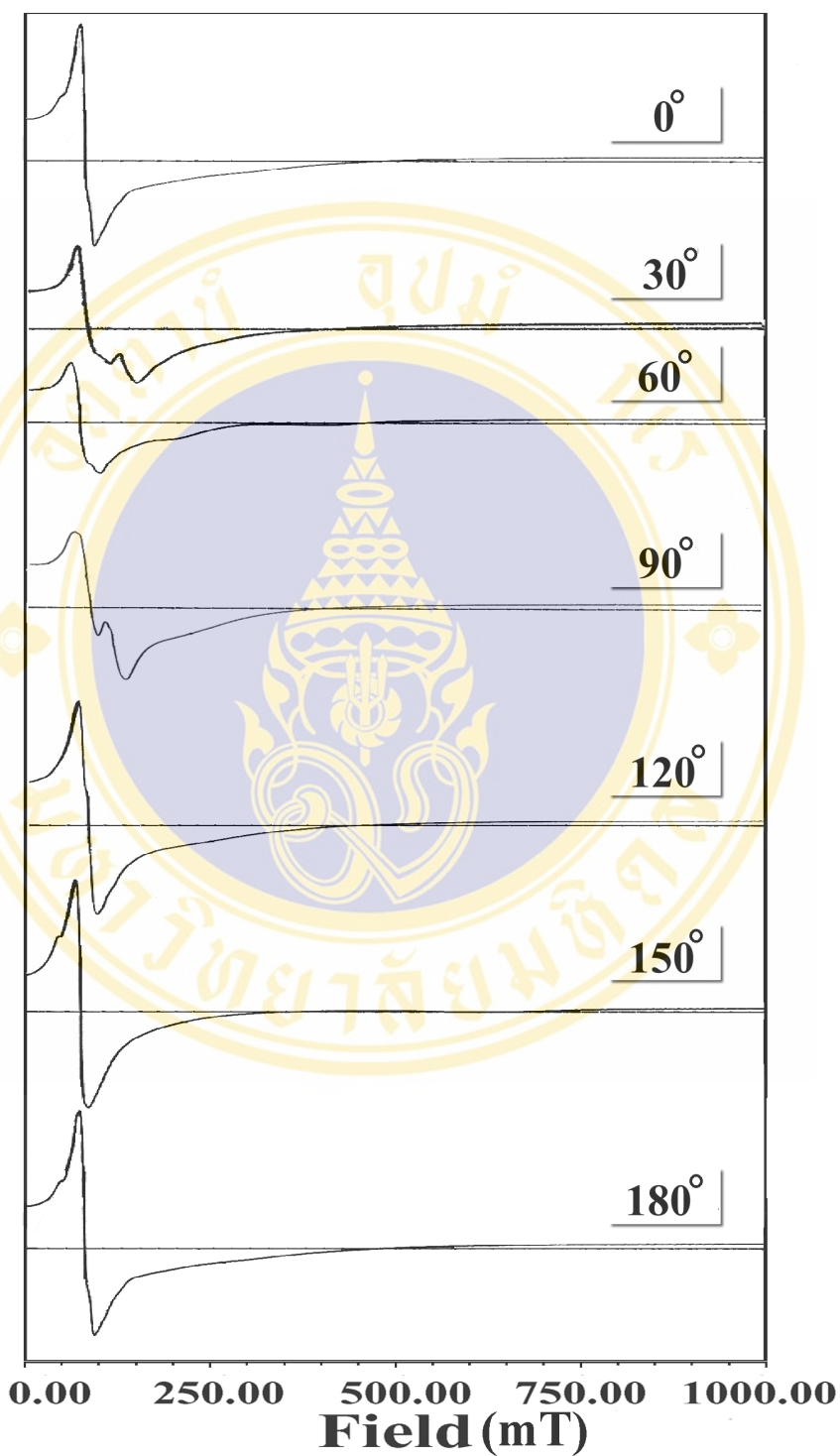


Figure 5.14 (a) FMR spectra of $\text{Fe}_{40}\text{Ni}_{40}(\text{Si+B})_{19}\text{Mo}_{1-2}$ before annealing at various angles(ϕ) of the applied external field.

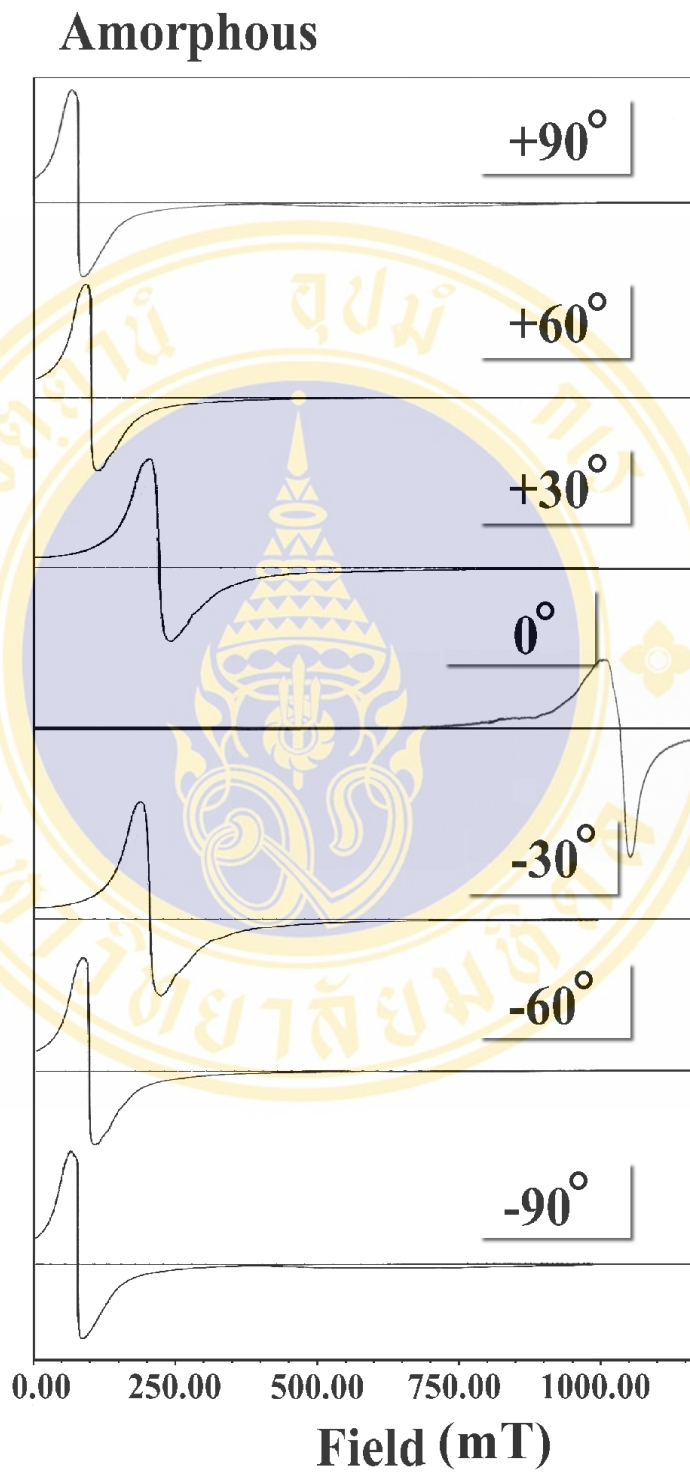


Figure 5.14 (b) FMR spectra of $\text{Fe}_{40}\text{Ni}_{40}(\text{Si+B})_{19}\text{Mo}_{1-2}$ before annealing at various angles(θ) of the applied external field.

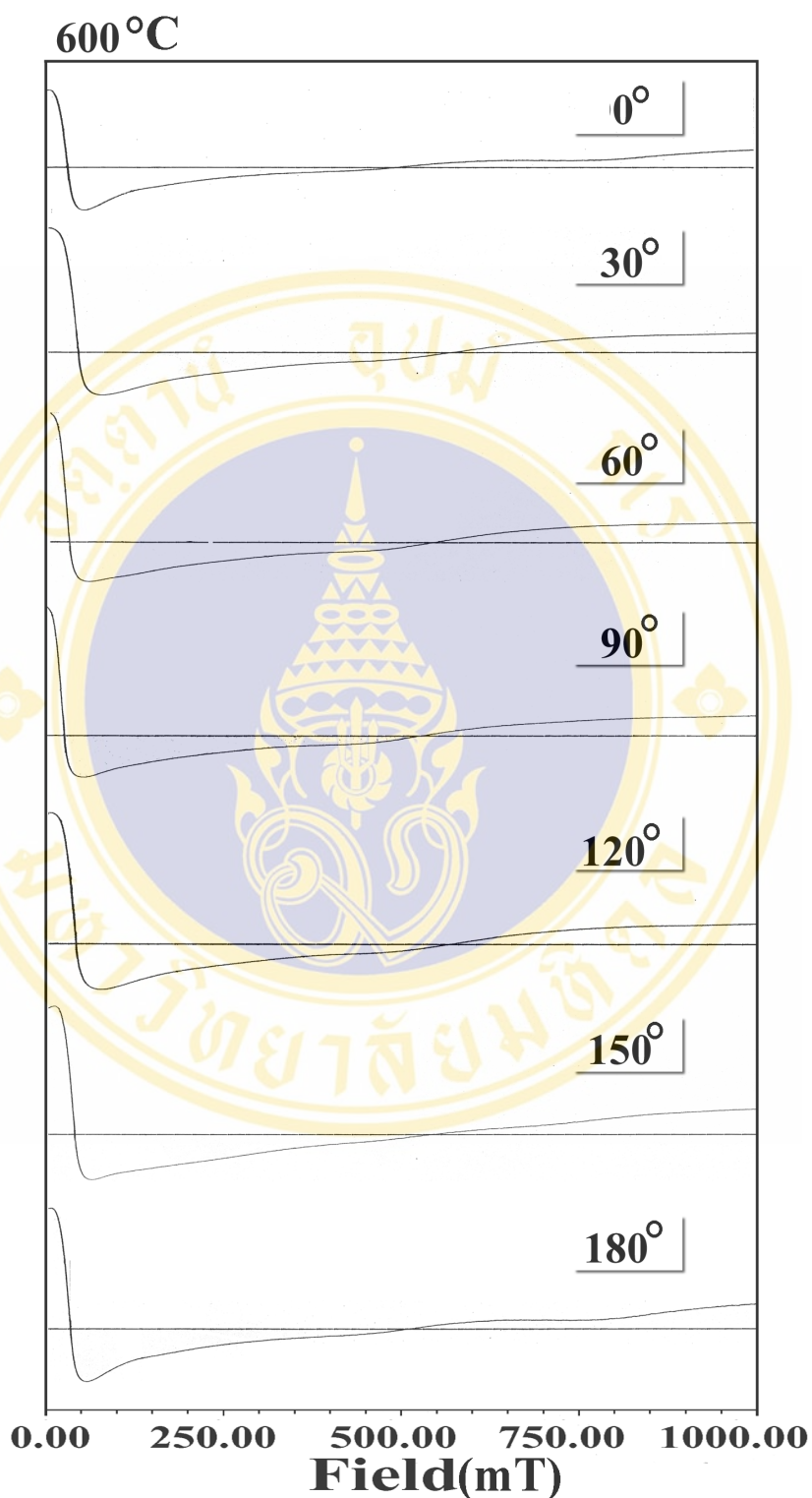


Figure 5.14 (c) FMR spectra of $\text{Fe}_{40}\text{Ni}_{40}(\text{Si+B})_{19}\text{Mo}_{1-2}$ after annealing at $600\text{ }^\circ\text{C}$ at various angles(ϕ) of the applied external field.

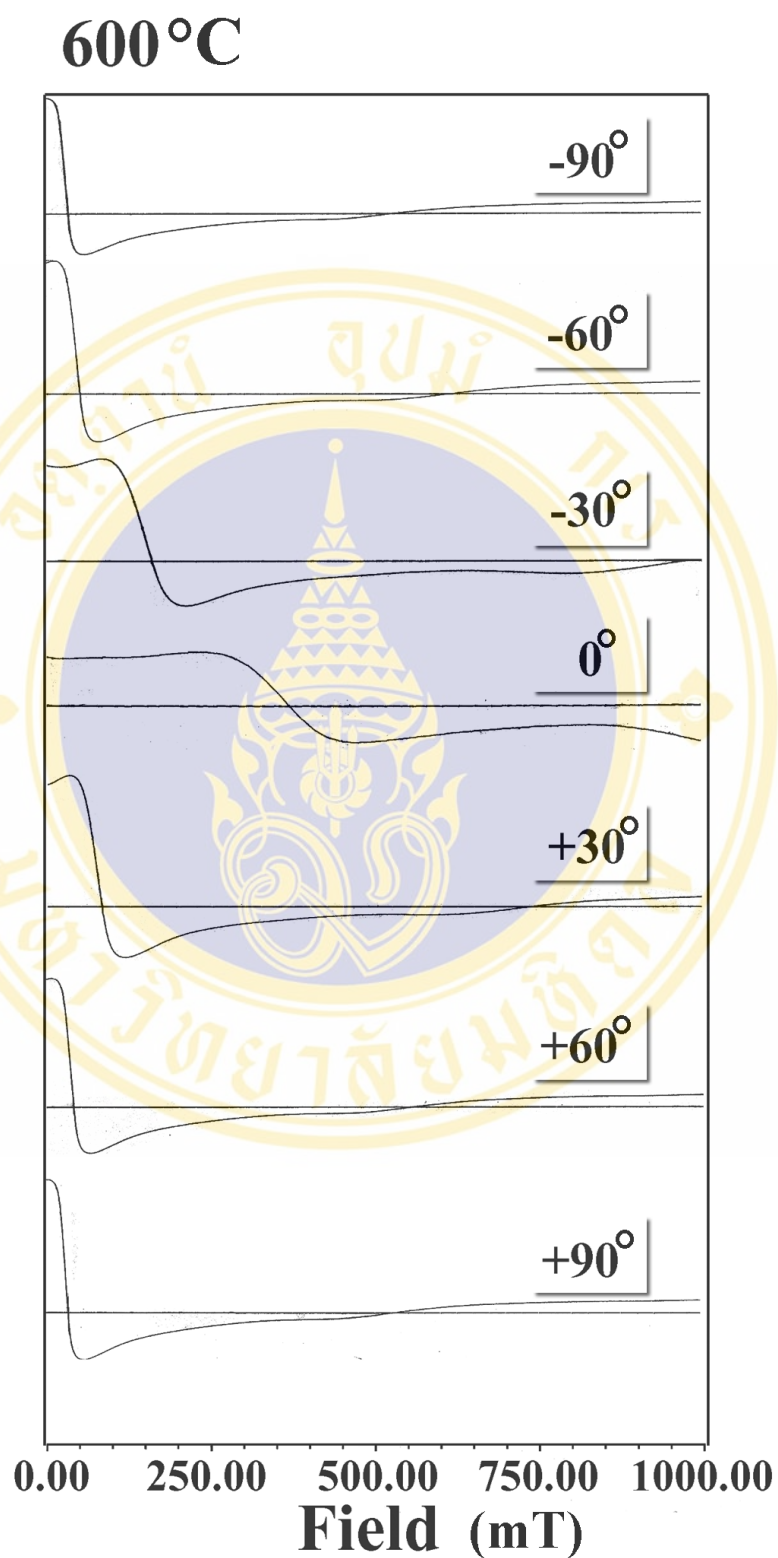


Figure 5.14 (d) FMR spectra of $\text{Fe}_{40}\text{Ni}_{40}(\text{Si+B})_{19}\text{Mo}_{1-2}$ after annealing at 600 °C at various angles(θ) of the applied external field.

Two sets of FMR experiments were made on two samples at different orientations of the static magnetic field H with respect to normal of ribbon plane. The first set of experiments, H was perpendicular to the ribbon plane. The sample was rotated about the normal of the ribbon 30-degree step (ϕ) and measured the FMR spectra. In the second set of experiments, the normal of the ribbon plane was rotated so that the normal made angle (θ) with H . The FMR spectra were recorded for every 30 degrees of theta. Typical FMR spectra for H perpendicular to the ribbon plane and for H making a certain angle with the normal of the plane for the as-quenched sample are shown in Fig. 5.14 (a) and Fig 5.14 (b). In the second set of experiments, the highest resonance absorption peak can be observed at 1030.79 mT when H is perpendicular to the normal of the ribbon (i.e. $\theta_H = 90^\circ$) and the resonance peak shifts to lower field for other angles. In the first set of experiments, however, the maximum resonance absorption peak is observed at 80 mT in agreement with the fact the magnetization is more or less in the ribbon plane. More absorption peaks at lower fields can be observed at other values of phi, 30°, 60° and 90°, which are probably due to the inhomogeneity of the ribbon.

FMR results from the sample annealed at 600 °C are shown in Fig. 5.14 (c) and Fig 5.14 (d). In the second set of measurements, the maximum resonance absorption peak can be observed at 370.51 mT when H is parallel to the normal ($\theta_H = 0^\circ$) of the ribbon plane. The resonance peak shifts to lower field for other orientations. In the first set of experiments, however, one strong and weaker resonance absorption peaks are observed. The sharp absorption peak is located at 30 mT but the weak resonance peak is very broad.

When both FMR results of the as-quenched and the annealed samples are compared, it is clear that the maximum absorption peak of the annealed sample is at lower magnetic field than of that the as-quenched one. This is due to the fact that there is a change in magnetization after the crystallization and the magnetization is almost perpendicular to the ribbon plane as shown in figure 5.15.

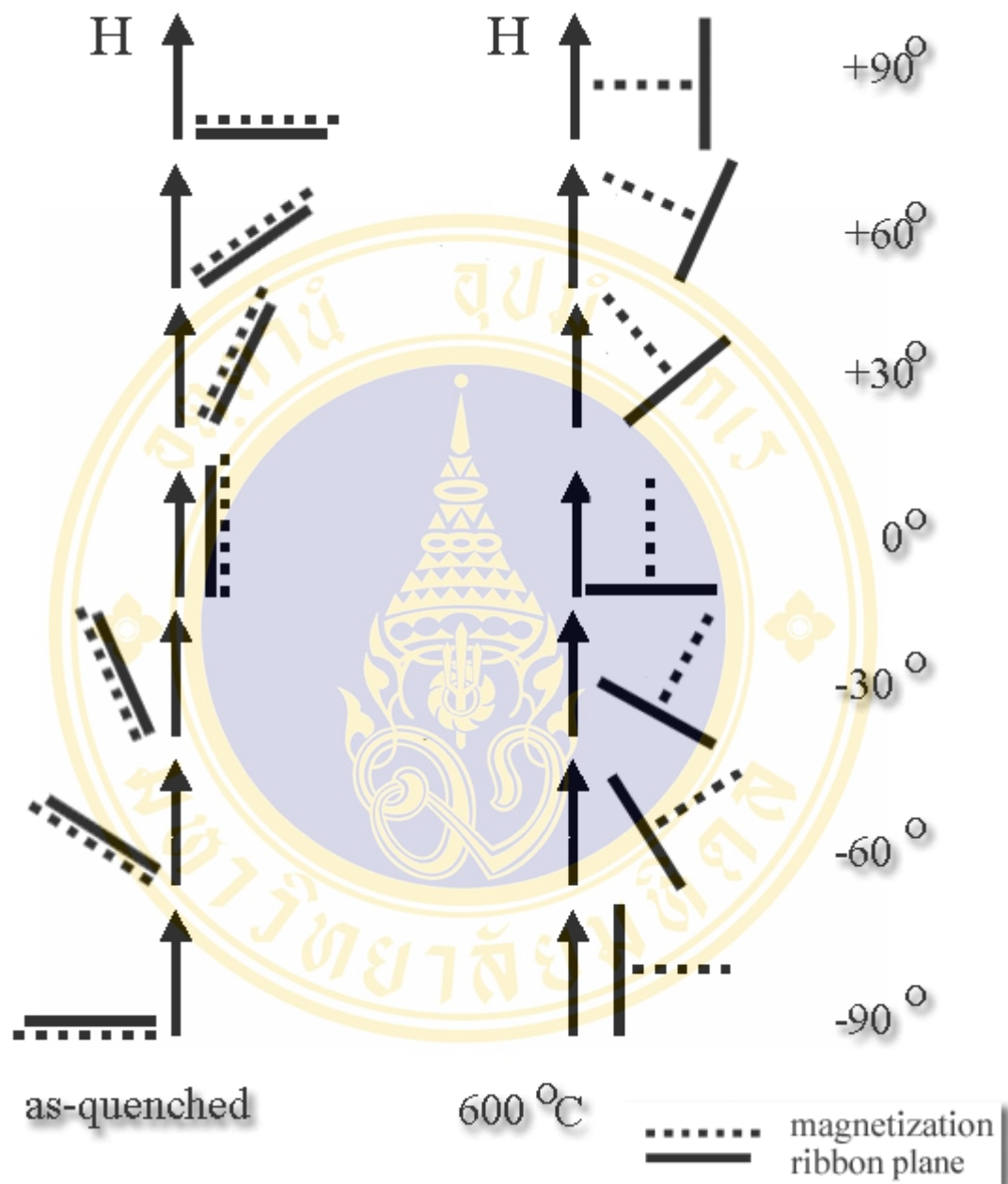


Figure 5.15 Schematic representation the direction of the magnetization, magnetic field and ribbon plane.

CHAPTER VI

CONCLUSION

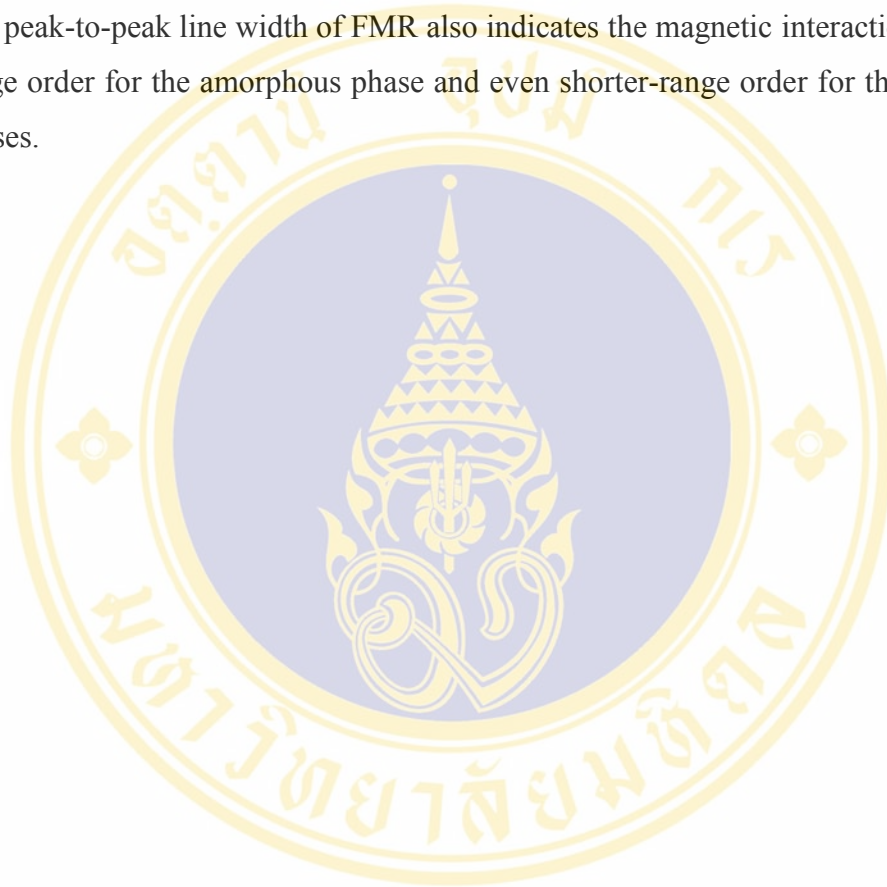
The evolution of crystallization process of $\text{Fe}_{40}\text{Ni}_{40}(\text{Si+B})_{19}\text{Mo}_{1-2}$ amorphous ribbon annealed at various temperatures was studied by several techniques. Mössbauer spectroscopy, XRD, SEM and DTA could monitor the crystallization behaviors respectively, whereas magnetic properties were examined by VSM and FMR techniques.

The results may be divided into three stages according to the crystallization evolution behavior. In the first stage the samples still remain in the amorphous phase for annealing temperatures of 350 °C, 400 °C similar to the as-quenched one except some reorientations of the magnetization. The results from Mössbauer spectroscopy show very small change in the magnetic structure, which agree with the XRD results that no crystalline phase can be detected.

In the second stage the samples annealed at 450 °C, 475 °C and 500 °C are partially crystallized. This is composed of some crystalline phases embedded in residual amorphous matrix. The amount of amorphous phase decreased while the crystalline phases increased after annealing at higher temperature. The first crystalline phases are of α -Fe, α -Fe(Si) and t -Fe₂B respectively. A new crystalline phase, fcc -FeNi, can be detected at 500 °C. The average nanograin sizes of α -Fe and α -Fe(Si) are in range of 30-50 nm and 40 nm respectively, depending on the annealing temperature.

In the last stage, the specimens annealed at 525 °C, 550 °C, 575 °C and 600 °C, have been completely crystallized and the amorphous phase can no longer be detected. At 525 °C, Mössbauer results show six different types of Fe-based crystalline phase; α -Fe, α -Fe(Si), t -Fe₅SiB₂, t -Fe₂B, t -Fe₃B and fcc -FeNi., while XRD results indicate that there are a few Ni-compounds(c -Ni and h -NiSi). At 550 °C and 575 °C, the types of Fe-based compounds decreases from six to four and α -Fe and α -Fe(Si) disappear at this stage. The final annealing temperature at 600 °C, Mössbauer results show only t -Fe₂B, t -Fe₃B and fcc -FeNi phases, while t -Fe₅SiB₂ phase vanishes. The average grain size of these crystals is in the order of micrometer.

The magnetic properties measured by VSM show that the magnetization increases with the annealing temperature. The magnetization also exhibits hysteresis behaviour, which indicates the presence of some magnetic domains after heat treatments. FMR results show that the magnetization of amorphous ribbon is in the plane and is more or less perpendicular to the ribbon plane after annealing at 600 °C. The peak-to-peak line width of FMR also indicates the magnetic interactions are short-range order for the amorphous phase and even shorter-range order for the crystallized phases.



REFERENCES

1. Brenner A, Burkhead PS and Sentel CA. US Patents No.2,653,128 (September 22, 1953).
2. Chen HS and Plok DE. US Patents No.3,856,513 (December 24, 1974).
3. Hasegawa R. Amorphous magnetic Materials – a history. *J.Magn.Magn.Mater.* 1991; 100:1-12.
4. Chen HS and Millers CE. *Rev. Sci.Istrum.*, 41(1970), 1237
5. Klement. Jr W, Willens R H and Duwez P. Non-crystalline structure in solidified Gold-Silicon Alloys. *Nature* 1960; 187:869-870.
6. Cohen MH and Turnbull D. Composition requirements for glass formation in Matallic and ionic systems. *Nature* 196; 189:131-132.
7. McCurrie RA, *Ferromagnetic Materials Structure and properties.*, Academic Press, Great Britain, 1994, 98
8. Mc Henry ME, Willard MA, and Laughlin DE. Amorphous and nanocrystalline materials for applications as soft magnets. *Progress in Materials Science.* 1999; 44:291-433.
9. Lu K. Nanocrystalline metals crystallized from amorphous solids: nanocrystallization, structure and properties. *Materials Science and Engineering.* ;1996 R16:161-211.
10. Lu K, Wang JT and Wei WD. A new method for synthesizing nanocrystalline alloys. *J. Appl. Phys.* 1991; 69:522-524.
10. Liu XD, Ding BZ, Hu ZQ, Lu K, and Wang YZ. Properties of nanocrystalline Fe-Cu-Si-B alloys generated by crystallization of the amorphous alloy. *Physica B.* 1993; 192:345-350.
12. Lu K, Liu XD, Yuan FH. and Wei WD. Microstructure and mechanical property of nanocrystalline NiZr₂ intermetallic compound. *J. Mater. Sci. & Tech.* 1996; 12:409-412.

13. Sui ML, Xing LY, Deng W, Lu K, Patu S and He YZ. Investigation of the interfacial defects in a nanocrystalline Ni-P alloy by positron annihilation spectroscopy *J. Appl. Phys.* 1991; 69:4451-4453.
14. Yoshizawa Y, Oguma S and Yamauchi K. New Fe-based soft magnetic alloys composed of ultrafine grain structure. *J. Appl. Phys.* 1988; 64:6044-6049.
15. Conde CF, Millian M and Conde A. Thermomagnetic study of devitrification in nanocrystalline Fe(Cr)SiB-CuNb alloys. *J. Magn. Magn. Mater.* 1994; 198:314-318.
16. Trudeau ML, Schulz R, Dussault D and VanNeste A. Structural changes during high-energy ball milling of iron-based amorphous alloys: Is high-energy ball milling equivalent to a thermal process. *Phys. Rev. Lett.* 1990; 64:99-102.
17. Koster U and Weiss P, *J. Non-Cryst. Solids*, 17(1975) 359.
18. Vavassori P, Ronconi F, Traldi M and Puppini E. Surface crystallization and frequency dependence of AC coercivity in Fe₈₀B₂₀ amorphous alloy. *J. Magn. Magn. Mater.* 1998; 177-181:127-128.
19. Murphy KA and Hershkowitz N. Temperature-dependent hyperfine interactions in Fe₂B. *Phys. Rev. B* 1973; 7:23-31.
20. Barault G and Greneche JM. Reinvestigation of the hyperfine field distributions in Fe-B metallic amorphous alloys. *Solid State Commun* 1995; 96:150-160.
21. Sánchez FH, Zang YD, Budnick JI and Hasegawa R. Mössbauer study of the crystallization of Fe_{100-x}B_x amorphous alloys. *J. Appl. Phys* 1989; 68:1671-1675.
22. Ruuskanen P and Heczko O. Formation of amorphous Fe_{1-x}B_x alloys during solid state alloying with hexane. *J. Non-Cryst. Solids* 1998; 224:36-42.
23. Balogh J, Kemény T, Vincze I, Bujdosó L, Tóth L and Vincze G. Amorphous alloy formation by mechanical alloying and consecutive heat treatment in Fe₅₀B₅₀ powder mixture. *J. Appl. Phys* 1995; 77:4997-5003.

24. Arshed M, Siddique M, Anwar-ul-Islam M, Ashfaq A, Shamim A and Butt NM. Isochronal crystallization of metglass $\text{Fe}_{83}\text{B}_{17}$ using mossbauer effect and resistivity measurements. *Solid State Commun* 1996; 98:427-430.
25. Yiping L, Hadjipanayis GC, Papaefthymiou V and Kostikas A. Heat treatment effects on structural and magnetic properties of fine Fe-B particle. *J. Magn. Magn. Mater.* 1996; 164:357-366.
26. Dalocan V and Dolocan E. Magnetic field dependence of the permeability in amorphous magnetic materials. *J. Magn. Magn. Mater.* 1995; 140-144:1911-1912.
27. Ole HN and Morrish AH. Amorphous-to-crystalline transformation of $\text{Fe}_{82}\text{B}_{12}\text{Si}_6$. *Phys. Rev. B* 1980; 22:3471-3480.
28. Singhal R. and Majumdar AK. Crystallization of glassy $\text{Fe}_{80}\text{B}_{20-x}\text{Si}_x$ alloys *J. Magn. Magn. Mater.* 1992; 115:245-249.
29. Kulik T and Kopewicz M. Effect of quenching rate on magnetic properties and local magnetic anisotropy on $\text{Fe}_{78}\text{B}_9\text{Si}_{13}$ glass *J. Magn. Magn. Mater.* 2000; 215-216:455-458.
30. Raa MM, ChaHopadhyay K, Majumdar B, and Nanayanasamy A. Structural and Sort Magnetic Properties of Finemet Alloys *J. Alloy. Comp* 2000; 297:199-205.
31. Schurer PJ. Mössbauer study of amorphous $\text{Fe}_{78}\text{B}_{12}\text{Si}_{10}$. *Phys. Rev. B.* 1979; 20:4660-4664.
32. Hang NO, Kyung SB and Chul SK, Magnetic properties and the crystallization of amorphous $\text{Fe}_{75.4}\text{B}_{14.2}\text{Si}_{10.4}$. *Phys. Rev. B.* 1981; 4: 6600-6609.
32. Saegusa N and Morrish AH, Atomic rearrangements and crystalline transformations in amorphous $\text{Fe}_{81}\text{B}_{13.5}\text{Si}_{3.5}\text{C}_2$. *Phys. Rev. B.* 1982; 26:305-314.
33. Saegusa N and Morrish AH, Surface atomic rearrangements and crystalline transformations in amorphous $\text{Fe}_{81}\text{B}_{13.5}\text{Si}_{3.5}\text{C}_2$ ribbons. *Phys. Rev. B.* 1982; 26:6547-6553.

34. Saegusa N and Morrish AH. Mössbauer study of the kinetics of the amorphous-to-crystalline transformation in amorphous $\text{Fe}_{81}\text{B}_{13.5}\text{Si}_{3.5}\text{C}_2$. Phys. Rev. B. 1983; 27:4027-4033.
35. A Bhatnagar. K and Bhanu PB. Study of magnetic and hyperfine interactions in the quaternary amorphous alloy $\text{Fe}_{81}\text{B}_{13.5}\text{Si}_{3.5}\text{C}_2$. Phys. Rev. B. 1983; 29:4896-4903.
36. Methasiri T and Tang I. M. Mössbauer studies on annealed $\text{Fe}_{81}\text{B}_{13.5}\text{Si}_{3.5}\text{C}_2$ amorphous ribbons. Physica. B. 1985; 133:37-42.
37. Arshed M, Siddique M, Anwar-ul-Islam M and Butt NM. Study of crystallization process of metglass $\text{Fe}_{86}\text{B}_{14}$ by Mössbauer effect and resistivity measurements. Solid State. Commun. 1994; 89:101-104.
38. Botta WJ, Negri FD and Yazari AR. Crystalline of Fe-based amorphous alloys. J. Non-Cryst. Solids. 1999; 247:19-25.
39. Sórescu M, Knobbe ET and Barb D. Excimer laser processing of amorphous and nanocrystalline $\text{Fe}_{73.5}\text{Cu}_1\text{Nb}_3\text{Si}_{22.5-x}\text{B}_x$ ($x=6$ and 9). J. Phys. Chem. Solids. 1998; 56:79-81.
40. Turteti RS, Morais E de, Wiesinger G, Reich C, Duang VH and Grössinger R. Structural detail and time dependence of initial susceptibility in Iron-rich Fe-Si ribbons. J. Magn. Magn. Mater. 1999; 205:290-300.
41. Randrianantoandro N, Gaffet E, Mira J, and Greneche JM. Magnetic hyperfine temperature dependence in Fe-Si crystalline alloys. Solid State. Commun. 1999; 11:323-327.
42. Sedov VL and Tsiegel'nik OA. Magnetic moment of iron atoms in invar Fe-Ni alloys. J. Magn. Magn. Mater. 1998; 183:117-126.
43. Allia P, Barico M, Tiberio P and Vinai F. Joule-heating effects in the amorphous $\text{Fe}_{40}\text{Ni}_{40}\text{B}_{20}$ alloy. Phys. Rev. B 1993; 47:3118-3125.
44. Clavaguera Mora MT, Barai MD, Surinach S, Clavaguera N, Parellada J, Crespo D and Pradell T. Direct evidence of two different relaxation processes induced by heat treatment on $\text{Fe}_{40}\text{Ni}_{40}\text{B}_{20}$ glassy ribbons. J. Phys. F. 1988; 18:2669-2681.

45. Brzózka K, Gawrorish M and Jezuita K. Influence of chemical disorder on the critical behavior of FeNi-based amorphous ferromagnets. *J. Magn. Magn. Mater.* 1996; 157-158:167-168.
46. Zadro K. Magnetic excitation in very dilute amorphous $\text{Fe}_x\text{Ni}_{80-x}\text{B}_{18}\text{Si}_2$ ferromagnets. *J. Magn. Magn. Mater.* 1998; 177-181:837-838.
47. Jortych E, Żurawicz JK, Oleszok D and Pćkata M. X-ray diffraction, magnetization and Mössbauer studies of nanocrystalline Fe-Ni alloys prepared by low- and high-energy ball milling. *J. Magn. Magn. Mater.* 2000; 208:221-230.
48. Rancourt DG, Lagarec K, Densemora A, Adunlop R, Glogstein JI, Reisenre RJ and Scorzelli RB. Experimental proof of the distinct electronic structure of a new meteoritic Fe-Ni alloy phase. *J. Magn. Magn. Mater.* 1999; 191:L255-L260.
49. Zhang XY, Xu YF, Yan ML, Chao LM, Zhang M, Hhao JH, Lai WY and Wang WK. Interdiffusion in $\text{Ni}_{80}\text{Fe}_{20}/\text{Mo}$ magnetic multilayers. *J. Magn. Magn. Mater.* 1998; 187:12-16.
50. Riveiro JM, Muñoz P, Andres JP and Lopez de la torre MA. About the possible observation and magnetic characterization of amorphous Ni. *J. Magn. Magn. Mater.* 1998; 188:153-160.
51. Detta A, Pal M, Das D and Chintalapudi SN. Disorder in nanocrystalline Ni_3Fe . *J. Magn. Magn. Mater.* 1999; 205:301-306.
52. Fratucello GB, Prandini AM, Luches P, Addato SD, Patchett AJ, and Nannarone S. Magnetic profile of Ni/Fe/Ni trilayers. *J. Magn. Magn. Mater.* 2000; 210:349-356.
53. Kaul SN and Babu PD. Detailed magnetization study of quenched random ferromagnets. I. Low-lying magnetic excitations. *Phys. Rev. B* 1996; 50:9308-9322.
54. Rancourt DG, Scorzelli RB and Schafer R. Low-spin γ_{LS} -Fe-Ni proposed as a new meteoritic mineral – reply. *J. Magn. Magn. Mater.* 1997; 174:324-330.

55. Rancourt DG, Scorzelli RB and Schafer R. Low-spin γ -Fe-Ni(γ_{LS}) proposed as a new mineral in Fe-Ni-bearing meteorites: Epitaxial intergrowth of γ_{LS} and tetrataenite as a possible equilibrium state at 20-40 at% Ni. *J. Magn. Magn. Mater.* 1995; 150:30-36.
56. Müllor M, Lederer T, Fornacon KH, and Schäfer R. Grain structure, coercivity and high – frequency noise in soft magnetic Fe-81Ni-6Mo Alloys. *J. Magn. Magn. Mater.* 1998; 177-181:231-232.
57. Hirohata A, Ono T, and Miyajima H. Magnetic properties of martensite in Fe-Ni alloy measured by means scanning probe microscopy. *J. Magn. Magn. Mater.* 1998; 177-181: 1243-1244.
58. de Oliveira AL, Tovar Costa MV, de Oliveira NA and Troper A. Study of magnetic hyperfine data on rare-earth impurities in Fe and Ni: Non-orbital contribution. *J. Magn. Magn. Mater.* 177-181; 1998:1441-1442.
60. Liu T, Hu TD, Xie YN, Zhao ZT and Ma RZ, *Nanostruc. Mater.* **8**(1997), 909
61. de Biasi RS and Grillo MLN. FMR Study of Crystallization in the Amorphous Alloy $Co_{65}Fe_4Ni_2Si_{15}B_{14}$ *J. Alloy. Comp.* 2000; 296:191-192.
62. de Biasi RS and Grillo MLN. FMR Study of Crystallization in the Amorphous Alloy $Co_{69}Fe_4Ni_1Mo_2B_{12}Si_{12}$ *J. Alloy. Comp.* 1998; 268:270-271.
63. Barandiaran JM and Schmool DS. Ferromagnetic resonance studies of multiphases ferromagnets. *J. Magn. Magn. Mater.* 2000; 221:178-186.
64. Unwin ME, Haycock PW, Hoon SR and Grannell PK. A novel broadband ferromagnetic resonance spectrometer. *J. Magn. Magn. Mater.* 1999; 205:199-208.
65. Gaganidze E, Esquinazi P and Ziese M. Vibrating ferromagnets in a magnetic field. *J. Alloy. Comp.* 2000; 310:144-152.
66. Gazeau F, Bracri JC, Gendron F, Perzynski R, Raikher YL, Stepanov VI and Dubois E. Magnetic resonance of ferrite nanoparticles: Evidence of surface effects. *J. Magn. Magn. Mater.* 1998; 180:175-187.
67. Franklin DR Anderton JC and Pointon AJ. Experimental evidence for a relationship between lotgering index and ferromagnetic resonance linewidth. *J. Magn. Magn. Mater.* 1996; 159:L51-L54.

68. Schmool DS and Barandiaran JM. New phenomena in the study of shape effects in ferromagnetic resonance. *J. Magn. Magn. Mater.* 1999; 191: 211-224.
69. Mizukami S, Ando Y and Miyazaki T. The study on ferromagnetic resonance linewidth for NM/80NiFe/NM (NM = Cu, Ta, Pd and Pt). *Jpn. J. Appl. Phys.* 2001; 40:580-585.
70. Rubinstein M, Haarris VG and Lubitz P. Ferromagnetic resonance in nanocrystalline $\text{Fe}_{73.5}\text{CuNb}_3\text{Si}_{13.5}\text{B}_9$ (Finemet). *J. Magn. Magn. Mater.* 2001; 201:306-312.
71. Thomas AH, Chantrell RW, El-Hilo M, Haycock PW and Grady KO. Calculation of FMR in interacting fine particle systems. *J. Magn. Magn. Mater.* 1995; 151:54-58.
72. Du J, Wu J, Tong LN, Lu M, Du JH, Pan MH, Zhai HR. and Xia H. Study on microstructural characterization and ferromagnetic resonance in sputtered Co/V multilayers. *Phys. Stat. Sol. (a)*.1998; 167:183-193.
73. Miglierini M. and Greneche JM. Mössbauer spectrometry of Fe(Cu)MB-type nanocrystalline alloys: I. The fitting model for the Mössbauer spectra. *J.Phys.:Condens.Matter.* 1997; 9: 2303-2319.
74. Miglierini M. and Greneche JM. Mössbauer spectrometry of Fe(Cu)MB-type nanocrystalline alloys: II. The topography of hyperfine interactions in Fe(Cu)ZrB alloys. *J.Phys.:Condens.Matter.* 1997; 9:2321-2347.
75. Baldokhin YV, Tcherdyntsev VV, Kaloshkin SD, Kochetov GA and Pustov YA. Transformations and fine magnetic structure of mechanically alloyed Fe–Ni alloys. *J. Magn. Magn. Mater.*1999; 203:313-315.



Appendix A

Mössbauer Effect

Recoil-free gamma-ray resonance absorption, The Mössbauer effect, also called nuclear gamma resonance fluorescence, has become the basis for a type of spectroscopy which has found wide application in many areas of science.

A.1 Theory of effect

The fundamental physics of this effect involves the transition (decay) of a nuclear from an excited state energy E_e to a ground state energy E_g with the emission of a gamma ray energy E_γ . If the emitting nucleus is free to recoil, so as to conserve momentum, the emitted gamma ray energy is

$$E_\gamma = (E_e - E_g) - E_r \quad (1)$$

Where E_r is the recoil energy of the nucleus. The magnitude of E_γ is given classically by the relationship

$$E_r = \frac{E_\gamma^2}{2mc^2} \quad (2)$$

Where m is the mass of the recoiling atom

c is the speed of light

Since E_r is a positive number, the E_γ will always be less than the difference $E_e - E_g$ and if the gamma ray is now absorbed by another nucleus, its energy is insufficient to promote the transition from the nucleus ground state E_g to the excited state E_e .

In 1957 R.L. Mössbauer discovered that if the emitting nucleus is held by strong bonding force in the lattice of the solid, the whole lattice take up the recoil energy, and the mass in the recoil energy equation (2) becomes the mass of the whole lattice. Since

this mass typically corresponds to that of 10^{10} of 10^{20} atoms, the recoil energy is reduced by the factor 10^{10} of 10^{20} , which the important result that $E_r \sim 0$ so that $E_\gamma = E_e - E_g$; that is, the emitting gamma-ray energy is exactly equal to the difference between the nuclear ground state and the excited state energy. Consequently, absorption of this gamma ray by the nucleus, which is also firmly bound to a solid lattice, can result in the “pumping” of the absorber nucleus ground state to the excited state. The newly excited nucleus remains on the average, in its upper energy state for a time given by its mean lifetime τ (a quantity dependent on energy, spin and parity of the nuclear state involved in the deexcitation process) and then falls back to the ground state by emission of the gamma-ray. An important feature of this emission process is the fact that it is essentially isotropic; that is, it occurs with equal probability in all directions.

A.2 Energy Modulation

It is necessary to provide an appropriate energy modulation of the gamma ray emitting in the initial decay process. An estimate of the energy nuclear to accomplish this can be calculated from the inherent width or sharpness of the excited-state nuclear level. This is given by the Heisenberg uncertainty principle as

$$\Gamma = \frac{h}{2\pi\tau} \quad (3)$$

h = Planck's constant

τ = The mean lifetime of the excited state

In case of ^{57}Fe a nucleus for which resonance fluorescence is especially easy to observe experimentally $\Gamma = 4.6 \times 10^{-12}$ keV. For this case the emitted gamma-ray energy correspond to 14.4 keV. That can take advantage of the Doppler phenomenon which states that if a radiation source has a velocity relative to an observer of v , its energy will be shifted by an amount equal to equation (4).

$$E = \left(\frac{v}{c}\right)E_\gamma \quad (4)$$

Setting the required Doppler energy equal to the nuclear transition energy leads to equation (3)

$$\begin{aligned} v &= c \frac{\Gamma}{E_\gamma} \quad (5) \\ &= 3 \times 10^{10} \text{ cm/s} \times \frac{4.6 \times 10^{-12} \text{ keV}}{14.4 \text{ keV}} \\ &= 0.0096 \text{ cm/s} \\ &= 0.0038 \text{ in/s} \end{aligned}$$

Relative velocities of this order of magnitude can be used to modulate the gamma ray emitted a typical Mössbauer transition, that is, to “sweep through” the energy width of the nuclear transition

A.3 Hyperfine Interaction

The hyperfine interaction is defined as the interaction between nucleus and the atomic electrons. In the field of Mössbauer spectroscopy, the hyperfine interaction is usually spilled up into several components for case of discussion. Effect produces by applying an external magnetic field are classified under the title of nuclear Zeeman effect.

A.3.1 Isomer Shift (δ)

The isomer (or chemical) shift can be obtained using Mössbauer spectroscopy. The relevant nuclear part depends on the nuclear radii of the ground excited states involved in the transition. The environmental part is the electron density that atomic electrons, usually S electrons have at the nucleus. Since it is not uncommon for valence electron to be in s orbitals, one can see why this quantity has also been known as the chemical shift. The isomer shift can be understood by considering how the nuclear energy levels shifted by the electrostatic interaction between these electrons

and positively charge nucleus of finite radius compared with a positively charge point nucleus. The isomer shift is seen in experiments in which recoil-free gamma radiation from a source is absorbed recoillessly by resonant nuclei in an absorber. The type and condition of the solid containing the source nuclei need not be identical to that containing the absorber nuclei. The value of the isomer shift is given by

$$\delta = \frac{2\pi}{3} e^2 Z \{ [\phi_s(0)]^2 - [\phi_a(0)]^2 \} \times \{ \langle R_e^2 \rangle - \langle R_g^2 \rangle \} \quad (6)$$

When Z_e is the nuclear charge, $[\phi(0)]^2$ is the electron density ($s = \text{source}$, $a = \text{absorber}$), and $\langle R_e^2 \rangle$ is the mean square radius of the nuclear positive charge distribution.

The total isomer shift (S_T), the effects of the Second – order Doppler Shift (SOD) must be included $= \delta_T = \delta + \text{SOD}$. The SOD is due to the fact that the source and absorber nuclei are in motion. Where a moving source emits resonant radiation, this is a frequency shift relative to stationary observer as result of the relativistic time dilation. The size of the SOD depends on the nature and temperature of the solids containing the source and absorber nuclei.

A.3.2 Quadrupole Interaction

A nucleus having a spin and a nonzero quadrupole moment will experience an orientation torque if located to a position where there is an electric field gradient. This interaction will removes some energy degeneracy in the excited and ground state nuclear level. The spilling depends on the absolute of the projection of the spin the quantization axis. If the nuclear spin is less than or equal to $1/2$, the nucleus possesses cubic symmetry, The electric field gradient at the nucleus is zero.

$$H_Q = \frac{e^2 q Q}{4I(2I-1)} [3I_z^2 - I^2 + \frac{1}{2}\eta(I_+^2 + I_-^2)] \quad (7)$$

Where $eq = V_{ZZ}$ (q is often called the electric field gradient), η (the asymmetry parameter) $= (V_{XX} - V_{YY})/V_{ZZ}$ and $I_{\pm} = I_x \pm I_y$ (Notice that, by

convention ; $0 \leq \eta \leq 1$; sine Laplace's equation applies, only 2 component q and η are needed to specify the EFG)

Calculations of the EFG parameters, a separation is usually made between the contributions:

1. Due to the aromatic electrons not in spherically symmetric distributions.
2. Due to the remaining lattice The problem of calculation the EFG components at the nucleus further complicated by the existence of shielding effect (produced by the subsequent distribution of atomic electrons in closed (Sternheimer factors)

A.3.3 Magnetic Interaction

The nucleus through its magnetic moment is also interactions with the electronic spin and orbital distributions. Hyperfine interaction can be written as

$$H_m = I \cdot A \cdot J \quad (8)$$

Where now the eigenstates of the system must includes both nuclear and atomic states,

A = The hyperfine interaction tensor

J = The total angular momentum of the atom or ion containing the Mössbauer Nucleus

I = The nuclear spin

Or can be written as

$$H_m = I \cdot A' \cdot S \quad (9)$$

Under conditions in which the electronic spin (S) or total angular momentum (J) is fluctuating rapidly compares to the motion of the nuclear spin (I), the nucleus only senses the average value of the electronic angular momentum. The interaction can be writer in from as a nucleus in an externally applied magnetic field,

$$\mathbf{H}_m = -\boldsymbol{\mu} \cdot \mathbf{B}_e \quad (10)$$

The field at nucleus is usually not simply equal to the value of the external field. The effective magnetic field B_e is written as

$$B_e = B_{ext} + B_{fc} + B_{sd} + B_{orb} \quad (11)$$

Where

B_e = the externally applied magnetic field neglecting demagnetizing and Lorentz fields

B_{fc} = the Fermi contact term*

B_{sd} = the electronic spin – dipole contribution from the surrounding ions (in cubic symmetry this term is zero)

B_{orb} = the magnetic field due to any resultant orbital angular momentum in the ion

* the Fermi contact Field (B_{fc}) arises from a resultant spin density (either up or down) at the nucleus. This effect is thus to S electron. Even in the case of spin – paired s electrons, their spatial distribution in the atom is effected by electron in incomplete shells. The net effect of the “core – polarization”, since the S electrons are at the nucleus, is that the magnetic field experienced can be orders of magnitudes large and in the opposite magnetic field in certain cases.

Table A1 ⁵⁷Fe nuclear transitions

Excited nuclear level ($\frac{3}{2}m_e$)	Ground nuclear level ($\frac{1}{2}m_e$)	Clebsch – Gordon coef. Squared	Vector spherical harmonic absolute value squared
3/2	1/2	1	$\frac{3}{4}(1 + \cos^2 \theta)$
3/2	-1/2	0	-
1/2	1/2	2/3	$\frac{3}{2}(\sin^2 \theta)$
1/2	-1/2	1/3	$\frac{3}{4}(1 + \cos^2 \theta)$
-1/2	1/2	1/3	$\frac{3}{4}(1 + \cos^2 \theta)$
-1/2	-1/2	2/3	$\frac{3}{2}(\sin^2 \theta)$
-3/2	1/2	0	-
-3/2	-1/2	1	$\frac{3}{4}(1 + \cos^2 \theta)$

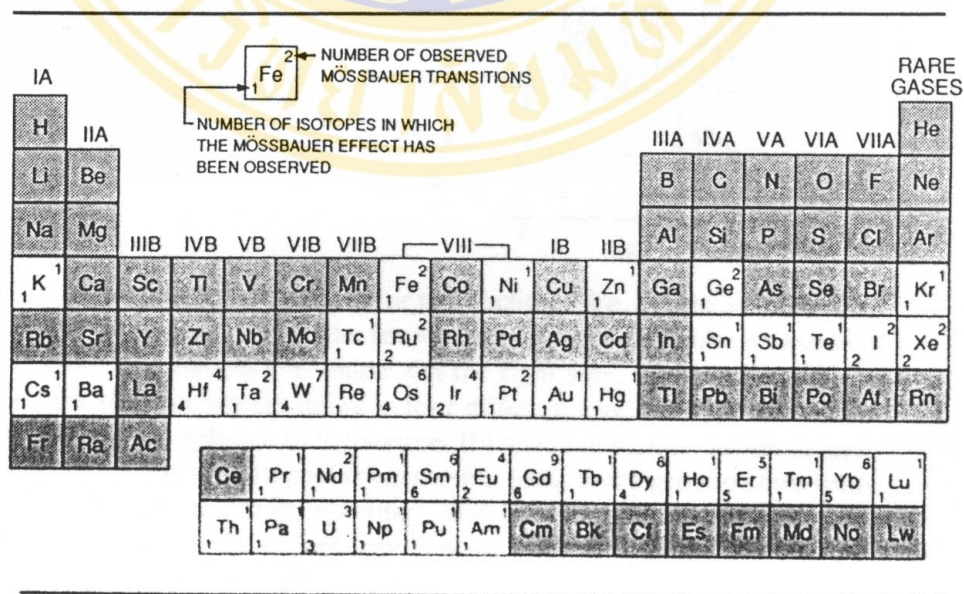


Figure A1Mössbauer Periodic Table.

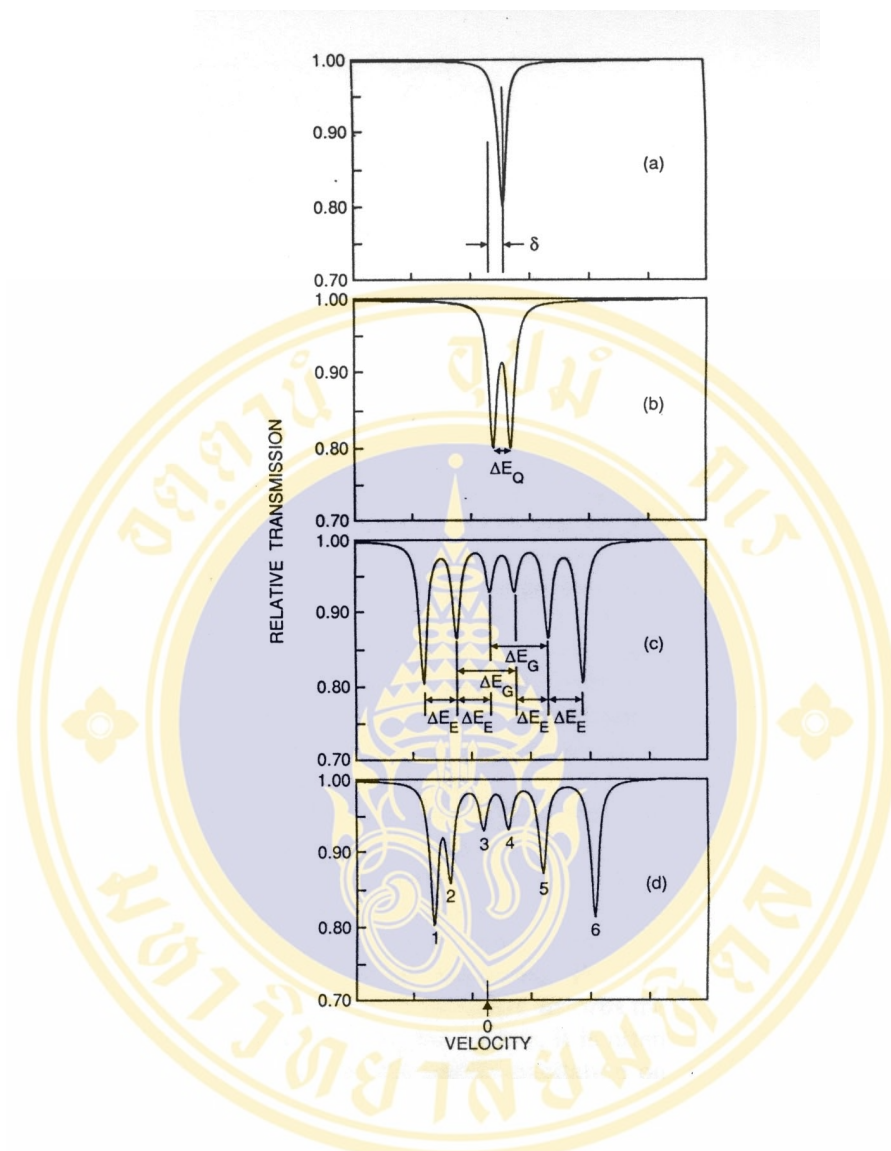
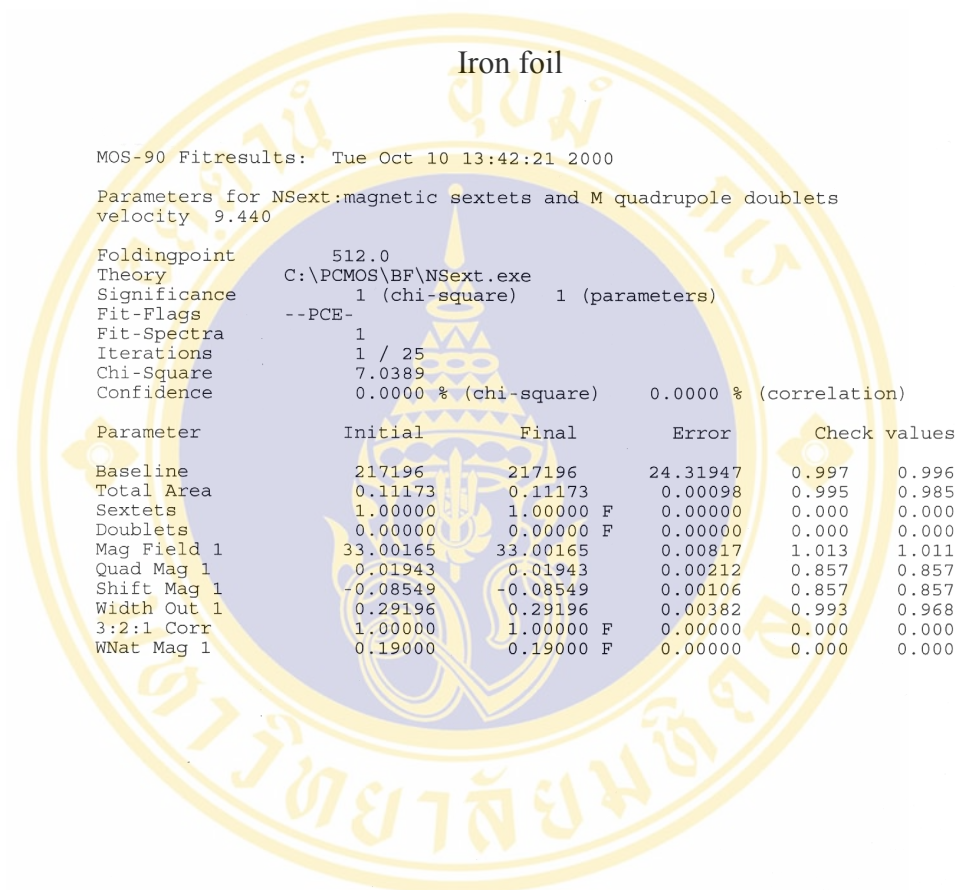


Figure A4. Hypothetical Mössbauer transmission spectra are shown corresponding to the case depicted in Fig (3) (a) the isomer shift (δ), (b) the quadrupole interaction (or quadrupole splitting, ΔE_Q), (c) the magnetic interaction (ΔE_G) and (d) the quadrupole and magnetic, hyperfine interaction (For a simple magnetic hyperfine structure, the ground state splitting, ΔE_G and excited state splitting, ΔE_E)



Appendix B

Fitting parameters of Fe₄₀Ni₄₀(Si+B)₁₉Mo₁₋₂ amorphous alloy fitted by PC Mos II



Before annealing by NSing Theory

MOS-90 Fitresults: Tue Jan 18 08:24:49 2000

\Parameters for NSing
velocity 7.689

Foldingpoint 512.0
 Theory C:\PCMO5\BF\NSing.exe
 Significance 1 (chi-square) 1 (parameters)
 Fit-Flags --PCE-
 Fit-Spectra 1
 Iterations 1 / 25
 Chi-Square 1.9181
 Confidence 0.0000 % (chi-square) 0.0000 % (correlation)

Parameter	Initial	Final	Error	Check values	
Baseline	2402809	2402809	107.28925	1.093	1.086
Total Area	0.05176	0.05176	0.00049	1.140	1.125
Isomer Shift 1	-0.49469	-0.49469	0.01020	0.932	0.924
Width 1	0.42396	0.42396	0.03456	1.843	1.656
Isomer Shift 2	2.11204	2.11204	0.01217	0.960	0.950
Width 2	3.01723	3.01723	0.27213	1.698	1.502
Area Sing 2	0.30834	0.30834	0.01113	1.405	1.374
Isomer Shift 3	-1.92839	-1.92839	0.00974	1.013	1.016
Width 3	2.54011	2.54011	0.25178	1.781	1.593
Area Sing 3	0.25046	0.25046	0.00879	1.238	1.199
Isomer Shift 4	3.56039	3.56039	0.01455	0.724	0.742
Width 4	2.00028	2.00028	0.20124	1.746	1.407
Area Sing 4	0.13465	0.13465	0.00722	1.366	1.326
Isomer Shift 5	-3.44407	-3.44407	0.01621	0.788	0.774
Width 5	2.46216	2.46216	0.22481	1.670	1.366
Area Sing 5	0.16203	0.16203	0.00707	1.297	1.269
Isomer Shift 6	0.61993	0.61993	0.01397	0.918	0.926
Width 6	1.37068	1.37068	0.18277	1.812	1.402
Area Sing 6	0.07663	0.07663	0.00560	1.511	1.325

Before annealing by MagDist Theory

```

\Parameters for MagDist: A distribution of magnetic sextets
fitresults of data :
velocity 7.689
foldingpoint 512.0
theory C:\PCMOS\BF\MagDist.exe
date Mon Mar 11 18:32:01 2002
flags --PCE-
fitspectra 1
chi2 1.4189
chi2-test 0.0000 %
corr-test 0.0000 %
fitcycles 1
maxiter 25
parasig 1
chi2sig 1
fitparameter 27
Baseline 2401823 2401823 95.56209 1.029 1.018
Total Area 0.04557 0.04557 0.00040 1.065 1.032
Distribution 16.00000 16.00000 F 0.00000 0.000 0.000
Sextets 0.00000 0.00000 F 0.00000 0.000 0.000
Doublets 0.00000 0.00000 F 0.00000 0.000 0.000
Min Mag Field 2.68805 2.68805 0.09013 0.950 0.996
Max Mag Field 25.32787 25.32787 0.09526 0.805 0.761
Quad Distr 0.05497 0.05498 0.02384 1.405 1.070
Shift Distr 0.03826 0.03825 0.01280 1.119 1.358
Width Out 0.31766 0.31766 0.01664 1.331 1.056
3:2:1 Corr 0.28507 0.28507 0.08621 1.952 1.313
Wnat Distr 0.19000 0.19000 F 0.00000 0.000 0.000
A 1st sextet 0.00095 0.00095 0.01581 0.963 1.980
A 2nd sextet 0.05993 0.05993 0.01070 1.720 1.013
A 3rd sextet 0.10761 0.10761 0.00883 1.231 1.452
A 4th sextet 0.00698 0.00698 0.01085 1.165 1.581
A 5th sextet 0.00070 0.00070 0.00676 0.936 1.166
A 6th sextet 0.03745 0.03745 0.00575 1.013 0.967
A 7th sextet 0.09073 0.09073 0.00598 0.950 1.043
A 8th sextet 0.11175 0.11175 0.00632 1.088 1.074
A 9th sextet 0.12880 0.12880 0.00576 1.033 1.040
A 10th sextet 0.06940 0.06940 0.00702 1.305 1.073
A 11th sextet 0.04561 0.04561 0.00637 1.113 1.024
A 12th sextet 0.05040 0.05040 0.00688 1.324 1.035
A 13th sextet 0.07276 0.07276 0.00687 1.293 1.068
A 14th sextet 0.07974 0.07974 0.00713 1.393 1.007
A 15th sextet 0.07198 0.07198 0.00637 1.343 1.080
    
```

Annealing at 350 °C by NSing Theory

MOS-90 Fitresults: Thu Jan 20 13:04:55 2000

\Parameters for NSing
velocity 7.688

Foldingpoint 512.0
 Theory C:\PCMO5\BF\NSing.exe
 Significance 1 (chi-square) 1 (parameters)
 Fit-Flags --PCE-
 Fit-Spectra 1
 Iterations 1 / 25
 Chi-Square 1.2166
 Confidence 0.0689 % (chi-square) 0.0000 % (correlation)

Parameter	Initial	Final	Error	Check values	
Baseline	968616	968616	68.33102	1.093	1.081
Total Area	0.04826	0.04826	0.00077	1.140	1.118
Isomer Shift 1	0.62239	0.62239	0.01759	0.973	0.967
Width 1	0.51838	0.51838	0.05889	1.922	1.756
Isomer Shift 2	-2.01750	-2.01750	0.01888	1.010	1.026
Width 2	2.25029	2.25029	0.29538	1.849	1.482
Area Sing 2	0.27147	0.27147	0.01562	1.336	1.264
Isomer Shift 3	-0.50055	-0.50055	0.01452	0.997	1.016
Width 3	0.68624	0.68624	0.13135	1.527	1.114
Area Sing 3	0.06911	0.06911	0.00574	1.096	0.967
Isomer Shift 4	3.65512	3.65512	0.02147	0.797	0.816
Width 4	1.79124	1.79123	0.23201	1.720	1.283
Area Sing 4	0.16057	0.16057	0.01077	1.289	1.260
Isomer Shift 5	-3.46960	-3.46960	0.02460	0.843	0.829
Width 5	1.88017	1.88016	0.26310	1.879	1.343
Area Sing 5	0.15219	0.15219	0.01239	1.438	1.368
Isomer Shift 6	2.18469	2.18469	0.01691	0.954	0.948
Width 6	2.05842	2.05842	0.30059	2.026	1.565
Area Sing 6	0.25747	0.25747	0.01398	1.349	1.223

Annealing at 350 °C by MagDist Theory

```

Parameters for MagDist: A distribution of magnetic sextets
fitresults of data :
velocity 7.688
foldingpoint 512.0
theory C:\PCMOS\BF\MagDist.exe
date Mon Mar 11 20:09:39 2002
flags --PCE-
fitspectra 1
chi2 1.0161
chi2-test 39.2817 %
corr-test 0.0000 %
fitcycles 1
maxiter 25
parasig 1
chi2sig 1
fitparameter 27
Baseline 968282 968282 63.02817 1.123 1.079
Total Area 0.04313 0.04313 0.00067 1.262 1.140
Distribution 16.00000 16.00000 F 0.00000 0.000 0.000
Sextets 0.00000 0.00000 F 0.00000 0.000 0.000
Doublets 0.00000 0.00000 F 0.00000 0.000 0.000
Min Mag Field 1.84642 1.84644 0.15790 1.352 1.432
Max Mag Field 25.96440 25.96435 0.19006 1.508 1.514
Quad Distr 0.12191 0.12192 0.14133 2.970 0.023
Shift Distr 0.00998 0.00997 0.07074 0.014 2.920
Width Out 0.36737 0.36737 0.03630 2.299 1.392
3:2:1 Corr 0.06901 0.06901 0.06297 1.389 1.131
Wnat Distr 0.19000 0.19000 0.00000 0.000 0.000
A 1st sextet 0.00785 0.00785 0.01175 1.351 1.484
A 2nd sextet 0.00042 0.00042 0.01323 1.906 1.228
A 3rd sextet 0.12842 0.12842 0.01279 1.367 1.469
A 4th sextet 0.04950 0.04950 0.01520 1.305 1.285
A 5th sextet 0.00014 0.00014 0.00000 0.000 0.000
A 6th sextet 0.00072 0.00072 0.00951 0.769 0.892
A 7th sextet 0.09981 0.09981 0.00997 1.314 1.047
A 8th sextet 0.01040 0.01040 0.00998 1.032 0.968
A 9th sextet 0.13544 0.13544 0.01040 1.176 0.891
A 10th sextet 0.08296 0.08296 0.01092 1.069 1.378
A 11th sextet 0.04001 0.04001 0.00999 0.938 1.081
A 12th sextet 0.08372 0.08372 0.01014 1.223 1.171
A 13th sextet 0.10085 0.10085 0.00960 1.096 0.964
A 14th sextet 0.09484 0.09484 0.00956 1.014 1.070
A 15th sextet 0.09497 0.09497 0.01006 1.216 0.935
    
```

Annealing at 400 °C by NSing Theory

MOS-90 Fitresults: Thu Jan 20 13:30:38 2000

\Parameters for NSing
velocity 7.688

Foldingpoint 512.0
 Theory C:\PCMOS\BF\NSing.exe
 Significance 1 (chi-square) 1 (parameters)
 Fit-Flags --PCE-
 Fit-Spectra 1
 Iterations 1 / 25
 Chi-Square 1.1654
 Confidence 0.6477 % (chi-square) 0.0000 % (correlation)

Parameter	Initial	Final	Error	Check values	
Baseline	916378	916378	69.52435	1.125	1.109
Total Area	0.05191	0.05191	0.00085	1.180	1.152
Isomer Shift 1	0.64679	0.64679	0.01941	0.952	0.948
Width 1	0.60322	0.60322	0.06877	1.983	1.727
Isomer Shift 2	-2.03499	-2.03499	0.02228	0.925	0.958
Width 2	1.98348	1.98348	0.26973	1.732	1.448
Area Sing 2	0.26598	0.26598	0.01665	1.339	1.230
Isomer Shift 3	-0.48563	-0.48563	0.01451	0.921	0.909
Width 3	0.67338	0.67338	0.12440	1.829	1.333
Area Sing 3	0.07796	0.07796	0.00626	1.344	1.171
Isomer Shift 4	3.63297	3.63297	0.02228	0.826	0.855
Width 4	1.71883	1.71883	0.21594	1.716	1.352
Area Sing 4	0.16491	0.16491	0.01271	1.106	1.113
Isomer Shift 5	-3.52504	-3.52504	0.02534	0.692	0.690
Width 5	1.87754	1.87754	0.25290	1.979	1.425
Area Sing 5	0.16201	0.16201	0.01364	1.359	1.331
Isomer Shift 6	2.19148	2.19148	0.02318	0.996	0.968
Width 6	1.90555	1.90555	0.31347	1.851	1.487
Area Sing 6	0.23098	0.23098	0.01685	1.198	1.077

Annealing at 400 °C by MagDist Theory

190 Fitresults: Sat Mar 08 19:01:05 2003

Parameters for MagDist: A distribution of magnetic sextets
velocity 7.688

Foldingpoint 512.0
Theory C:\NEWMOSS\MagDist.exe
Significance 1 (chi-square) 1 (parameters)
Fit-Flags --PCE-
Fit-Spectra 1
Iterations 1 / 25
Chi-Square 0.9198
Confidence 89.7747 % (chi-square) 0.0000 % (correlation)

Parameter	Initial	Final	Error	Check values
Baseline	915967	915967	60.28988	1.024 1.007
Total Area	0.04528	0.04528	0.00067	1.056 1.008
Distribution	16.00000	16.00000 F	0.00000	0.000 0.000
Sextets	0.00000	0.00000 F	0.00000	0.000 0.000
Doublets	0.00000	0.00000 F	0.00000	0.000 0.000
Min Mag Field	1.63987	1.63997	0.13963	0.618 0.598
Max Mag Field	26.53334	26.53332	0.14012	1.139 1.107
Quad Distr	0.03789	0.03789	0.00000	0.000 0.000
Shift Distr	0.05246	0.05246	0.00000	0.000 0.000
Width Out	0.33901	0.33901	0.02823	1.467 0.947
3:2:1 Corr	0.23517	0.23517	0.12696	1.940 1.895
Wnat Distr	0.19000	0.19000	0.00000	0.000 0.000
A 1st sextet	0.01137	0.01137	0.01282	1.449 1.290
A 2nd sextet	0.10649	0.10649	0.01302	0.885 1.241
A 3rd sextet	0.07094	0.07094	0.01305	0.965 0.706
A 4th sextet	-0.02536	-0.02536	0.01479	1.454 1.616
A 5th sextet	0.01159	0.01159	0.01203	1.161 1.141
A 6th sextet	0.05368	0.05368	0.00956	0.876 0.999
A 7th sextet	0.06872	0.06872	0.01094	1.186 1.437
A 8th sextet	0.10822	0.10822	0.01141	1.037 1.124
A 9th sextet	0.07266	0.07265	0.00906	0.985 1.101
A 10th sextet	0.06366	0.06366	0.01067	1.216 1.103
A 11th sextet	0.06150	0.06150	0.01019	1.224 1.134
A 12th sextet	0.08266	0.08266	0.01139	1.369 1.219
A 13th sextet	0.10825	0.10825	0.01250	1.565 1.339
A 14th sextet	0.08773	0.08773	0.01129	1.341 1.183
A 15th sextet	0.08573	0.08573	0.01108	1.398 1.163

Annealing at 450 °C by MagDist Theory

MOS-90 Fitresults: Mon Mar 10 17:32:37 2003

*Parameters for N_{Sext}: N magnetic sextets and M quadrupole doublets
velocity 7.688

```

Foldingpoint          512.0
Theory                C:\NEWMOSS\MagDist.exe
Significance          1 (chi-square)  1 (parameters)
Fit-Flags             --PCE-
Fit-Spectra          1
Iterations            1 / 25
Chi-Square            1.2579
Confidence            0.0105 % (chi-square)  0.0000 % (correlation)

```

Parameter	Initial	Final	Error	Check values
Baseline	1003665	1003665	73.25445	1.095 1.080
Total Area	0.05116	0.05116	0.00078	1.124 1.099
Distribution	7.00000	7.00000 F	0.00000	0.000 0.000
Sextets	4.00000	4.00000 F	0.00000	0.000 0.000
Doublets	0.00000	0.00000 F	0.00000	0.000 0.000
Min Mag Field	3.42646	3.42642	0.12976	1.804 1.657
Max Mag Field	28.61880	28.61879	0.21898	0.921 0.963
Quad Distr	0.92330	0.92336	0.16762	2.557 2.603
Shift Distr	-0.17063	-0.17067	0.08131	2.563 2.739
Width Out	0.56893	0.56893	0.03921	1.215 0.932
3:2:1 Corr	0.10601	0.10600	0.04856	1.411 1.374
Wnat Distr	0.19000	0.19000 F	0.00000	0.000 0.000
A 1st Sextet	0.12714	0.12714	0.00856	1.090 0.967
A 2nd Sextet	0.10150	0.10150	0.00857	1.732 1.644
A 3rd Sextet	0.08755	0.08755	0.00909	1.080 1.057
A 4th Sextet	0.08332	0.08332	0.00894	0.992 1.026
A 5th Sextet	0.13660	0.13660	0.01090	1.521 1.331
A 6th Sextet	0.03036	0.03036	0.00808	1.000 0.967
Mag Field 1	20.66624	20.66624	0.05885	1.053 1.033
Quad Mag 1	-0.10495	-0.10495	0.01487	1.103 1.091
Shift Mag 1	-0.03818	-0.03818	0.00815	0.846 0.831
Width Out 1	0.24552	0.24552	0.03126	0.952 0.654
3:2:1 Corr	1.00000	1.00000 F	0.00000	0.000 0.000
Area Mag 1	0.13383	0.13383	0.01503	0.929 0.830
WNat Mag 1	0.19000	0.19000 F	0.00000	0.000 0.000
Mag Field 2	23.91637	23.91638	0.18364	1.113 1.277
Quad Mag 2	-0.52418	-0.52418	0.04593	1.059 1.054
Shift Mag 2	-0.23118	-0.23118	0.02229	1.047 1.230
Width Out 2	0.28133	0.28133	0.09154	0.632 0.314
3:2:1 Corr	1.00000	1.00000 F	0.00000	0.000 0.000
Area Mag 2	0.04803	0.04803	0.01322	0.834 0.590
WNat Mag 2	0.19000	0.19000 F	0.00000	0.000 0.000
Mag Field 3	32.23190	32.23189	0.10611	0.846 0.901
Quad Mag 3	0.50170	0.50170	0.02484	0.533 0.515
Shift Mag 3	-0.25940	-0.25940	0.01215	0.539 0.526
Width Out 3	0.35101	0.35100	0.05612	1.975 1.537
3:2:1 Corr	1.00000	1.00000 F	0.00000	0.000 0.000
Area Mag 3	0.11268	0.11268	0.01582	1.567 1.423
WNat Mag 3	0.19000	0.19000 F	0.00000	0.000 0.000
Mag Field 4	33.58816	33.58816	0.05524	0.723 0.787
Quad Mag 4	0.01124	0.01124	0.01438	0.997 1.028
Shift Mag 4	-0.08616	-0.08616	0.00709	1.027 1.019
Width Out 4	0.26785	0.26785	0.02727	1.613 1.355
3:2:1 Corr	1.00000	1.00000 F	0.00000	0.000 0.000
Area Mag 4	0.14201	0.14201	0.01283	1.324 1.240
WNat Mag 4	0.19000	0.19000 F	0.00000	0.000 0.000

Annealing at 475 °C by MagDist Theory

MOSS-90 Fitresults: Mon Mar 10 17:29:13 2003

Parameters for NSext: N magnetic sextets and M quadrupole doublets
velocity 7.688

Foldingpoint 512.0
 Theory C:\NEWMOSS\MagDist.exe
 Significance 1 (chi-square) 1 (parameters)
 Fit-Flags --PCE-
 Fit-Spectra 1
 Iterations 1 / 25
 Chi-Square 1.3478
 Confidence 0.0001 % (chi-square) 0.0000 % (correlation)

Parameter	Initial	Final	Error	Check values	
Baseline	922024	922024	69.19406	1.068	1.056
Total Area	0.05168	0.05168	0.00079	1.093	1.074
Distribution	7.00000	7.00000 F	0.00000	0.000	0.000
Sextets	4.00000	4.00000 F	0.00000	0.000	0.000
Doublets	0.00000	0.00000 F	0.00000	0.000	0.000
Min Mag Field	3.36212	3.36213	0.09839	1.198	1.111
Max Mag Field	26.54776	26.54791	0.16786	1.191	1.186
Quad Distr	0.11847	0.11847	0.04051	0.892	0.643
Shift Distr	0.22910	0.22908	0.02050	0.696	0.964
Width Out	0.44268	0.44269	0.02941	1.016	0.857
3:2:1 Corr	0.34663	0.34663	0.09385	0.926	0.991
Wnat Distr	0.19000	0.19000 F	0.00000	0.000	0.000
A 1st Sextet	0.11710	0.11710	0.01177	0.749	0.942
A 2nd Sextet	0.10764	0.10764	0.01018	1.040	0.732
A 3rd Sextet	0.02932	0.02932	0.01127	0.809	1.052
A 4th Sextet	0.03424	0.03425	0.00785	0.998	1.010
A 5th Sextet	0.12239	0.12240	0.01544	1.322	1.224
A 6th Sextet	0.08104	0.08103	0.00971	0.945	0.862
Mag Field 1	19.49570	19.49601	0.07582	0.976	0.850
Quad Mag 1	0.09122	0.09123	0.02140	0.793	0.765
Shift Mag 1	0.03231	0.03229	0.01117	0.833	0.844
Width Out 1	0.24510	0.24500	0.04654	1.512	1.092
3:2:1 Corr	1.00000	1.00000 F	0.00000	0.000	0.000
Area Mag 1	0.09844	0.09842	0.01829	1.422	1.126
Wnat Mag 1	0.19000	0.19000 F	0.00000	0.000	0.000
Mag Field 2	23.48722	23.48738	0.12997	0.860	0.938
Quad Mag 2	-0.38337	-0.38336	0.03385	0.791	0.754
Shift Mag 2	-0.21999	-0.21998	0.01621	0.867	0.900
Width Out 2	0.24655	0.24661	0.04023	1.764	1.112
3:2:1 Corr	1.00000	1.00000 F	0.00000	0.000	0.000
Area Mag 2	0.05890	0.05896	0.03329	1.702	1.553
Wnat Mag 2	0.19000	0.19000 F	0.00000	0.000	0.000
Mag Field 3	32.51019	32.51014	0.07711	0.939	0.955
Quad Mag 3	0.46540	0.46540	0.01722	0.725	0.672
Shift Mag 3	-0.26755	-0.26756	0.00852	0.719	0.719
Width Out 3	0.36558	0.36553	0.03930	1.839	1.533
3:2:1 Corr	1.00000	1.00000 F	0.00000	0.000	0.000
Area Mag 3	0.16725	0.16723	0.01550	1.520	1.409
Wnat Mag 3	0.19000	0.19000 F	0.00000	0.000	0.000
Mag Field 4	33.68176	33.68179	0.04277	0.953	1.000
Quad Mag 4	0.08388	0.08389	0.01135	0.796	0.810
Shift Mag 4	-0.12267	-0.12267	0.00569	0.769	0.782
Width Out 4	0.25523	0.25522	0.02098	1.296	1.122
3:2:1 Corr	1.00000	1.00000 F	0.00000	0.000	0.000
Area Mag 4	0.17265	0.17266	0.01313	1.221	1.193
Wnat Mag 4	0.19000	0.19000 F	0.00000	0.000	0.000

Annealing at 500 °C by MagDist Theory

MOS-90 Fitresults: Tue Mar 11 14:32:18 2003

Parameters for N₆ext: N magnetic sextets and M quadrupole doublets
velocity 9.440

Foldingpoint 512.0
 Theory C:\NEWMOSS\MagDist.exe
 Significance 1 (chi-square) 1 (parameters)
 Fit-Flags --PCE-
 Fit-Spectra 1
 Iterations 1 / 25
 Chi-Square 1.9176
 Confidence 0.0000 % (chi-square) 0.0000 % (correlation)

Parameter	Initial	Final	Error	Check values	
Baseline	2086008	2086008	89.93127	1.034	1.031
Total Area	0.06895	0.06895	0.00052	1.062	1.055
Distribution	7.00000	7.00000	F 0.00000	0.000	0.000
Sextets	4.00000	4.00000	F 0.00000	0.000	0.000
Doublets	1.00000	1.00000	F 0.00000	0.000	0.000
Min Mag Field	4.22299	4.22296	0.10899	1.204	1.095
Max Mag Field	26.51055	26.51048	0.12890	1.235	1.236
Quad Distr	0.58023	0.58022	0.02035	0.712	0.612
Shift Distr	-0.04227	-0.04228	0.01144	0.493	0.552
Width Out	0.44127	0.44126	0.02777	1.359	1.183
3:2:1 Corr	0.42966	0.42966	0.03792	0.975	0.987
Wnat Distr	0.19000	0.19000	F 0.00000	0.000	0.000
A 1st Sextet	0.09953	0.09953	0.00823	1.142	1.227
A 2nd Sextet	0.03368	0.03368	0.00487	0.883	0.960
A 3rd Sextet	0.07161	0.07161	0.00615	1.255	1.209
A 4th Sextet	0.03825	0.03825	0.00569	1.164	1.284
A 5th Sextet	0.12180	0.12179	0.00883	1.283	1.162
A 6th Sextet	0.04040	0.04040	0.00554	1.130	1.274
Mag Field 1	19.56285	19.56284	0.05318	1.044	0.990
Quad Mag 1	0.08083	0.08083	0.01674	0.619	0.561
Shift Mag 1	0.01888	0.01888	0.00905	0.559	0.563
Width Out 1	0.16022	0.16023	0.03381	1.588	1.296
3:2:1 Corr	1.00000	1.00000	F 0.00000	0.000	0.000
Area Mag 1	0.04114	0.04114	0.00908	1.707	1.381
WNat Mag 1	0.19000	0.19000	F 0.00000	0.000	0.000
Mag Field 2	23.04223	23.04247	0.26329	1.957	1.845
Quad Mag 2	-0.18979	-0.18974	0.05915	1.617	1.547
Shift Mag 2	-0.26094	-0.26092	0.02767	1.562	1.531
Width Out 2	0.59363	0.59360	0.12467	1.957	1.290
3:2:1 Corr	1.00000	1.00000	F 0.00000	0.000	0.000
Area Mag 2	0.07401	0.07401	0.01372	1.723	1.237
WNat Mag 2	0.19000	0.19000	F 0.00000	0.000	0.000
Mag Field 3	31.66827	31.66826	0.07019	0.788	0.803
Quad Mag 3	0.46873	0.46873	0.01660	0.712	0.712
Shift Mag 3	-0.23746	-0.23746	0.00816	0.726	0.713
Width Out 3	0.41990	0.41990	0.03912	1.926	1.691
3:2:1 Corr	1.00000	1.00000	F 0.00000	0.000	0.000
Area Mag 3	0.12678	0.12678	0.01056	1.704	1.590
WNat Mag 3	0.19000	0.19000	F 0.00000	0.000	0.000
Mag Field 4	33.63502	33.63502	0.02148	0.816	0.817
Quad Mag 4	0.04475	0.04475	0.00558	0.881	0.892
Shift Mag 4	-0.08894	-0.08894	0.00282	0.860	0.855
Width Out 4	0.35342	0.35342	0.01118	1.300	1.235
3:2:1 Corr	1.00000	1.00000	F 0.00000	0.000	0.000
Area Mag 4	0.30959	0.30959	0.00899	1.280	1.277
WNat Mag 4	0.19000	0.19000	F 0.00000	0.000	0.000
Quad Splt	0.75260	0.75259	0.03132	1.583	1.456
Isom shift	0.18173	0.18173	0.01411	1.305	1.291
Width	0.32317	0.32316	0.05034	0.931	0.588
Pt area	0.04545	0.04545	0.00824	1.244	0.948

Annealing at 525 °C by N sext Theory

MOS-90 Fitresults: Mon Mar 10 17:20:43 2003

Parameters for N sext: N magnetic sextets and M quadrupole doublets
velocity 9.440

Foldingpoint 512.0
Theory C:\NEWMOSS\Nsext.exe
Significance 1 (chi-square) 1 (parameters)
Fit-Flags --PCE-
Fit-Spectra 1
Iterations 1 / 25
Chi-Square 1.4197
Confidence 0.0000 % (chi-square) 0.0000 % (correlation)

Parameter	Initial	Final	Error	Check values
Baseline	2398446	2398446	96.06197	1.024 1.018
Total Area	0.05533	0.05533	0.00049	1.048 1.031
Sextets	9.00000	9.00000	F 0.00000	0.000 0.000
Doublets	1.00000	1.00000	F 0.00000	0.000 0.000
Mag Field 1	19.94797	19.94798	0.08040	0.834 0.977
Quad Mag 1	0.36047	0.36047	0.01872	0.935 0.943
Shift Mag 1	-0.16135	-0.16135	0.01010	0.754 0.663
Width Out 1	0.21606	0.21606	0.03514	1.116 0.707
3:2:1 Corr	1.00000	1.00000	F 0.00000	0.000 0.000
WNat Mag 1	0.19000	0.19000	F 0.00000	0.000 0.000
Mag Field 2	20.64499	20.64499	0.09518	0.869 0.882
Quad Mag 2	0.07805	0.07805	0.01751	0.776 0.784
Shift Mag 2	-0.01252	-0.01252	0.00933	0.915 0.893
Width Out 2	0.49453	0.49454	0.05316	1.136 0.976
3:2:1 Corr	1.00000	1.00000	F 0.00000	0.000 0.000
Area Mag 2	0.19565	0.19566	0.01871	1.062 0.983
WNat Mag 2	0.19000	-0.19000	F 0.00000	0.000 0.000
Mag Field 3	22.52610	22.52610	0.09729	0.939 1.000
Quad Mag 3	1.10775	1.10775	0.02642	0.843 0.742
Shift Mag 3	0.77245	0.77245	0.01428	0.715 0.772
Width Out 3	0.21400	0.21400	0.04349	1.294 0.786
3:2:1 Corr	1.00000	1.00000	F 0.00000	0.000 0.000
Area Mag 3	0.04147	0.04147	0.00597	1.113 1.006
WNat Mag 3	0.19000	0.19000	F 0.00000	0.000 0.000
Mag Field 4	22.81105	22.81106	0.08350	0.844 0.856
Quad Mag 4	-0.64059	-0.64059	0.02066	0.841 0.834
Shift Mag 4	0.22358	0.22357	0.01052	0.842 0.855
Width Out 4	0.22770	0.22770	0.03879	1.402 0.925
3:2:1 Corr	1.00000	1.00000	F 0.00000	0.000 0.000
Area Mag 4	0.05558	0.05558	0.00744	1.148 0.991
WNat Mag 4	0.19000	0.19000	F 0.00000	0.000 0.000
Mag Field 5	25.24532	25.24532	0.10721	0.983 1.002
Quad Mag 5	-0.00234	-0.00234	0.02481	0.688 0.693
Shift Mag 5	-0.19442	-0.19442	0.01278	0.675 0.721
Width Out 5	0.32229	0.32229	0.07095	1.662 1.128
3:2:1 Corr	1.00000	1.00000	F 0.00000	0.000 0.000
Area Mag 5	0.07940	0.07940	0.01973	1.567 1.074
WNat Mag 5	0.19000	0.19000	F 0.00000	0.000 0.000
Mag Field 6	26.40248	26.40250	0.11851	0.711 0.726
Quad Mag 6	0.61978	0.61977	0.03716	1.255 1.154
Shift Mag 6	-0.00510	-0.00510	0.01805	1.140 1.180
Width Out 6	0.22392	0.22392	0.06898	1.583 1.000
3:2:1 Corr	1.00000	1.00000	F 0.00000	0.000 0.000
Area Mag 6	0.03603	0.03603	0.01154	1.450 1.107
WNat Mag 6	0.19000	0.19000	F 0.00000	0.000 0.000
Mag Field 7	26.96745	26.96744	0.13146	1.024 0.965
Quad Mag 7	-0.14153	-0.14153	0.02505	1.044 1.042
Shift Mag 7	-0.06672	-0.06673	0.01203	1.123 0.963
Width Out 7	0.57923	0.57923	0.06509	1.631 1.244
3:2:1 Corr	1.00000	1.00000	F 0.00000	0.000 0.000
Area Mag 7	0.19471	0.19471	0.02092	1.190 1.074
WNat Mag 7	0.19000	0.19000	F 0.00000	0.000 0.000
Mag Field 8	32.53126	32.53126	0.08350	0.800 0.759
Quad Mag 8	-0.04414	-0.04414	0.01878	0.867 0.891
Shift Mag 8	0.01055	0.01055	0.01043	0.676 0.582
Width Out 8	0.26935	0.26935	0.04556	1.650 1.330
3:2:1 Corr	1.00000	1.00000	F 0.00000	0.000 0.000
Area Mag 8	0.07637	0.07637	0.01376	1.221 1.069
WNat Mag 8	0.19000	0.19000	F 0.00000	0.000 0.000
Mag Field 9	33.65167	33.65167	0.05405	0.580 0.619
Quad Mag 9	0.13660	0.13660	0.01363	0.707 0.694
Shift Mag 9	-0.12880	-0.12880	0.00711	0.677 0.702
Width Out 9	0.26905	0.26905	0.02470	1.188 1.069
3:2:1 Corr	1.00000	1.00000	F 0.00000	0.000 0.000
Area Mag 9	0.11612	0.11612	0.01214	0.858 0.823
WNat Mag 9	0.19000	0.19000	F 0.00000	0.000 0.000
Quad spl 1	0.94091	0.94091	0.04383	0.955 1.095
Isom shift 1	0.21934	0.21934	0.02558	1.036 1.043
width 1	0.90777	0.90777	0.08585	1.163 0.806
Pt area 1	0.13959	0.13959	0.00671	1.008 0.903

Annealing at 550 °C by NSext Theory

MOS-90 Fitresults: Mon Mar 10 17:18:37 2003

Parameters for NSext: N magnetic sextets and M quadrupole doublets
velocity 9.440

Parameter	Initial	Final	Error	Check values	
Foldingpoint	512.0				
Theory	C:\NEWMOSS\NSext.exe				
Significance	1 (chi-square)	1 (parameters)			
Fit-Flags	---CE-				
Fit-Spectra	1				
Iterations	2 / 25				
Chi-Square	1.4740				
Confidence	0.0000 % (chi-square)	0.0000 % (correlation)			
Parameter	Initial	Final	Error	Check values	
Baseline	3081026	3081026	103.88449	1.094	1.070
Total Area	0.03752	0.03752	0.00040	1.241	1.153
Sextets	8.00000	8.00000	F 0.00000	0.000	0.000
Doublets	1.00000	1.00000	F 0.00000	0.000	0.000
Mag Field 1	18.82515	18.82502	0.19292	1.124	0.911
Quad Mag 1	-0.16111	-0.16105	0.04124	0.938	1.290
Shift Mag 1	-0.21132	-0.21130	0.02379	1.390	1.949
Width Out 1	0.40856	0.40869	0.12838	2.578	1.524
3:2:1 Corr	1.00000	1.00000	F 0.00000	0.000	0.000
WNat Mag 1	0.19000	0.19000	F 0.00000	0.000	0.000
Mag Field 2	20.91613	20.91617	0.24450	0.925	1.022
Quad Mag 2	-0.02252	-0.02245	0.04386	1.150	0.831
Shift Mag 2	-0.12391	-0.12390	0.02267	0.997	0.775
Width Out 2	0.56292	0.56284	0.19324	4.851	3.347
3:2:1 Corr	1.00000	1.00000	F 0.00000	0.000	0.000
Area Mag 2	0.14665	0.14664	0.06678	4.949	3.615
WNat Mag 2	0.19000	0.19000	F 0.00000	0.000	0.000
Mag Field 3	21.27332	21.27314	0.09762	1.050	0.944
Quad Mag 3	0.43654	0.43654	0.02359	1.010	1.009
Shift Mag 3	0.50808	0.50806	0.01225	1.025	0.982
Width Out 3	0.24855	0.24846	0.05065	1.202	0.699
3:2:1 Corr	1.00000	1.00000	F 0.00000	0.000	0.000
Area Mag 3	0.07514	0.07513	0.01234	1.080	0.933
WNat Mag 3	-0.19000	0.19000	F 0.00000	0.000	0.000
Mag Field 4	23.86752	23.86727	0.07077	0.838	0.888
Quad Mag 4	-0.13053	-0.13055	0.02284	0.655	0.670
Shift Mag 4	0.06248	0.06251	0.01254	0.657	0.691
Width Out 4	0.16714	0.16702	0.04526	1.089	0.838
3:2:1 Corr	1.00000	1.00000	F 0.00000	0.000	0.000
Area Mag 4	0.05595	0.05587	0.01816	1.056	0.653
WNat Mag 4	0.19000	0.19000	F 0.00000	0.000	0.000
Mag Field 5	23.63336	23.63263	0.12255	0.577	0.571
Quad Mag 5	-0.23395	-0.23384	0.02563	0.778	0.847
Shift Mag 5	-0.15051	-0.15043	0.01708	0.607	0.656
Width Out 5	0.40027	0.40027	0.08807	2.310	1.638
3:2:1 Corr	1.00000	1.00000	F 0.00000	0.000	0.000
Area Mag 5	0.16910	0.16909	0.04723	2.648	2.038
WNat Mag 5	0.19000	0.19000	F 0.00000	0.000	0.000
Mag Field 6	23.73402	23.73414	0.11562	0.983	0.894
Quad Mag 6	0.93705	0.93707	0.02749	0.995	1.011
Shift Mag 6	0.20056	0.20057	0.01400	1.068	1.068
Width Out 6	0.36024	0.36025	0.06177	1.340	0.982
3:2:1 Corr	1.00000	1.00000	F 0.00000	0.000	0.000
Area Mag 6	0.11020	0.11018	0.01873	1.202	1.073
WNat Mag 6	0.19000	0.19000	F 0.00000	0.000	0.000
Mag Field 7	26.60571	26.60515	0.10322	0.633	0.647
Quad Mag 7	-0.24379	-0.24382	0.01970	0.958	0.904
Shift Mag 7	-0.15407	-0.15410	0.01298	1.224	1.266
Width Out 7	0.35866	0.35871	0.05212	1.952	1.549
3:2:1 Corr	1.00000	1.00000	F 0.00000	0.000	0.000
Area Mag 7	0.16667	0.16671	0.02563	1.775	1.577
WNat Mag 7	0.19000	0.19000	F 0.00000	0.000	0.000
Mag Field 8	26.75040	26.75011	0.06170	0.642	0.710
Quad Mag 8	-0.13333	-0.13330	0.01918	0.895	0.992
Shift Mag 8	0.07629	0.07630	0.01039	1.042	1.000
Width Out 8	0.15966	0.15975	0.03746	1.707	1.346
3:2:1 Corr	1.00000	1.00000	F 0.00000	0.000	0.000
Area Mag 8	0.06237	0.06243	0.01790	1.529	1.236
WNat Mag 8	0.19000	0.19000	F 0.00000	0.000	0.000
Quad spl1	0.85345	0.85345	0.03570	0.968	1.034
Isom shift 1	0.11235	0.11236	0.02086	0.965	0.995
width 1	0.62562	0.62558	0.06069	1.178	0.933
Pt area 1	0.12271	0.12271	0.00750	1.358	1.502

Annealing at 575 °C by N Sext Theory

MOS-90 Fitresults: Mon Mar 10 17:13:41 2003

Parameters for N Sext: N magnetic sextets and M quadrupole doublets
velocity 9.436

Parameter	Initial	Final	Error	Check values	
Foldingpoint	512.0				
Theory	C:\NEWMOSS\NSext.exe				
Significance	1 (chi-square)	1 (parameters)			
Fit-Flags	--PCE-				
Fit-Spectra	1				
Iterations	1 / 25				
Chi-Square	1.5228				
Confidence	0.0000 % (chi-square)		0.0000 % (correlation)		
Baseline	2217379	2217379	88.79894	1.066	1.054
Total Area	0.06609	0.06609	0.00048	1.156	1.114
Sextets	8.00000	8.00000	F 0.00000	0.000	0.000
Doublets	1.00000	1.00000	F 0.00000	0.000	0.000
Mag Field 1	18.25861	18.25861	0.05925	0.952	0.950
Quad Mag 1	0.00592	0.00592	0.01425	0.855	0.851
Shift Mag 1	-0.31746	-0.31746	0.00779	0.832	0.830
Width Out 1	0.22968	0.22968	0.03019	1.314	1.028
3:2:1 Corr	1.00000	1.00000	F 0.00000	0.000	0.000
WNat Mag 1	0.19000	0.19000	F 0.00000	0.000	0.000
Mag Field 2	19.47686	19.47687	0.09346	1.451	1.275
Quad Mag 2	0.31165	0.31165	0.02128	1.467	1.438
Shift Mag 2	0.10160	0.10160	0.00934	1.191	1.166
Width Out 2	0.37908	0.37908	0.04749	1.449	1.163
3:2:1 Corr	1.00000	1.00000	F 0.00000	0.000	0.000
Area Mag 2	0.11698	0.11698	0.01423	1.349	1.224
WNat Mag 2	0.19000	0.19000	F 0.00000	0.000	0.000
Mag Field 3	18.12453	18.12453	0.10886	1.049	1.005
Quad Mag 3	0.53547	0.53547	0.02388	0.760	0.748
Shift Mag 3	0.49243	0.49243	0.01169	0.782	0.742
Width Out 3	0.22010	0.22010	0.05361	2.315	1.486
3:2:1 Corr	1.00000	1.00000	F 0.00000	0.000	0.000
Area Mag 3	0.04307	0.04307	0.00837	1.642	1.513
WNat Mag 3	0.19000	0.19000	F 0.00000	0.000	0.000
Mag Field 4	20.89628	20.89629	0.20593	0.905	0.963
Quad Mag 4	-0.49749	-0.49749	0.05180	1.400	1.290
Shift Mag 4	-0.03080	-0.03080	0.01909	1.329	1.318
Width Out 4	0.54013	0.54013	0.11293	2.110	1.426
3:2:1 Corr	1.00000	1.00000	F 0.00000	0.000	0.000
Area Mag 4	0.09109	0.09109	0.01843	2.007	1.654
WNat Mag 4	0.19000	0.19000	F 0.00000	0.000	0.000
Mag Field 5	23.92936	23.92936	0.12288	1.357	1.297
Quad Mag 5	-0.01137	-0.01137	0.02133	1.433	1.537
Shift Mag 5	-0.05116	-0.05116	0.00808	1.101	1.225
Width Out 5	0.50437	0.50437	0.06854	2.033	1.903
3:2:1 Corr	1.00000	1.00000	F 0.00000	0.000	0.000
Area Mag 5	0.21892	0.21892	0.03724	2.035	1.847
WNat Mag 5	0.19000	0.19000	F 0.00000	0.000	0.000
Mag Field 6	24.23337	24.23337	0.07187	0.861	0.902
Quad Mag 6	0.76043	0.76042	0.01988	0.942	0.864
Shift Mag 6	0.07337	0.07337	0.00911	0.972	1.052
Width Out 6	0.22678	0.22678	0.03523	1.382	1.274
3:2:1 Corr	1.00000	1.00000	F 0.00000	0.000	0.000
Area Mag 6	0.06237	0.06237	0.01166	1.347	1.311
WNat Mag 6	0.19000	0.19000	F 0.00000	0.000	0.000
Mag Field 7	26.40673	26.40673	0.07910	1.239	1.243
Quad Mag 7	-0.10833	-0.10833	0.01186	0.951	0.975
Shift Mag 7	-0.08651	-0.08651	0.00637	1.052	1.079
Width Out 7	0.43074	0.43074	0.03177	1.714	1.693
3:2:1 Corr	1.00000	1.00000	F 0.00000	0.000	0.000
Area Mag 7	0.24411	0.24411	0.02755	1.814	1.886
WNat Mag 7	0.19000	0.19000	F 0.00000	0.000	0.000
Mag Field 8	27.20436	27.20436	0.06976	1.026	0.977
Quad Mag 8	0.03179	0.03179	0.02123	0.740	0.826
Shift Mag 8	0.19030	0.19030	0.01194	0.940	0.870
Width Out 8	0.16087	0.16087	0.03477	1.697	1.253
3:2:1 Corr	1.00000	1.00000	F 0.00000	0.000	0.000
Area Mag 8	0.03513	0.03513	0.00805	1.532	1.286
WNat Mag 8	0.19000	0.19000	F 0.00000	0.000	0.000
Quad spl 1	0.80183	0.80183	0.03753	0.873	1.023
Isom shift 1	0.09491	0.09491	0.02020	0.896	0.901
width 1	0.74490	0.74490	0.06936	1.545	1.205
Pt area 1	0.11369	0.11369	0.00516	1.282	1.189

Annealing at 600 °C by N Sext Theory

MOS-90 Fitresults: Sat Mar 08 18:53:22 2003

Parameters for N Sext: N magnetic sextets and M quadrupole doublets
velocity 9.436

Foldingpoint 512.0
 Theory C:\NEWMOSS\N Sext.exe
 Significance 1 (chi-square) 1 (parameters)
 Fit-Flags --PCE-
 Fit-Spectra 1
 Iterations 1 / 25
 Chi-Square 1.5576
 Confidence 0.0000 % (chi-square) 0.0000 % (correlation)

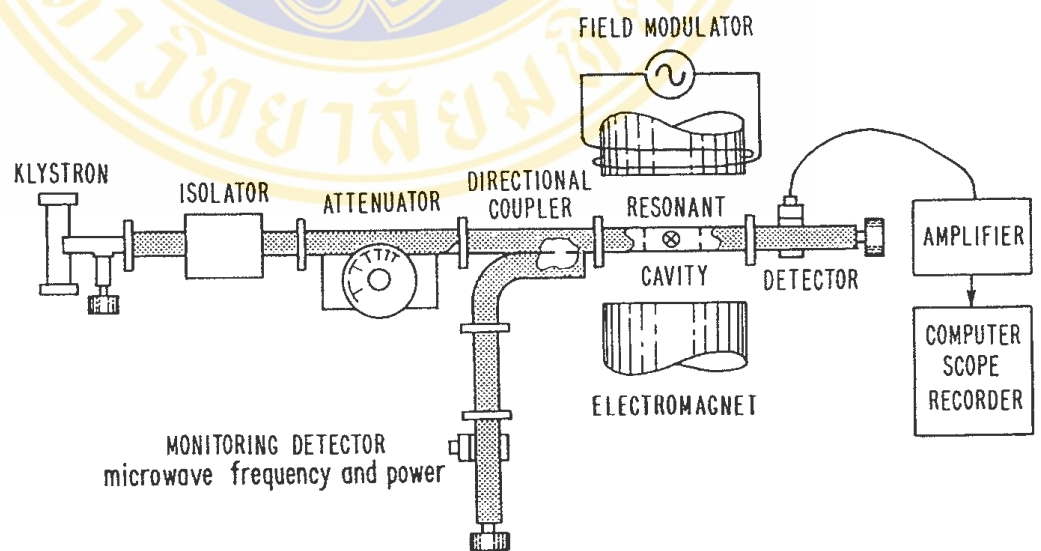
Parameter	Initial	Final	Error	Check values	
Baseline	2947952	2947952	96.89286	1.031	1.022
Total Area	0.02001	0.02001	0.00036	1.085	1.051
Sextets	4.00000	4.00000 F	0.00000	0.000	0.000
Doublets	1.00000	1.00000 F	0.00000	0.000	0.000
Mag Field 1	23.92793	23.92792	0.10813	1.816	1.649
Quad Mag 1	0.27914	0.27914	0.04163	1.190	1.182
Shift Mag 1	0.03897	0.03897	0.00949	1.169	1.061
Width Out 1	0.37260	0.37260	0.05423	1.535	1.460
3:2:1 Corr	1.00000	1.00000 F	0.00000	0.000	0.000
WNat Mag 1	0.19000	0.19000 F	0.00000	0.000	0.000
Mag Field 2	23.64563	23.64562	0.06686	1.474	1.376
Quad Mag 2	-0.08117	-0.08117	0.02612	1.074	1.265
Shift Mag 2	0.00130	0.00130	0.00647	1.406	1.143
Width Out 2	0.34677	0.34677	0.03960	1.560	1.382
3:2:1 Corr	1.00000	1.00000 F	0.00000	0.000	0.000
Area Mag 2	0.39426	0.39425	0.07317	1.421	1.488
WNat Mag 2	0.19000	0.19000 F	0.00000	0.000	0.000
Mag Field 3	26.61400	26.61398	0.16146	1.285	1.560
Quad Mag 3	0.07586	0.07585	0.03729	2.215	1.247
Shift Mag 3	0.03597	0.03598	0.02069	1.482	1.818
Width Out 3	0.32225	0.32224	0.08740	2.608	2.053
3:2:1 Corr	1.00000	1.00000 F	0.00000	0.000	0.000
Area Mag 3	0.14366	0.14366	0.04640	2.765	2.172
WNat Mag 3	0.19000	0.19000 F	0.00000	0.000	0.000
Mag Field 4	26.21128	26.21128	0.22805	0.963	1.005
Quad Mag 4	-0.29886	-0.29884	0.07308	1.446	2.106
Shift Mag 4	-0.19559	-0.19560	0.03570	1.900	1.185
Width Out 4	0.27710	0.27710	0.12885	3.081	1.815
3:2:1 Corr	1.00000	1.00000 F	0.00000	0.000	0.000
Area Mag 4	0.07130	0.07130	0.03010	2.227	1.833
WNat Mag 4	0.19000	0.19000 F	0.00000	0.000	0.000
Quad spl 1	0.46305	0.46305	0.03683	0.891	0.891
Isom shift 1	0.11388	0.11388	0.02275	0.792	0.857
width 1	0.38037	0.38036	0.06141	1.674	1.076
Pt area 1	0.09462	0.09462	0.00835	1.253	1.124



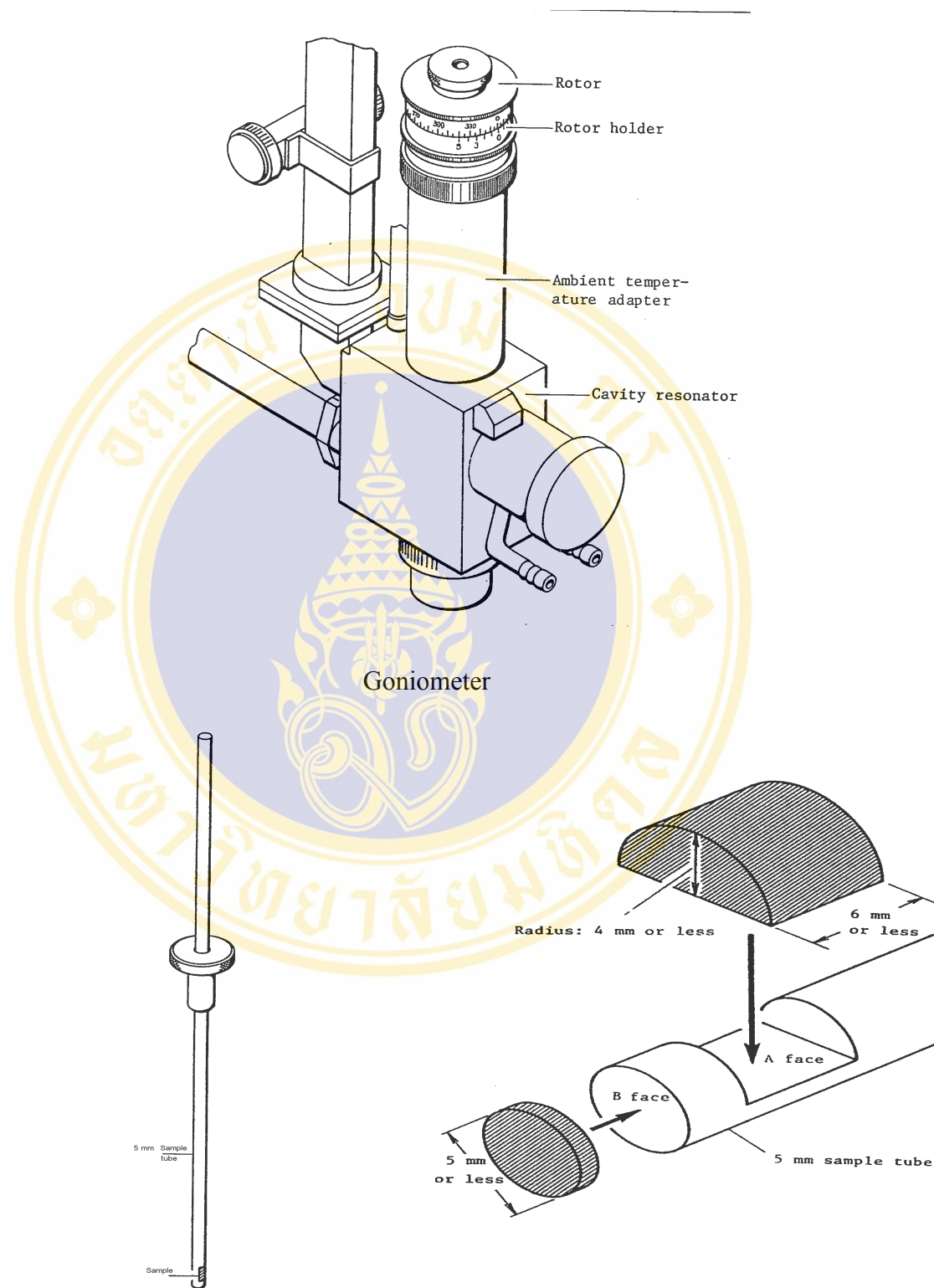
Appendix C



ESR Spectrometer



Block Diagram of ESR Spectrometer



Sample Holder

Loading sample

BIOGRAPHY

NAME	Mr. Somjet Saiseng
DATE OF BIRTH	9 July 1977
PLACE OF BIRTH	Ubonrachathani, Thailand
INSTITUTIONS ATTENDED	Mahidol University,1998 : Bachelor of Science (Chemistry) Mahidol University,2003 : Master of Science (Physical Chemistry)
RESEARCH GRANT	Postgraduate Education and Research Program in Chemistry, PERCH Teaching Assistant scholarship